POLITECNICO DI TORINO

MASTER's Degree in Mechatronics engineering

MASTER's Degree Thesis

Air Gap-Integrated Capacitive Power Transfer System for Electrically Excited Synchronous Machine

Supervisors

Prof. Radu BOJOI

Prof. Zeljko PANTIC

Candidate

Stefano SAVIO

October 2022

Abstract

The development of cost-effective electric vehicles has renewed interest in the Wound Field Synchronous Machines (WFSMs) for traction applications. However, efficiency and reliability issues of the brushes for rotor excitation present a bottleneck for adopting WFSMs. To overcome these challenges, the application of wireless power transfer systems for field excitation has recently been explored. This thesis presents an integrated Capacitive Power Transfer (CPT) system for field excitation of WFSMs. The proposed coupling structure for CPT is placed within the air gap of the machine. The coupling plates, constructed of magnetic material, constitute the coupling structure. The novelty of the proposed approach is that the presented design allows power transfer to the rotor without increasing the active volume of the machine. A preliminary feasibility analysis of the system is performed through Finite Element Analysis (FEA) simulations and different topologies of matching networks are compared. A prototype with a stator and a Computer Numerical Control (CNC) fabricated fictitious rotor is developed to test the proposed CPT system. Experimental verification of the proposed power transfer system shows an efficiency of 81.3% with a transferred power of 64 W at 2 MHz frequency.

Acknowledgements

This thesis work wouldn't be possible without the help and support of several people that helped and followed me from the first day I arrived at the FREEDM center at North Carolina State University. Thanks to my Supervisor in the United States Zejko Pantic, to have included me in this new project and giving me the possibility to join his Ph.D. students group, an extremely motivated and collaborative team that never left me alone, and to my Italian advisor Radu Bojoi. Thanks to my team members Syed Muhammad Hassan Gillani, Ujjwal Pratik and Ritvik Chattopadhyay for helping me with their advice and experience during the development of my thesis. A special thanks go to Karen Autry, Hulgize Kassa and Rebecca Mclennan, without whom my stay in the USA would not have been the same.

I would also like to take this opportunity to thanks my new roommates and friends in these five months Jacob Vickery, Spencer White, Payton Christian, Brad DeLuzio, Andrew and Matthew Hobson, Jon Anzola, Zhansen Akhmetov and last but not the least Claudio Briganti, who helped and supported me more than he knows. Thanks to the Polytechnic of Turin, which allowed me to have this American experience.

Thank all my family, my parents and my grandparents for sustaining me economically and morally. Thank Livia and Luciano for their kindness and closeness, Andrea, Edoardo and all the people that have been close to me during these 5 past years, despite the difficulties.

"sic itur ad astra"
Eneide (IX, 641), Virgilio

Table of Contents

List of Tables

List of Figures

Acronyms

WFSM
Wound field syncronous machine

LSM
loss separation method

EV
electric vehicle

IPMSM
Interior permanent magnet synchronous rotor

IM
Induction motor

IPT
Inductive power transfer

SCR
Silicon controlled rectifier

AVR
Automatic voltage regulator

CWPT
Capacitive wireless power transfer

PM
Permanent magnets

FEA

Finite Element Analysis

Chapter 1

Introduction

Nowadays, electric motors are getting a lot of interest from the industry as part of a consistent transition from engine motors to electric motors. The electric motor can be a good candidate for the future due to the sustainability that they bring with them, low maintenance compared to the classic ones, and optimal performances.

This study is linked to a specific category of electric motors, the Wound field synchronous machine, WFSM. Those motors are characterized by the absence of permanent magnets (PM) on the rotor or stator and hence WFSM is much cheaper than the PM machine. As explained in [1], WFSMs are chosen when the customer is interested in power generation applications from a few kVA to GVA with an high efficiency and reliability.

On the other side, as there are no permanent magnets on the rotor, a system to generate the rotor field is needed. In these terms, a lot of solutions have been suggested during the years, considering their dynamic performances, compactness, and reliability of them [2] but all of them included brushes, slip rings or additional components that are quite invasive or increase significantly the dimension of the machines, need periodic maintenance and have a significant weight.

To overcome these issues, new solutions have been proposed during the years including the use of harmonics, inductive and capacitive excitation systems [3], but none of them capable of exploiting a truly solution to the problems: the harmonic excitation and the inductive power transfer avoid the use of brushes, but they have a low efficiency. Capacitive power transfer solutions seems to be a valid alternative in terms of cost and efficiency,but the spread of electric field in the nearby environment limits its use for lower power application for human safety. Additional components are also added to realize the CPT system.

1.1 Thesis objectives

This dissertation aims to study and develop a unique CWPT structure for a WFSM. In particular, the main objectives are:

- to investigate the proposed geometry topology of the capacitive plates, understanding the parameters effect on the overall performance of the machine;
- to investigate through Finite Element Analysis (FEA) different configuration and consequently build a prototype looking at the best design.
- to test the prototype to verify if there is an effective power transfer between the plates.

1.2 The thesis outline

In order to accomplish the study objectives, the dissertation is structured as follows:

- from Chapter 2 to Chapter 3, a general description of the different excitation system is presented putting more attention on the CWPT system. Moreover, the need of a compensation circuit for this kind of topology is explained;
- Chapter 4 describes the conducted Finite Element Analysis through the software ANSYS, showing the procedure and practical consideration on the proposed structure of the capacitive coupler. Moreover, an analysis of the estimated losses is performed.
- in Chapter 5 the analytical modeling of the prototype is described and two compensation network are developed and compared;
- Chapter 6 shows the analysis results coming from a preliminary sweep of few parameters of the coupler regarding the overall performance of the machine. Both the previously described compensation networks are illustrated with different Pareto fronts.
- in Chapter 7 the construction of a prototype of a CWPT is proposed. Consequently, a full power transfer test has been performed in order to verify its feasibility. The challenges encountered during the prototype development have also been discussed in detail.
- A Bayesian optimization procedure is explained in Chapter 8, presenting the challenges related to it.

- Chapter 9 carries out a final analysis about the obtained results and the possible improvements that may be developed in the future

Chapter 2

Wound field synchronous machine: State-of-the-art for excitation systems

The growing interest in the electric vehicles (EVs) brought the customers to find alternative solutions to the wide use of permanent magnets in their motors. Interior permanent magnet synchronous motors (IPMSMs) and Induction motors (IMs) are costly and do not represent a valid alternative in the future because they are based on the extraction of rare material. WFSMs represent an attractive solution because they get rid of permanent magnets and can achieve higher efficiency, but still, they represent some critical issues.

During the years starting from 1920, many excitation solutions for the rotor field have been provided [1], starting from DC exciters, that uses DC generators as power source, coming to the most recent solutions that use wireless power transfer systems. The primary connection between all those methods and that differentiates them from the proposed design is that most of them derive power from the spinning shaft by adding brushes, slip rings or other structures, increasing the length of the motor consequently. Talking about the most common solutions to derive power to the rotor, those can be classified in three categories: static excitation systems, brushless, and embedded systems. Further solutions like inductive power transfer (IPT) and CPT received significant interest in recent years. This chapter aims to give an overview of the principal excitation systems highlighting their pros and cons of them.

2.1 Static excitation systems

Static excitation systems are the oldest solutions proposed and they make large use of brushes and slip rings. A slip ring is an electromechanical device that transmits power between two structures, one is static and the other one is rotating. The main purpose is that it allows the energy to flow between two electrical components while just one of them is rotating and the other one is fixed, like the stator of a motor.

The pros about them are that they allow bidirectional power flow and they are very cheap, but on the contrary, there are components that slide on each other. This generates friction between components and mechanical wear that brings the need of periodic maintenance. A simple setup is shown in figure 2.1: the brushes are maintained in contact with the slip rings through a charged spring.

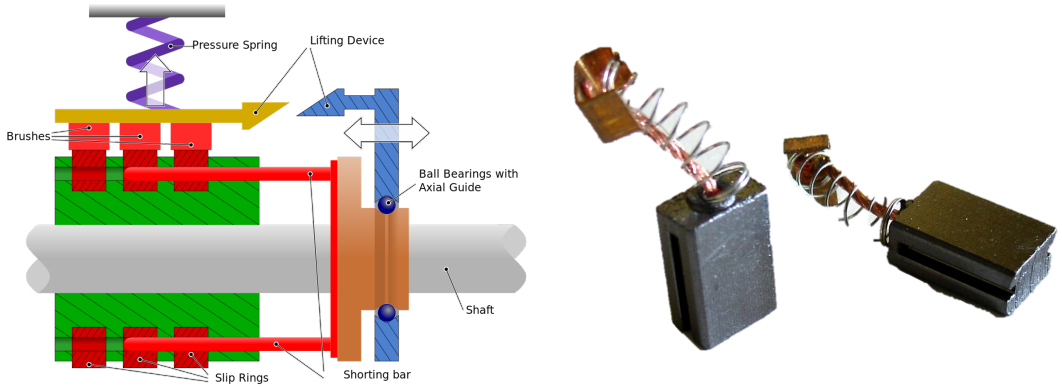

Figure 2.1: Left: Cross section of slip rings for an electric motor, from *Wikipedia*; right: carbon fiber brushes, from [4]

Figure 2.2 shows a basic excitation configuration of a brushed system. From the grid, a 3-phase winding is energized to generate the rotating stator field. An excitation transformer is needed to provide power to the field windings from the grid. Then, a silicon-controlled rectifier (SCR) combined with an automatic voltage regulator (AVR) rectifies the current. Through the brushes, the current is brought to the rotating parts of the machine and finally to the field windings.

More configurations have been developed, including the use of a boost-buck converter in alternative to solve problems related to a low grid voltage condition. In the end, a discharge circuit is needed to guarantee a fast way to de-excite the rotor field windings.

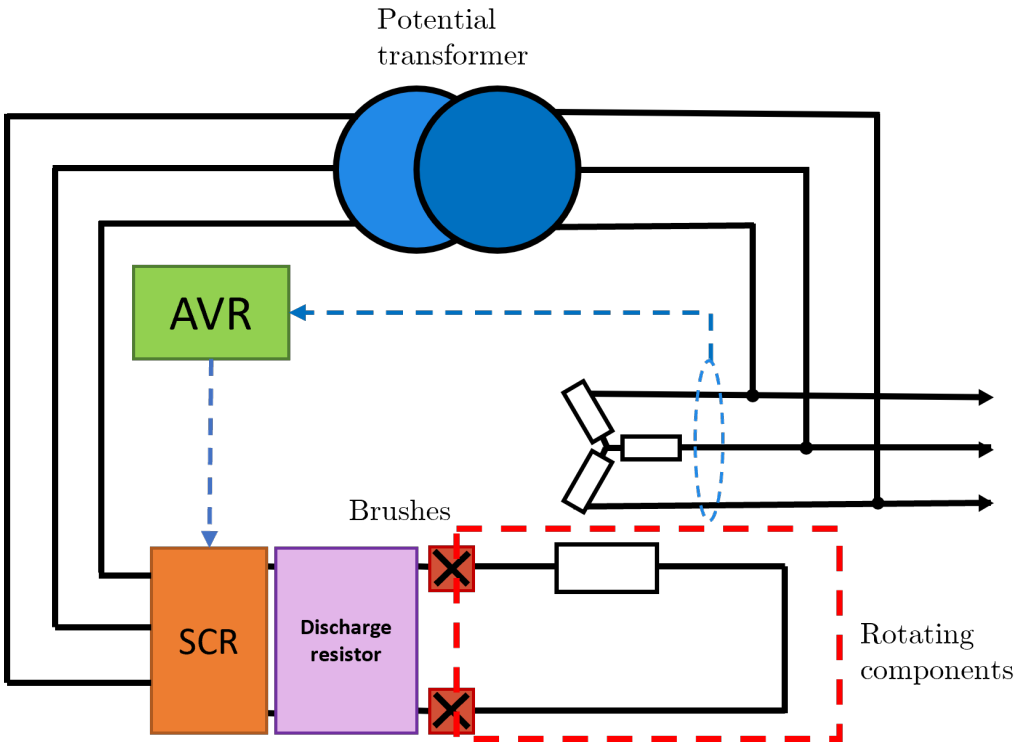

Figure 2.2: Static excitation configuration

2.2 Brushless excitation systems

This kind of solution is generally used in standby generator sets. It delivers power from the shaft and is contactless 2.3. It has proven reliability that lets bring this solution to be used in different scenarios, especially where periodic maintenance is not achievable, like the aerospace domain.

On the other side, the additional component required for this configuration occupies significant space on the shaft, so it's not always implementable.

The excitation system is based on a three-phase rotor winding that is excited by a DC current present on the stator of the excitation system, shown in 2.3. As explained before, those additional components are mounted on the shaft of the machine. When the shaft revolves, an electromotive force is induced in the gap between the stator exciter and the rotor. A rotating rectifier transforms the AC current into DC to feed the rotor field windings of the machine. This kind of solution is generally implemented when a good excitation control is needed, mostly implemented in small to medium generator sets [1].

Another contactless solution can be achieved with the use of a rotary transformer.

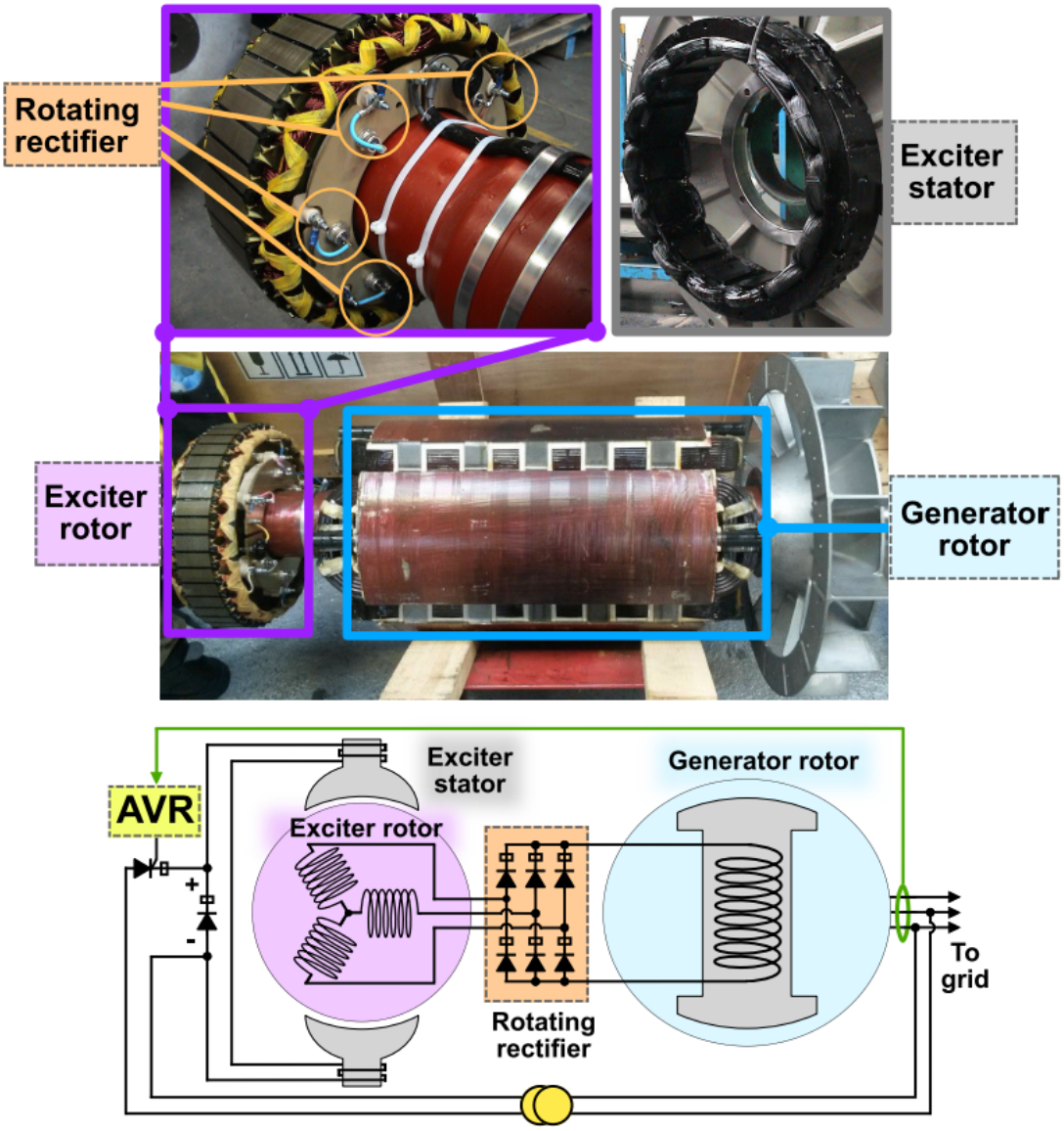

Figure 2.3: Components of a brushless excitation system, from [1]

A rotary transformer works like the static one but presents a geometry that lets it rotate on its shaft. There exists two principal structures for them, an axial version of it and a flat one [5], shown in figure 2.4.

This solution is more compact compared to the previous one, has a high power density and is independent of the shaft speed and its position.

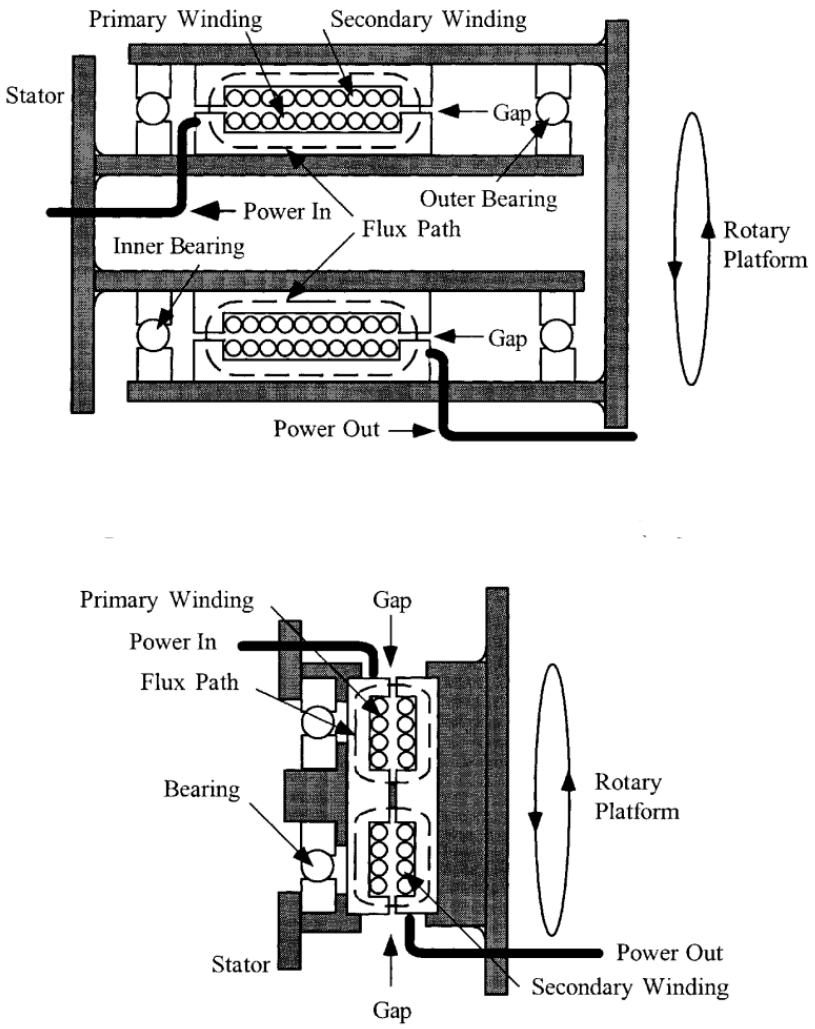

Figure 2.4: Top: axial rotary transformer; Bottom: flat plane rotary transformer, from [6]

On the other hand, they have a more complex structure. They are unidirectional power and are expensive. The introduction of a rotary transformer adds a few constraints that are not present in a common transformer [7]. A bigger air gap, directly depending on the eccentric dimension of the rotating shaft, results in low magnetizing inductance. Furthermore, the distance between the primary and secondary windings imposes a significant leakage inductance generating a not neglectable amount of losses.

2.3 Embedded, integrated or exciterless excitation systems

This kind of solution implements the exciter components directly on the stator of the machine, avoiding increasing the overall dimensions of the machine. The idea is not new, but recently they obtained a renewed interest in the industry. The basic principle is based on the use of harmonics. The excitation power is generated by an extra single-phase harmonic winding located on the stator designed in a way that generates an electromotive force. The good points about this solution are that it is again contactless, it does not depend on the shaft position, and it does not need any complex electronics. On the other side, a similar configuration imposes to modify the structure and the geometry of the machine itself and this can affect its performance and its control of it. As additional space is needed to store the stator harmonic windings, more space is necessarily increasing the active size of the WFSM. The simplest configuration that can be implemented is shown in figure 2.5.

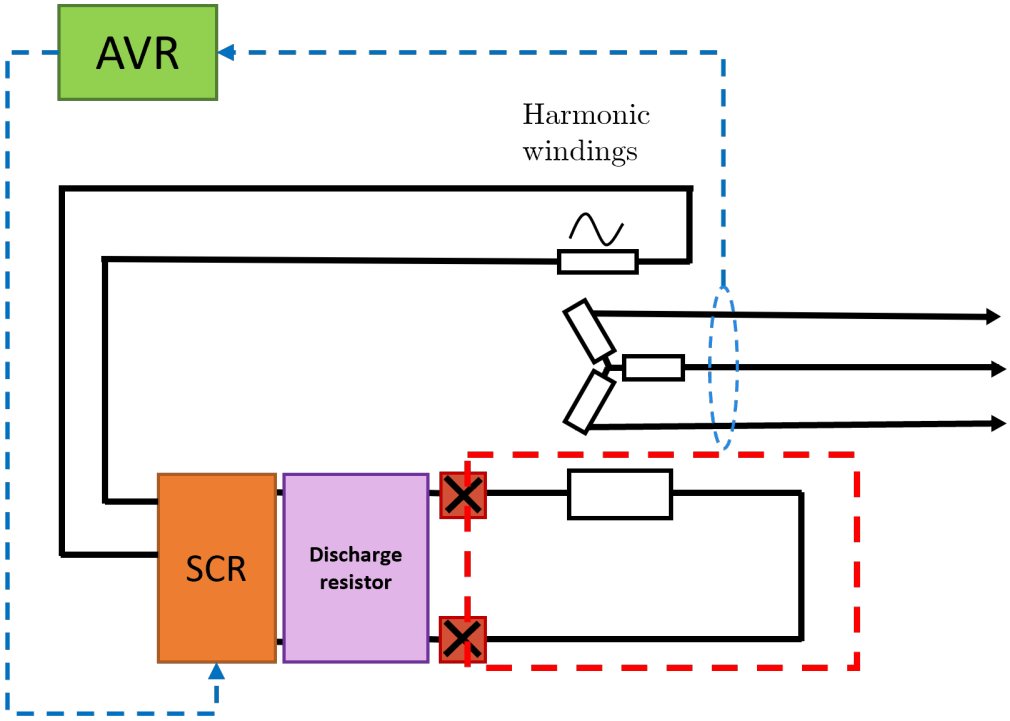

Figure 2.5: Basic scheme of a harmonic excitation system

2.4 Wireless power transfer solutions

A separate section is dedicated to the methods concerning wireless power transfer solutions. Inductive power transfer (IPT) and capacitive power transfer (CPT) are two methods that exploit the near-field electromagnetic induction, magnetic induction, and electric one, respectively. IPT was already known and studied originally by Nicola Tesla [8]. Nowadays, established solutions regarding roadway lighting [9], transport systems, and handling applications have been introduced. From [10], it's clear how IPT systems are a better choice in situations where the air gap is significant while having an important efficiency drop over short transfer distances, compared to CPT solutions [11], as shown in fig. 2.6.

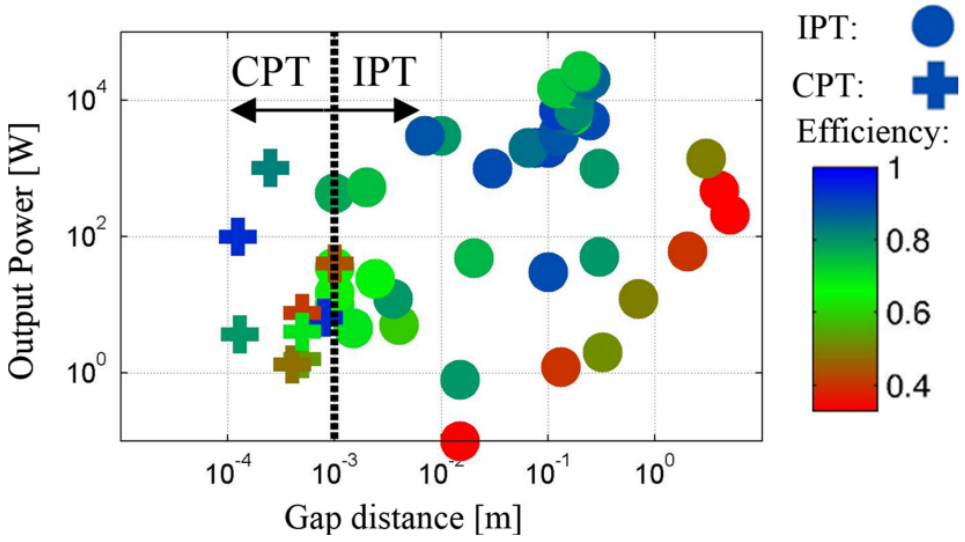

Figure 2.6: Output power versus gap distance, from [11]

An IPT system works with a magnetic field: the receiving coil is put in close proximity to the track wires in order to catch the magnetic flux around. The principle is very similar to a transformer but with a smaller magnetic coupling

The next chapter is dedicated to a more accurate explanation of the CPT system as a major part of the thesis project.

Chapter 3

Capacitive wireless power transfer and compensation topology

The concept of Capacitive Wireless Power Transfer was first demonstrated by Nicola Tesla back in 1892 [8]. In his experiment, he shows by applying a high-frequency voltage to two metal plates and putting in between two tube lights those turn on, demonstrating in this way the transmission of power without contact between parts.

3.1 Capacitive wireless power transfer principle

The basic idea of a CWPT is extremely simple, as shown in fig.3.1. It is divided into two portions, a forward path and a backward path. Through the forward path, the current goes from the source to the load and returns back using the backward path. The power transfer is guaranteed by two capacitive couplers that let the system transmit the power wirelessly. The distance between the capacitive plates depends on the application and can vary from a few mm (electronics applications) to cm (electric e-drives). The more the gap increases, the more complexity of the system increases In the case of a capacitor with simple geometry and with a small air gap between the plates, the value of the total capacitance can be computed based on the known formula:

$$C = \frac{e_0 A}{d} \tag{3.1}$$

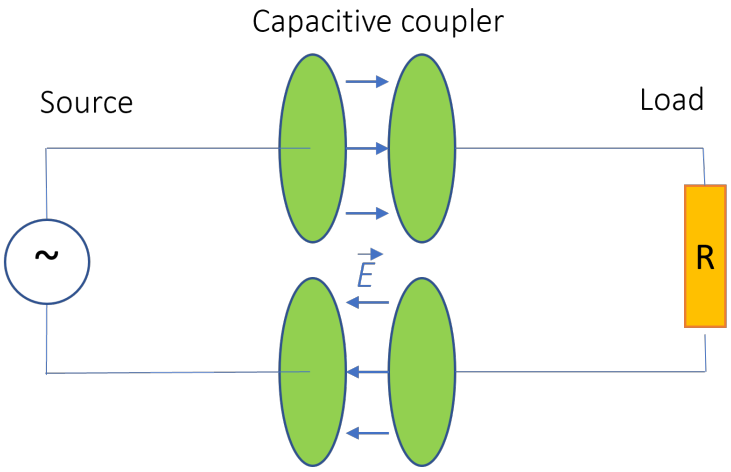

Figure 3.1: Basic scheme of CWPT

where e_0 is the dielectric constant of air, A is the surface area of the capacitive plates and d is the distance between them.

3.2 Fundamental topologies of CWPT

Different configuration topologies have been developed in the past years. The classical configuration is the one that is presented in the previous section with four capacitive plates where the direct and the return path are parallel to each other, as shown in figure 3.1. In order to avoid undesired cross-coupling in this configuration the two paths need to be spaced each other to minimize the cross-coupling effect.

Another topology that has been proposed is the one that uses only two metal plates as a direct path using the ground as a returning path [12], as shown in figure 3.2. This coupler has a large coupling tolerance but presents very low power transfer capability and very poor efficiency.

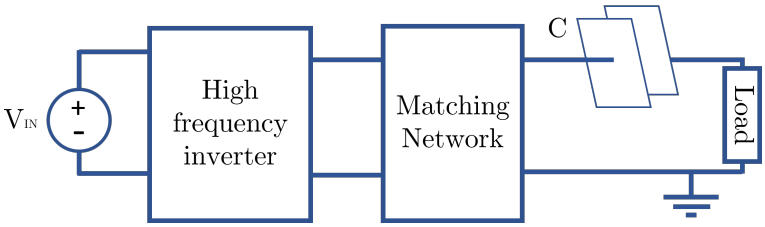

Figure 3.2: Single wire CPT system

A topology that has been very important in this research field is the four plates stacked configuration [13] shown in figure 3.3.

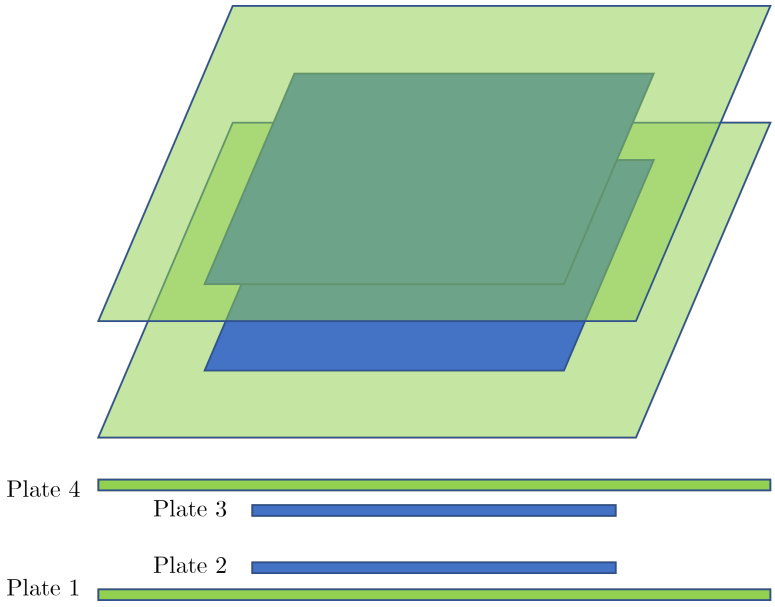

Figure 3.3: Structure of the four plate capacitance model

This kind of configuration was first studied and later implemented for large air gap power transfer like EV charging. The main characteristic of this topology is that the direct path is stored inside of the returning path plates, bigger than the previous ones. Compared to previously proposed solutions, the four stacked plates have a higher tolerance to rotational misalignment but present high undesired cross-coupling effects that translate into a reduction of the power transmitted.

One of the last proposed configuration is a six plate capacitive coupler [14]. As shown in 3.4, the structure is similar to the four plates parallel power transfer, but with two extra outer plates that have the main purpose of shielding the system, reducing the electric field outside of the interested area.

In systems that end up using stacked plates, the undesired cross-coupling between the plates cannot be neglected and need to be considered in the analysis of the electric model. Taking into consideration the four plate model, for example, as there are four plates involved, this leads to six coupling capacitances, shown in 3.5. This initial complex configuration is transformed, as shown in [13] into a simpler circuit model called π model 3.6. To find the relation between input and output, two independent voltage sources are applied respectively to the sending plate and the receiving one. Then, through Kirchhoff's current equations, voltages expression and

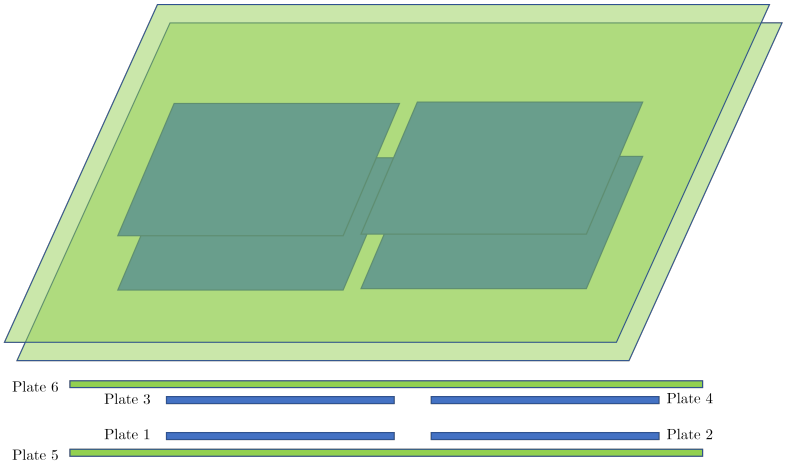

Figure 3.4: Structure of the six plate model

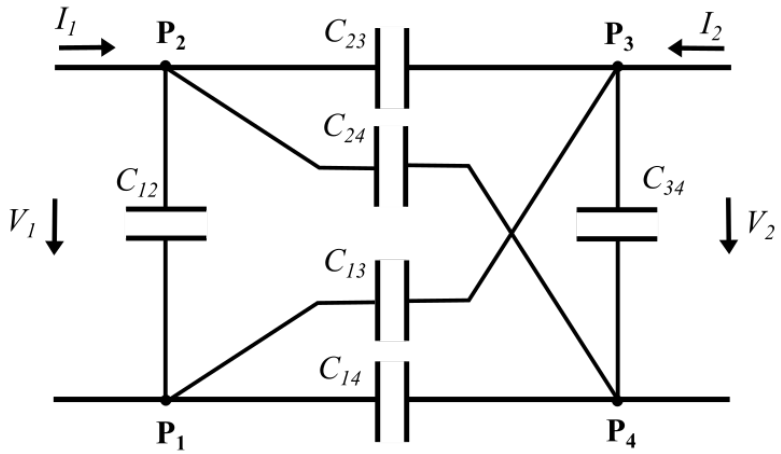

Figure 3.5: Coupling capacitors between plates of the four plate model

equivalent simpler capacitance equation that contains all the coupling capacitance possible are selected. The final model that can be utilized for circuit analysis has only two capacitance C_1, C_2 that represent the primary and secondary side, and C_M that is the mutual capacitance between the two. An in-depth explanation of the π model will be proposed in chapter 5 where the specific model for the case study is explained.

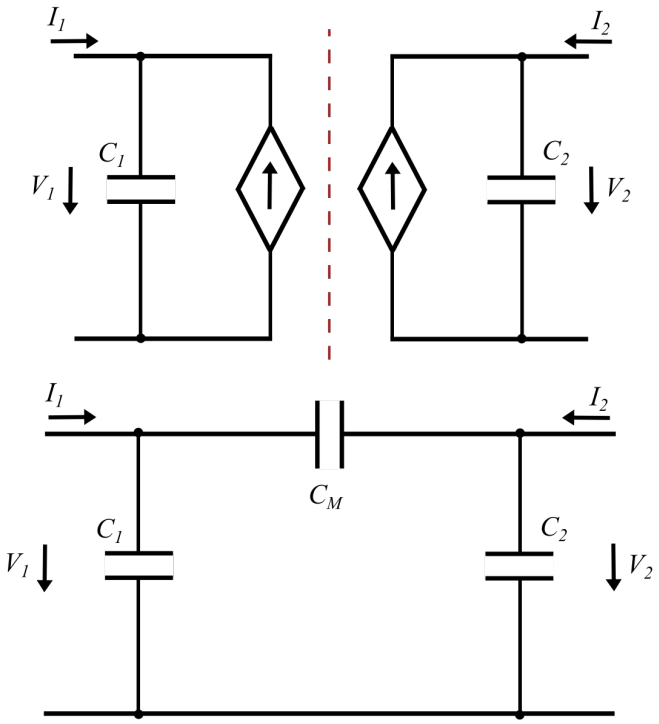

Figure 3.6: Simplified model of the four plate configuration

The capability to transfer a good amount of power comes from having a big capacitance coefficient. This is not always achievable, especially in situations like electric vehicles where the distance between the plates is not negligible. To estimate how much power will be transmitted through the capacitive system, phasor analysis can be performed, and the power transmitted, as explained in [15] is evaluated as:

$$Pout = \frac{\omega^2 RC^2 V_s^2}{2(1+\omega^2 R^2 C^2)} = \begin{cases} \frac{\omega C V_s^2 R}{2} & \text{if } \omega \ll \frac{1}{RC} \\ \frac{V^2}{2R} & \text{if } \omega \gg \frac{1}{RC} \end{cases} \tag{3.2}$$

The working conditions are practically two and depends on the current frequency. The condition of interest is when the frequency of the current is significantly high with respect to the resonance point so that the capacitive coupler looks like a short circuit. When the frequency is very low it acts like an open circuit so the power transmitted drops drastically.

However, taking in exam a case similar to the one presented, it comes out that

in order to have at the output power of 70 W, supposing to having a 1 MHz current flowing, the source voltage becomes unacceptable:

	value	unit
Capacitance	150	pF
frequency	1	MHz
R_{load}	15	Ω

$$V_{in} = 26.45kV \tag{3.3}$$

From this consideration comes out that a simple model like the one previously presented is not feasible.

A solution that can be adopted, first introduced by Tesla, is working at resonance frequency adding inductors in the circuit. This means creating a resonance circuit, as explained in the next session.

3.3 Matching network topologies

The purpose of a matching network is to provide primary voltage and current gain and guarantee reactive power compensation. They are generally built by capacitors and inductors in parallel or in series and their design of them hardly depends on the specific application. The challenge that comes in terms of design is deciding the number of stages and gains of the matching network.

In this section the principal topologies of matching networks are presented.

3.3.1 Simple resonant circuit

The purpose of using inductors is that they have positive reactive power. Adding them to the circuit permits to balance the reactive power coming out from the capacitors reducing the overall losses of the system. Choosing the working frequency, it's possible to dimension the inductor to put the circuit in the resonance conditions.

The most popular topology of compensation network is a single inductor in resonance with the capacitor [16].

$$w_0 = \frac{1}{\sqrt{LC}} \tag{3.4}$$

3.3.2 LC compensation circuit

The further step close to a concrete solution is improving the current design by creating a big virtual inductance without practically having it in the circuit. In order to understand this concept, two transformers can be inserted into the circuit as explained in [15]. The first one increases the voltage and the second one drops it down again by a factor of N, while the current behaves in the opposite way. When the impedance is analyzed after the transformer it gets multiplied by the square turns ratio: in this scenario the capacitive plates on both sides see a bigger inductance compensating the circuit.

At MHz frequency, the transformers can't be used so an implementation with capacitors and inductors is chosen. The first section of the circuit achieves the same

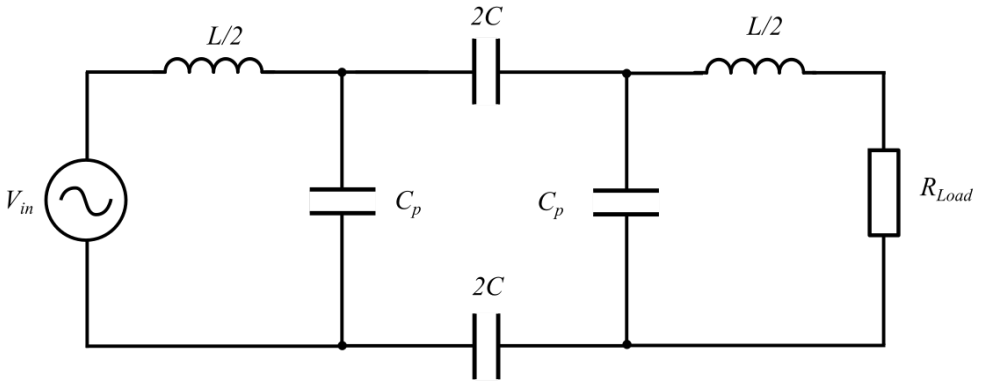

Figure 3.7: LC compensation circuit

voltage step up that can be obtained from a transformer and the same happens on the other side. As explained in [15], the two sections of the circuit can be seen as parallel resonant converters that resonate in parallel and not in series as in the previous configuration. LC compensation is generally used on both primary and secondary sides, resulting in a double-sided LC compensation [17].

3.4 LCL and other topologies

From the previous design, different topologies have been proposed incrementing the number of components and, consequently, the stages of the resonance tanks. Figure 3.8 shows the principal one: LCL, LCLC, CLLC compensation network.

From an analytical point of view, all the circuits can be studied through the

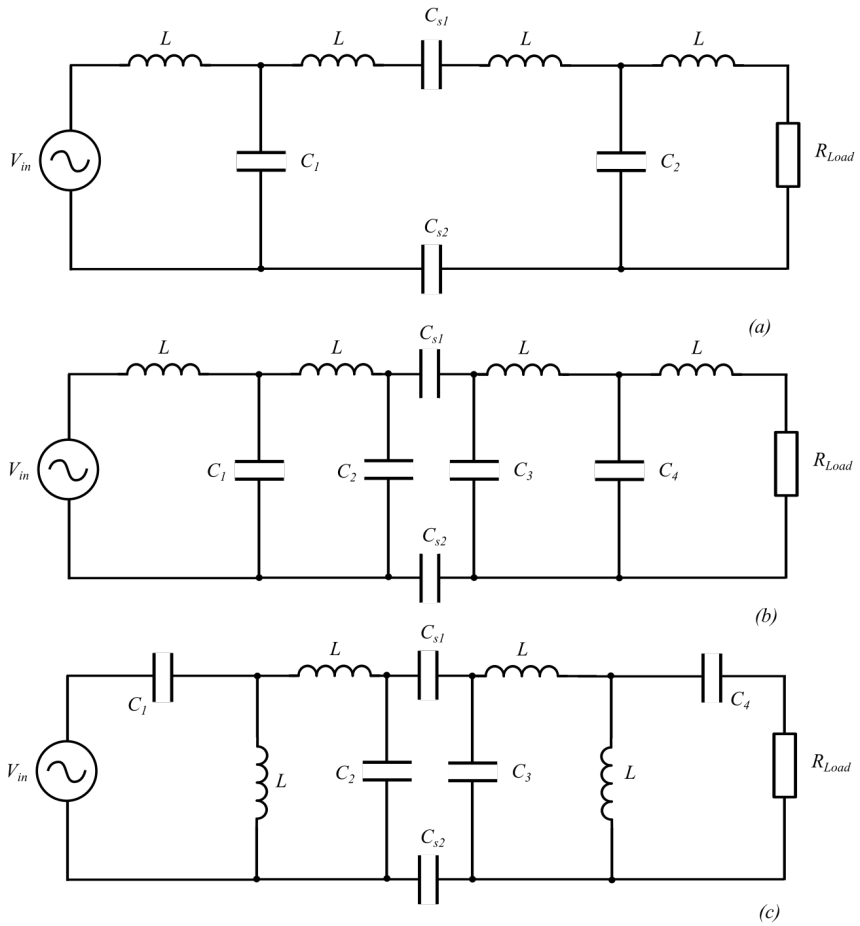

Figure 3.8: fig.(a): LCL compensation network, fig.(b) LCLC compensation network, fig.(c): LCCL compensation network

superposition principle. According to [18], The voltage gain that can be achieved with an LCLC compensation is less than an LCL system, while both are directly dependent on the coupling coefficient k_c. The interesting aspect regarding the third configuration, CLLC, is that his voltage gain is almost independent of the coupling coefficient and higher than the previous ones.

In addition, the angular frequencies corresponding to the maximum voltage gain are different for the three solutions:

$$\omega_{LCL} > \omega_{LCLC} > \omega_{CLLC} \tag{3.5}$$

In conclusion, the choice of a matching network strongly depends on the characteristics of the overall circuit, starting from the available physical space, the costs regarding the components and the property of the system regarding the needed gain, the oscillation frequency and the load.

3.5 Final configuration CWPT

To contextualize the purpose of a matching network, the complete implementation of a CWPT system is shown in 3.9.

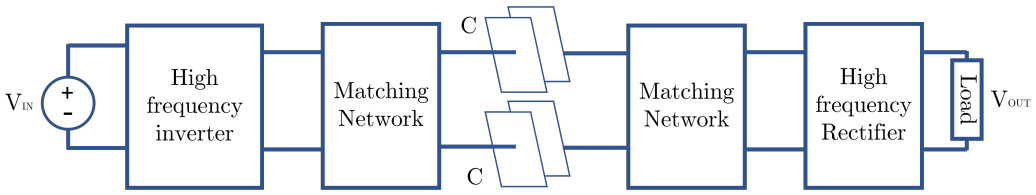

Figure 3.9: Circuit stages of a conventional CWPT system

The new components that come in the configuration are essentially two: an high-frequency inverter and a rectifier.

The presence of the inverter is usually needed because the source of voltage, in general, comes from a DC Battery [19], but also, in the case of an electric motor, the source will still have a frequency extremely low compared to the high frequency needed in the system. On the other side, the presence of the rectifier is needed if the load requires a DC voltage source, as in the case study for WFSM.

Chapter 4

Ansys model and preliminary analysis

To perform a complete analysis of the losses and performance of the capacitive wireless power transfer and the motor, multiple simulations have been carried out using the well-known software ANSYS. For our purposes, the suite ANSYS ELECTRONICS, a comprehensive platform where it's possible to design and simulate different configurations 2D or 3D in the Electromagnetic domain, is used. In this chapter, the procedure to build a reasonable model of an electric machine is described, showing and explaining the results regarding the estimation of the losses and the torque for different geometry configurations.

For the preliminary analysis of the system, two simulations have been used: A 3D and a 2D model designed in ANSYS MAXWELL. The 2D model is used to evaluate the losses and the torque of the motor. The 3D model is first used for preliminary analysis and considerations on the capacitance matrix and later, as explained in chapter 7, to confirm through real measurements that the capacitance calculation is valid and later used for optimization design purposes in Chapter 8.

For the presented project, as there are no previous models similar to this one, the software Flux from CEDRAT has been used to confirm the evaluation of the losses in the plates.

4.1 Introduction to FEA

The software ANSYS makes use of the known Finite Element Analysis. This kind of analysis solves complex problems related to many fields, from elasticity and

structural analysis to electromagnetic simulations, like in this case study. FEA methods are used in complex scenarios where building an analytical model would be extremely complex as a first approach.

The basic principle of the FEA is dividing the model into smaller components, usually tetrahedral forms, and then, using mathematical equations, predicting the behavior of each of those elements. It's evident that the higher the number of tetrahedra the model is divided into, the higher the computational time, especially compared with a full analytical model, but the advantage of this model is that it can analyze very complex geometry, taking in consideration all the properties of the material and combining together different domains, from electromagnetic to thermodynamic domain and so on.

The real challenge in building an FEA analysis model is reducing as minimum as possible the computational time directly related to the number of tetrahedra while still having valuable results based on the reduction of the energy error. The energy error is an evaluation of the mesh density that measure the discontinuity of the field between two near subdivision.

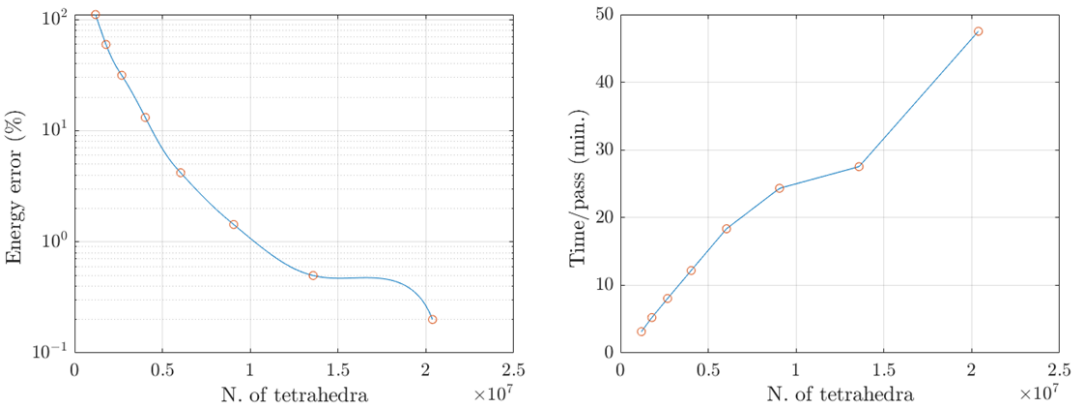

Figure 4.1: Energy error decreasing (left) and time increasing (right) respect to the number of thetrahedra in a general case study

The program goes through multiple passes and at each step, the number of tetrahedral is increased till the energy error is smaller than a certain value decided by the designer. If the model has a solution, the relation between the number of tetrahedra and the energy error is almost linear, as shown in 4.1. For each step, the time of analysis is consequently increasing.

4.2 FE Models setup

The design of an electric motor usually is performed with the program RMXprt from ANSYS ELECTRONICS software suite. This tool allows the selection of the interested machine that the designer want to simulate, starting from the general dimensions to the definition of the number and type of windings. This tool has been only used for the realization of the stator of the machine as is the only fixed component at this stage of analysis. For the other components, the rotor and the capacitive plates, a parametric design has been developed in order to investigate different designs. The chart presented in figure 4.2 gives the main steps needed to set up a simulation correctly,which is valid for a 2D and 3D simulations.

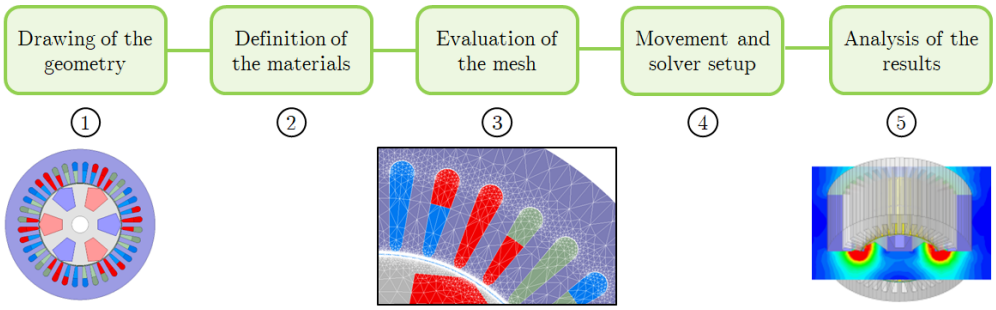

Figure 4.2: Work flow to model design

4.2.1 Geometry description

The main goal of this project is to install the capacitive power transfer plates within the airgap of the machine. This brings few benefits coming from an important reduction of the space occupied by the full machine and creating a WFSM completely contactless.

Figure 4.3 shows the proposed structure. Two pairs of concentric stripped cylindrical plates made from multiple strips are placed within the air gap of the WFSM. Two plates are placed on the stator side (Plate 01 and Plate 02), and two are on the rotor side (Plate 03 and Plate 04). Each plate pair has a total length equal or slightly less than the to half the machine stack length. The plates are distanced with air as a dielectric medium to constitute a rotary air capacitor [20].

In the geometry design procedure a reduction of the losses and an increase of the overall torque needs to be considered as the main goal to achieve. The majority of the losses come from the eddy currents induced by the 75 Hz field. In order to

limit this non negligible consequence, the plates are cut in strips instead of having a full complete sheet. For first analysis, the width of the strips is constant . All the strips have been connected together at the end with a ring of the same material. Further consideration will be provided to justify the plate thickness decision as the insulation thickness.

The plates are separated by the core of the machine with a layer of an insulation material. The rotor and stator core have also to be considered as plates (Plate 05 and Plate 06), as explained in chapter 5.

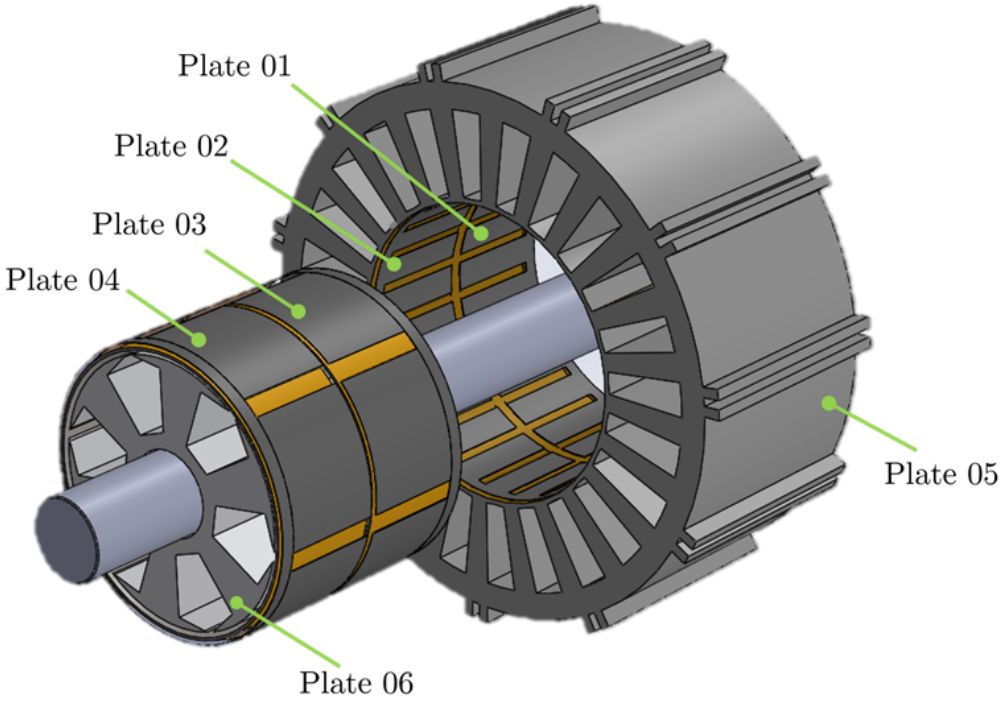

Figure 4.3: 3D representation of the capacitive coupler

The design of the machine started from an existing motor already present in the lab, a Mitsubishi super line SF XR. The machine was born as an induction motor, so only the stator of it can be designed without any parametrization. Dimensions of the rotor and the capacitive plates are object of study so they are defined as variable parameters. In order to avoid an over complicate study of this machine and maintaining the focus on the CWPT system, the net air gap between the static component and the rotational one is fixed and equal to 0.8 mm.

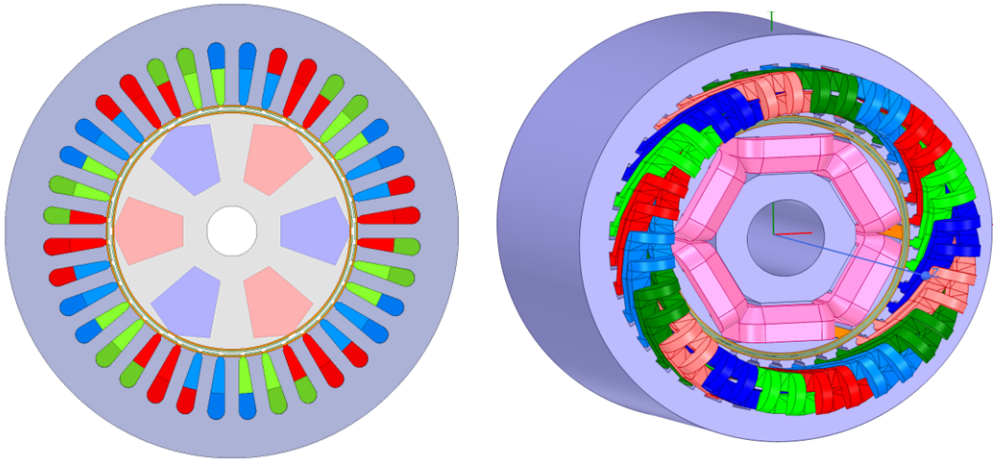

Figure 4.4: 2D and 3D model designed in ANSYS MAXWELL 2D and 3D

4.2.2 Meshing size

The definition of the mesh is extremely important for a correct analysis of the torque and losses. Defining the mesh of the model means deciding the way the program will divide the model in smaller tetrahedral, defining the number of them based on the surface deviation and normal deviation. The program is not always able to generate a good mesh from scratch, but needs some rules or boundary condition imposed by the designer that knows what is the final purpose of that analysis.

For example, if some tetrahedras are too stretched or too skinny those can be eliminated or approximated with smaller elements. The tetrahedra density can be defined over different regions of the model to give more flexibility and to optimize the analysis time especially in engineering applications that often requires three-dimensional mesh studies.

Taking in consideration this study, as the thickness of the plates is small compared to the other elements of the machine (μm vs mm), their meshing needs to be fine enough to obtain valuable results. Over the basic mesh defined by the program itself, ANSYS allows to define specific mesh operation to specific components based on the length of the components, the surface extension or volume of them. In figure 4.5 is shown the meshing plot of the 2D design and the redefined mesh of the plates and the insulation layers.

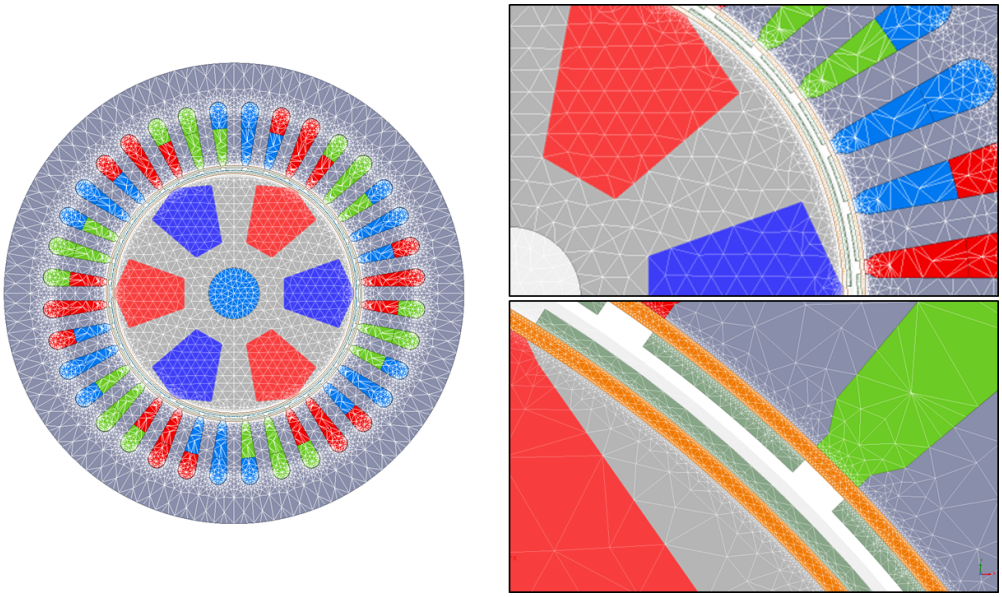

Figure 4.5: Meshing detail of the ANSYS MAXWELL 2D model

4.2.3 Definition of the material

In order to create a realistic and accurate model of the proposed design, a precise definition of the material is needed. From the in-built ANSYS library, the interested material can be selected and assigned to the specific component.

For the proposed design, the materials present are three:

- Laminated steel HF-10: material of the core;
- Steel HF-10: material of the capacitive plates;
- Kapton tape: material of the insulation layers;

4.2.4 Motion setup and solver

The ANSYS MAXWELL Suite permits to perform static and dynamic analysis, in the magnetic or in the electric domain.

An electrostatic analysis in performed on the 3D model. The electrostatic field simulator computes static electric fields due to a stationary charge distribution or based on an applied potential [21]. For this kind of analysis the solver supposes that there is no time variation on the electric quantities. The electrostatic sources can be defined as charges with uniform distribution over a surface or through voltages,

as in this case. In the 3D simulation all the six main components are excited with a voltage source and the capacitance matrix is evaluated.

Differently, a magnetic transient simulation is performed on the 2D design. The magnetic source of magnetic field can be dependent on moving or non moving currents, voltages or magnets and circuits. The transient solution is based on the evaluated quantity of the magnetic field H and on the current distribution J.

Performing this kind of simulation gives access to multiple derived quantities such as torque, position, flux linkage and losses. In this study, 2D simulations are performed to evaluate the losses in the capacitive plates deriving from the stator field current and from the one flowing in the plates themself.

4.3 Design considerations

4.3.1 Geometry rotor optimization

The optimization of the rotor geometry has been performed by another member of the team through the software Flux with the algorithm Global response search method (GRSM). This optimization solution is based on a response surface: every iteration the optimization loop generates a different design. The first iterations of generated design are spaced in all of the bounded geometry space in order to ensure a good balance while looking for the optimum solution and then increasing the number of simulation in the best region. Each iteration have a specific number of design points. Every point is independent from each other so this permits the algorithm to analyze them in parallel reducing the computation time.

The input optimized parameters are the geometry of rotor slot and pole and the control angle of the stator current. The interested objective function considered include the maximization of the torque, the minimization of the ripple and the current density of the rotor constrained to 4.5 A/mm^2. Figure 4.6 shows the evaluated objective function.

Figures 4.7 and 4.8 show the variation of the average torque and the ripple respect to each evaluation. The first fifty iterations are used by the algorithm to have an overall view of the geometry space to be optimized. Subsequently, an optimum region of solutions is identified and more designs are evaluated in that region. When the design doesn't show any more significant changes in the geometry and the objective functions are almost constant the optimization is completed. Figure 4.9 shows the initial geometry and the final geometry of the rotor.

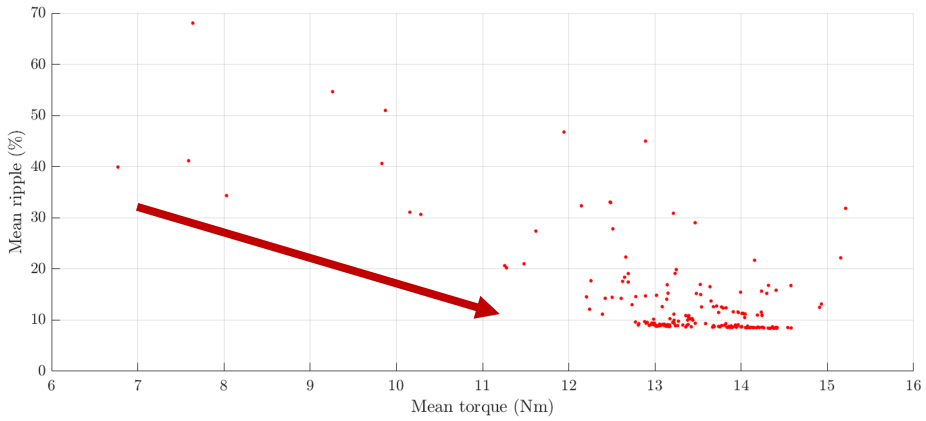

Figure 4.6: Variation of torque ripple and max torque across different evaluations showing optimum point

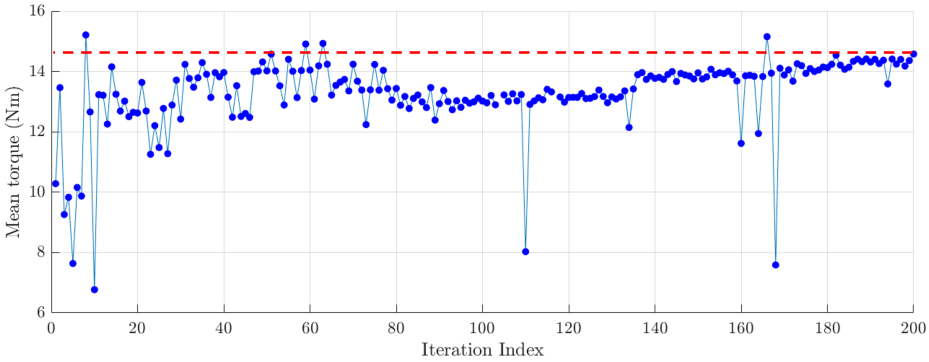

Figure 4.7: Variation of average torque with each evaluation showing average torque maximization

4.3.2 Stator and rotor windings

To simplify the assembly of a first prototype, a full pitch winding scheme has been proposed. However, after few simulations and optimization of the rotor shape, the ripple of the machine was significantly high, about 17%. The torque ripple is generated by harmonics of the magnetic field due to non idealities of it. This imperfections generates vibrations that directly reflects on the efficiency and stability of the machine [22]. It is mandatory during first design stages to reduce as much as possible the simulated torque ripple considering the mechanical vibrations present into a real model.

In order to avoid too many troubles related to an high ripple, the winding

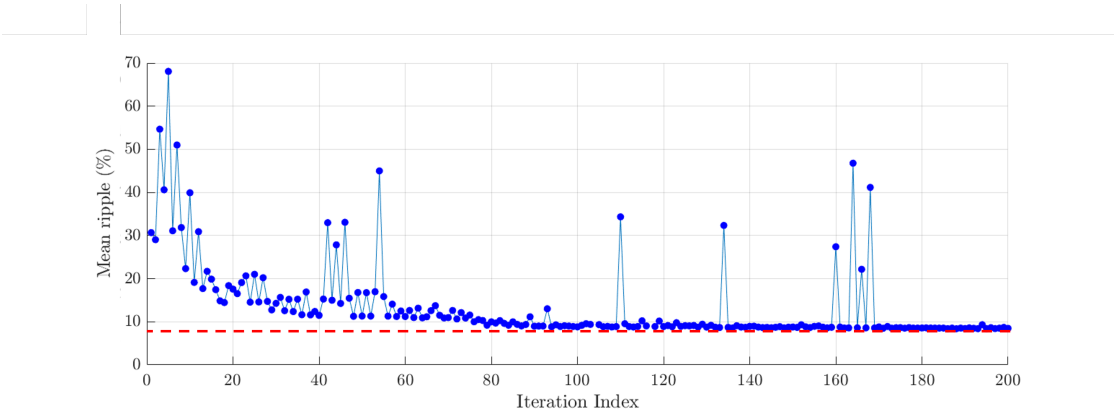

Figure 4.8: Variation of torque ripple with each evaluation showing torque ripple minimization

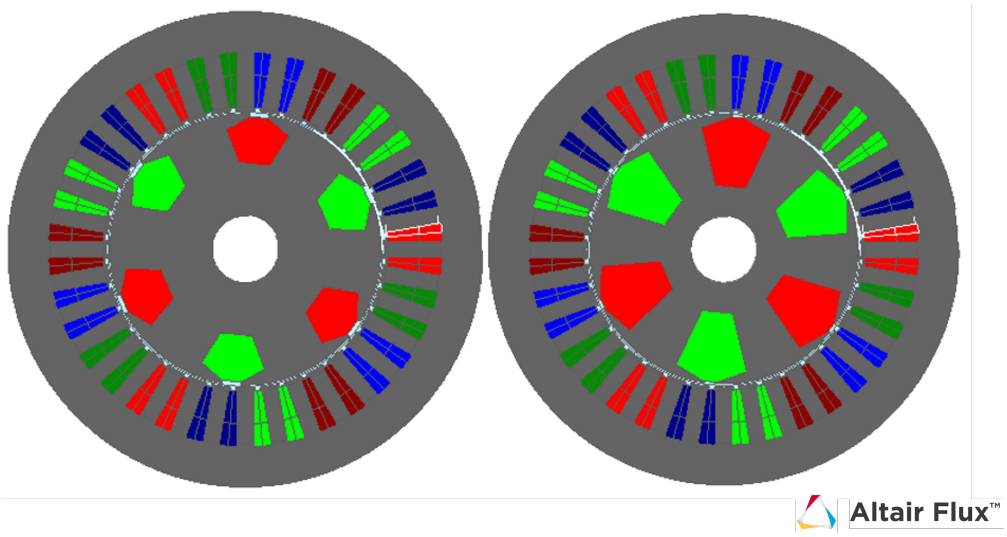

Figure 4.9: Rotor geometry before (left) and after (right) optimization

configuration has been changed to an half pitch winding, shown in figure 4.10.

As explained in [23], in the full pitch configuration the phase windings take the full slot area, while in the short pitch configuration they are wrapped around each pole with each winding taking almost half of the slot area. This configuration is more complicated in terms of construction, but reduces significantly the ripple of the machine. As shown in 4.11, a comparison between the two configuration is presented. The ripple is reduced of around 7%.

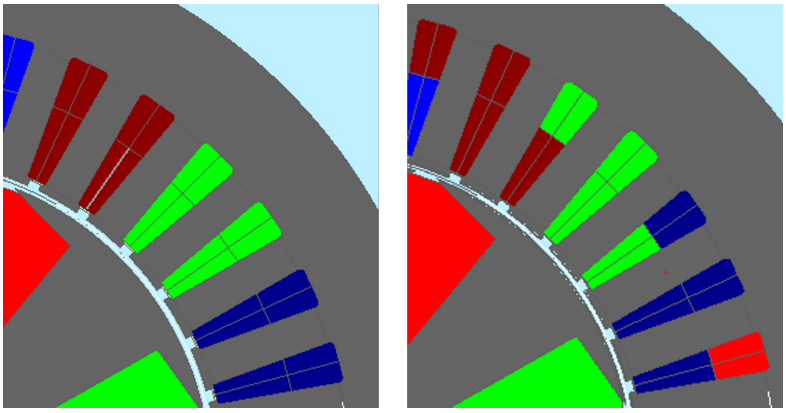

Figure 4.10: Flux model comparison between full pitch and half pitch windings

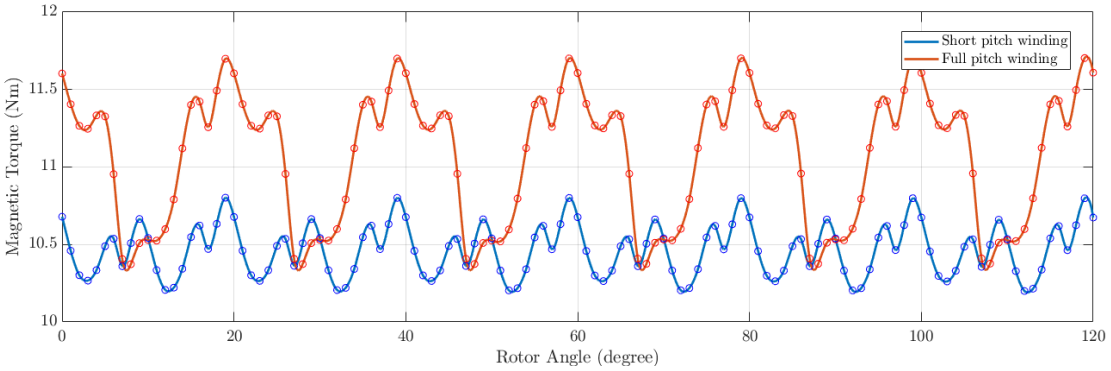

Figure 4.11: Comparison configuration between short pitch winding and full pitch winding

4.4 Loss analysis

For the purpose of having a vivid analysis on the impact of inserting capacitive plates inside an electrical machine, an exhaustive losses analysis has been performed through Finite Element Analysis.

In the table 4.1 are presented the principal losses due to the addition of the plates in the motor. The principal source of losses come from the stator field current at 75 Hz and the current that flows in the capacitive plates at high frequency frequency. In the design of an electric motor it's fundamental to take care of the losses that are generated due to the presence of electromagnetic field.

In a machine the losses can be divided in two section, the losses coming from the stator and rotor called *core losses* and the losses in the windings normally called *copper losses* [24].

Frequency	Stator	Rotor	Stator plates	Rotor plates
75 Hz	Hysteresis eddy currents	Hysteresis eddy currents	Hysteresis eddy currents	Hysteresis eddy currents
1 MHz	Hysteresis eddy current	Hysteresis eddy currents	conduction loss	conduction loss

Table 4.1: Summary of the main losses present in the model

4.4.1 Core losses

The machine core is generally made of a magnetic material. Magnetic material has a low reluctance so it generates a good path for the magnetic flux to flow. The eddy current losses are in general small due to a low conductivity of the material itself and for lamination of the core.

Indeed, the losses can be divided in three parts using the known loss separation method (LSM) [24]:

- Eddy current losses: this loss depends on the circular currents that are generated into a material while exposed to a time varying magnetic field. This kind of loss is evaluated by Ansys [25] for core material by:

$$p_c = k_c(fB_m)^2 \tag{4.1}$$

- Hysteresis losses: it's the typical loss of a ferromagnetic material, it describe the magnetization of a component due to the presence of an external field in the form of a residual magnetization, evaluated with:

$$p_h = k_h f B_m^2 \tag{4.2}$$

- Additional losses: usually called excess losses, deriving from some spatial harmonics of the magnetic field, evaluated through the equation:

$$p_e = k_e(fB_m)^{1.5} \tag{4.3}$$

Where k_x are coefficients depending on the material characteristics, B_m is the maximum value of the magnetic field and f is the frequency.

In picture 4.12 and 4.13 are shown the amount of losses derived from an evaluated machine design. As explained in [21] the core loss evaluation it's a post-processing

calculation, based on already calculated transient magnetic field quantities. It is applicable for the evaluation of core losses in steel laminations. As can be noticed the Hysteresis component takes more time to reach the steady state value: this is due to the material that has to complete a full hysteresis loop before reaching steady state and the effect is more evident on the stator compared to the rotor. The stator is close to the varying magnetic field and it's more affected by this time-varying action. As the field is rotating at $75Hz$ it reach steady state after one full electric cycle at around $13ms$. On the rotor the effect is extremely reduced.

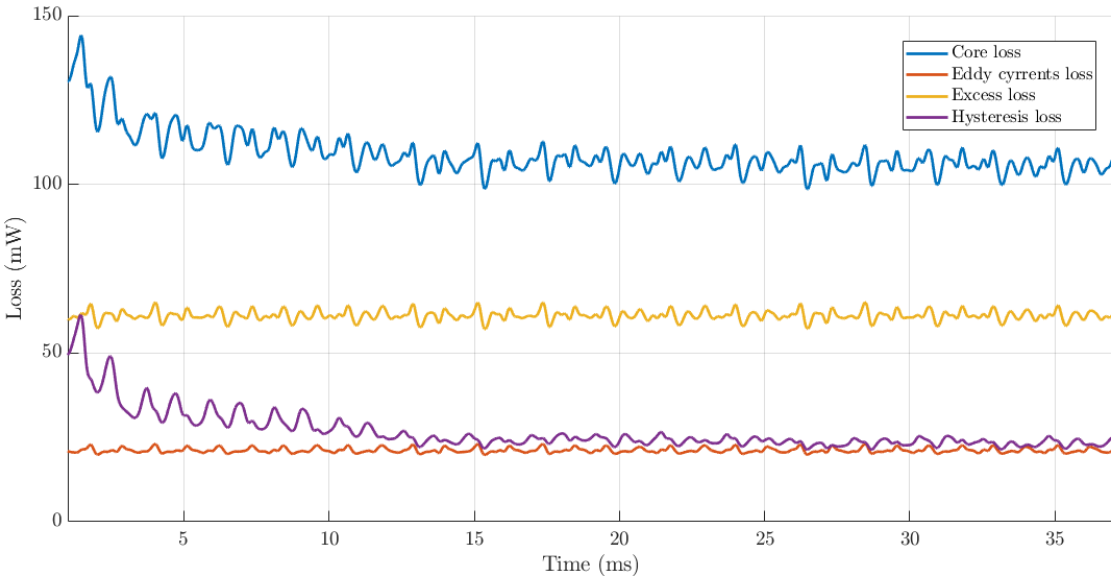

Figure 4.12: Core losses on the rotor core for one electrical cycle

1 MHz core loss

The losses in the stator and rotor core due to the 1MHz current flowing in the strips are present, but negligible as will be shown in the chapter 6. The current frequency is high, but the the magnetic field generated is very small due to a small current flowing in the capacitive strips, as shown in

4.4.2 Losses in the plates

A different analysis should be performed to evaluate the losses in the capacitive plates. The source of losses in these components come from two sources: losses due

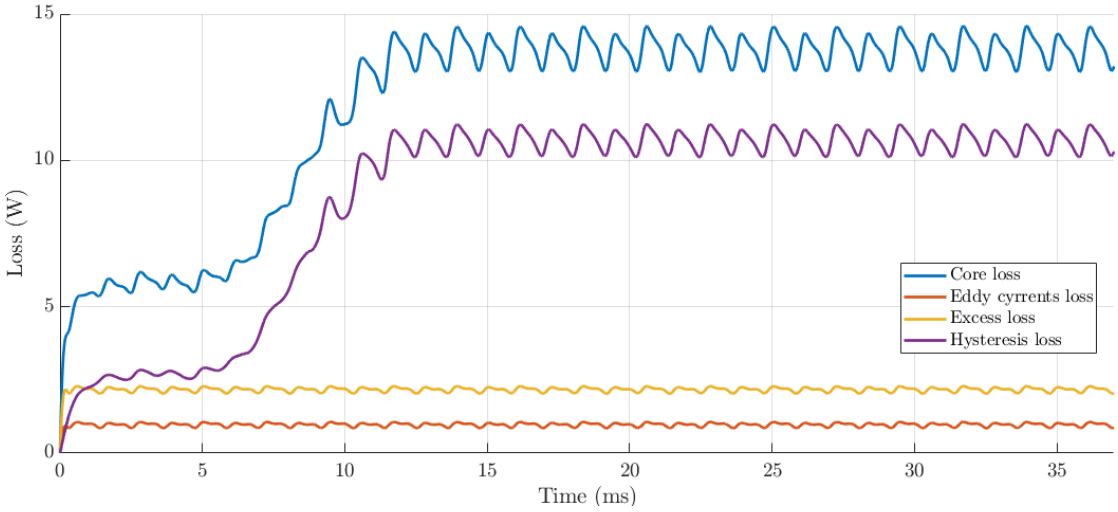

Figure 4.13: Core losses on the stator core for one electrical cycle

to 75 Hz frequency and losses due to 1 MHz frequency. As the frequencies are very different from each other, 2 different simulations needs to be performed.

To evaluate the losses, the plates are modeled as a conductive component. The core loss model can only be used for components that are not supposed to have current flowing inside.

The losses present are due to:

- Eddy currents: deriving from the 75 Hz field;
- Proximity effect: in presence of multiple conductors near each other, like multiple capacitive strips, the distribution of the currents of the first conductor is directly affected from the current flowing in the other conductors. In other words, the current will flow in a smaller region of the conductor;
- Skin effect: this effects represents the tendency of an alternating current flowing into a conductor to distribute such that the current density on the outer region of the conductor is higher compared to the inside. Also this effect reduce the effective area where the current can easily flow, increasing the overall losses. This effect is evident while having an fast-changing field.

Losses due to 75 Hz magnetic field

Figure 4.14 shows the profile of the losses generated in one strip over one electrical cycle at 75 Hz frequency. The peak of the loss comes in correspondence of the peak

of the magnetic field on the strips. As a consequence, the eddy currents will be higher for that amount of time, as shown figure 4.15, directly proportional to the square root of the magnetic flux density [26] 4.4:

$$P = \frac{\pi^2 B_p^2 d^2 f^2}{6k\rho D} \tag{4.4}$$

As can be noticed, the value of the eddy currents is not negligible even though the

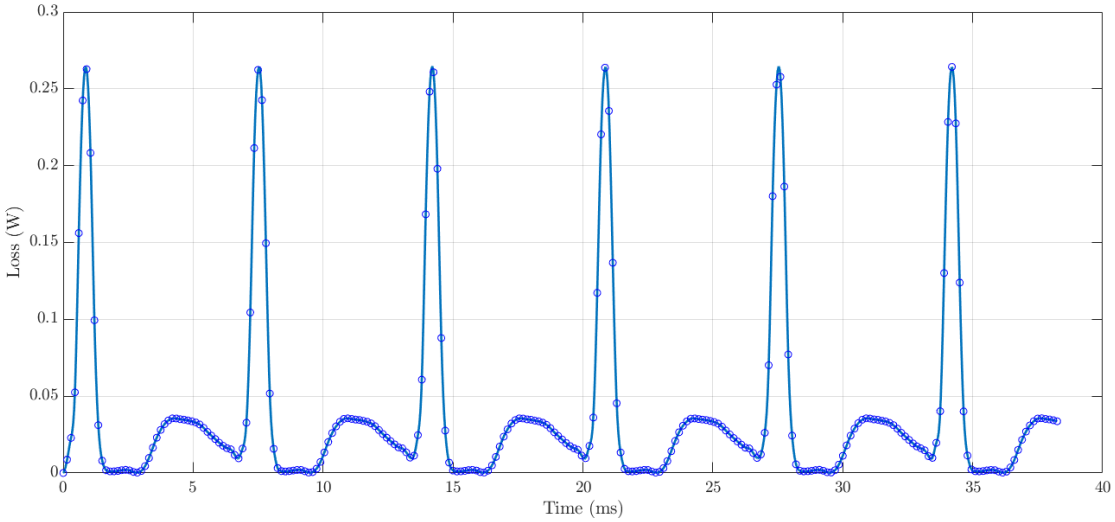

Figure 4.14: Capacitive strip losses over one electrical cycle due to 75 Hz current

material has a low conductivity: this is related to the absence of lamination in the plates.

Figure 4.15 shows the effect of the 75 Hz field over the strips, showing the circulating currents inside the coductor.

Losses due to 2 MHz frequency

A second analysis is performed to evaluate the losses coming from the current flowing inside the strips. For this analysis, the capacitive strips are modelled as solid conductors and a current is injected inside them. From figure 4.16 The skin effect can be noticed. An estimation of this effect is performed through the equation 4.5 that represent the point where the current, starting from the side of

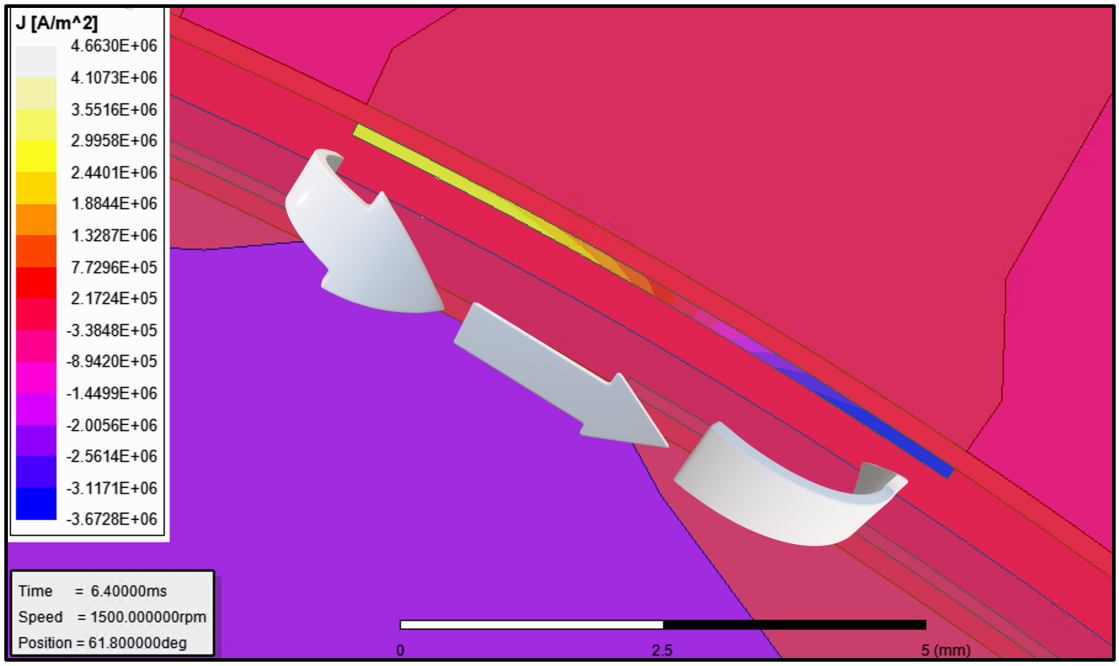

Figure 4.15: 3D simulation showing the eddy current circulating in one strip

the conductor, reaches the 37% of the value over the surface:

$$\delta = \sqrt{\frac{\rho}{\pi f \mu}} = \sqrt{\frac{\rho}{\pi f \mu_r \mu_o}} \tag{4.5}$$

where ρ is the resistivity of the material, f is the frequency, and μ is the permeability of the material. Fig. 4.17 shows the losses due to the near magnetic field, previously called proximity effect. All this kind of losses are small and negligible, as will be shown in chapter 6

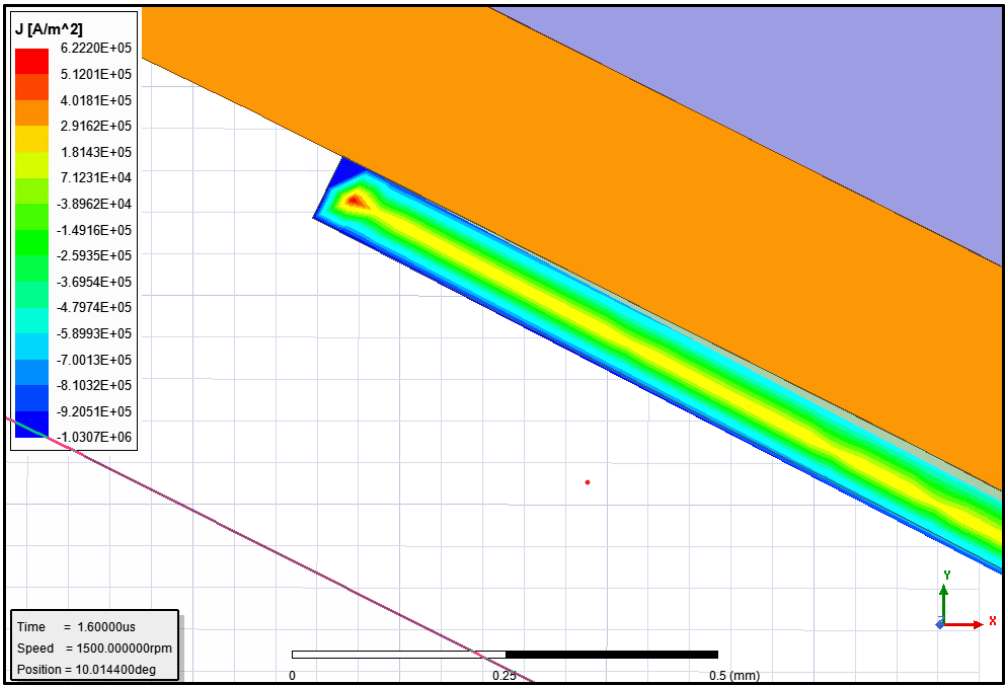

Figure 4.16: 3D simulation showing the skin effect over one capacitive strip

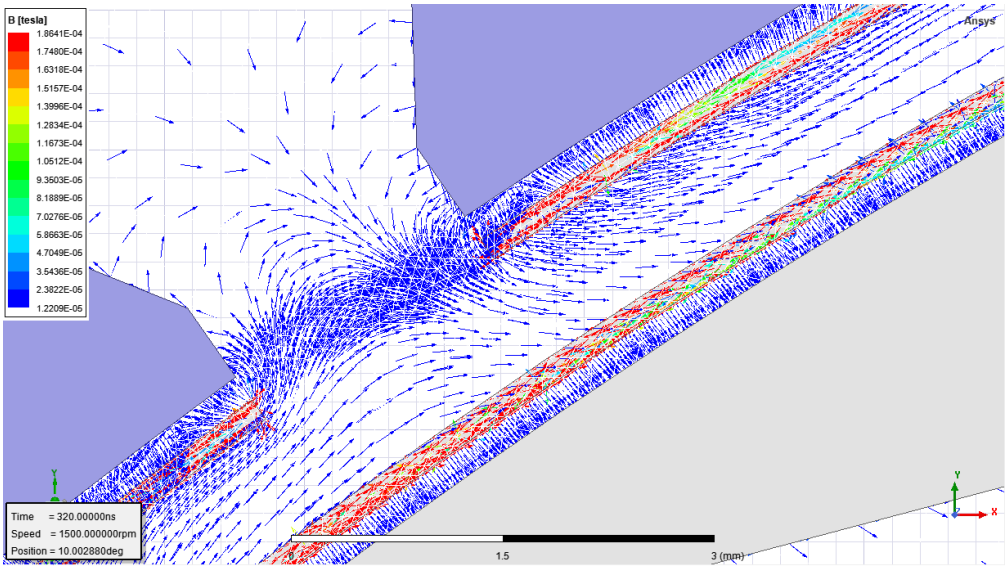

Figure 4.17: 3D plot showing the magnetic flux density around the capacitive strips with a 2 MHz frequency current flowing in the strips

Chapter 5

Analytical model of the CPT and selection of the matching network

In this chapter, the analytical model of the capacitive power transfer system and the matching network topology are presented. For the CPT system, the six plate model previously introduced in chapter 3 will be developed and two compensation topologies will be analyzed and compared.

5.1 6 plate model

The system that we are considering is shown in Plates P_1, P_2 and P_5 are respectively the two plates on the stator side and the stator machine core, then P_3, P_4 and P_6 represent the secondary side and are the plates positioned on the rotor and the rotor core itself.

In 5.1 are shown all the couplings present in the model. As the considered model has six plates, this will end up having 15 coupling capacitances. The majority of them, in our case, represent some minor cross-coupling effects that, as will be shown later, will be neglected to simplify the analysis. The voltages on the sides V_1 and V_2 represent the voltages on the primary and secondary side, while the voltage V_3 represent an imaginary excitation between the stator and rotor core, used to simplify the equations, but as there is no current flowing I_3 will be considered as zero.

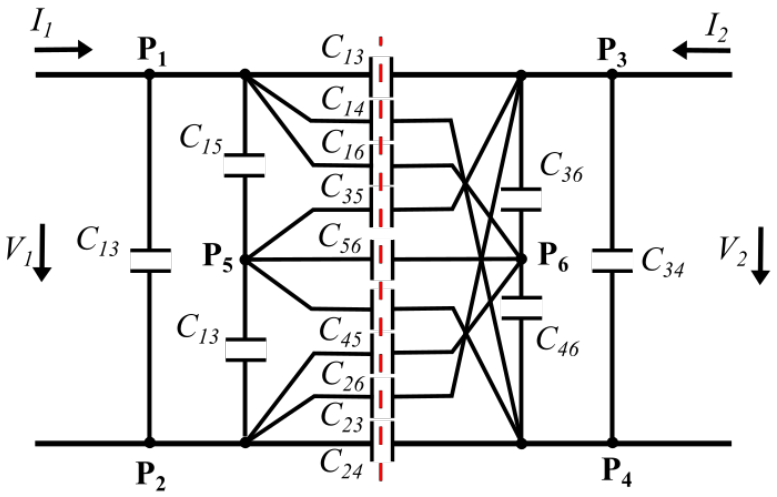

Figure 5.1: Six plate complete model

In order to find the π model equation that describes the model, first, a 3-port model is proposed [14]. Through the relation between the three-port model and the full capacitance model, the π model will be found. In this scenario, the relations between voltages and currents are expressed in:

$$\begin{cases} I_1 = j\omega C_1 V_1 - j\omega C_{M12} V_2 - j\omega C_{M13} V_3 \\ I_2 = -j\omega C_{M21} V_1 + j\omega C_2 V_2 - j\omega C_{M23} V_3 \\ I_3 = -j\omega C_{M31} V_1 - j\omega C_{M32} V_2 + j\omega C_3 V_3 \end{cases} \tag{5.1}$$

Where C_1, C_2 and C_3 are the self capacitances of the ports while the others represent the mutual capacitances between each other.

To solve the system, analytical equations based on Kirchoff's law are computed. To understand the procedure to find C_1, we can set V_2 and V_3 equal to zero having from the three-port model:

$$C_1 = \left. \frac{I_1}{j\omega V_1} \right|_{V_2=V_3=0} \tag{5.2}$$

To extract the equation of V_1 from 5.1 the same voltages can be shorted finding C_1:

$$C_1 = C_{12} + C_{01} \tag{5.3}$$

where C_{01} derive from a combination of the capacitances represented in 5.1 through simplifying the circuit as shown in 5.2:

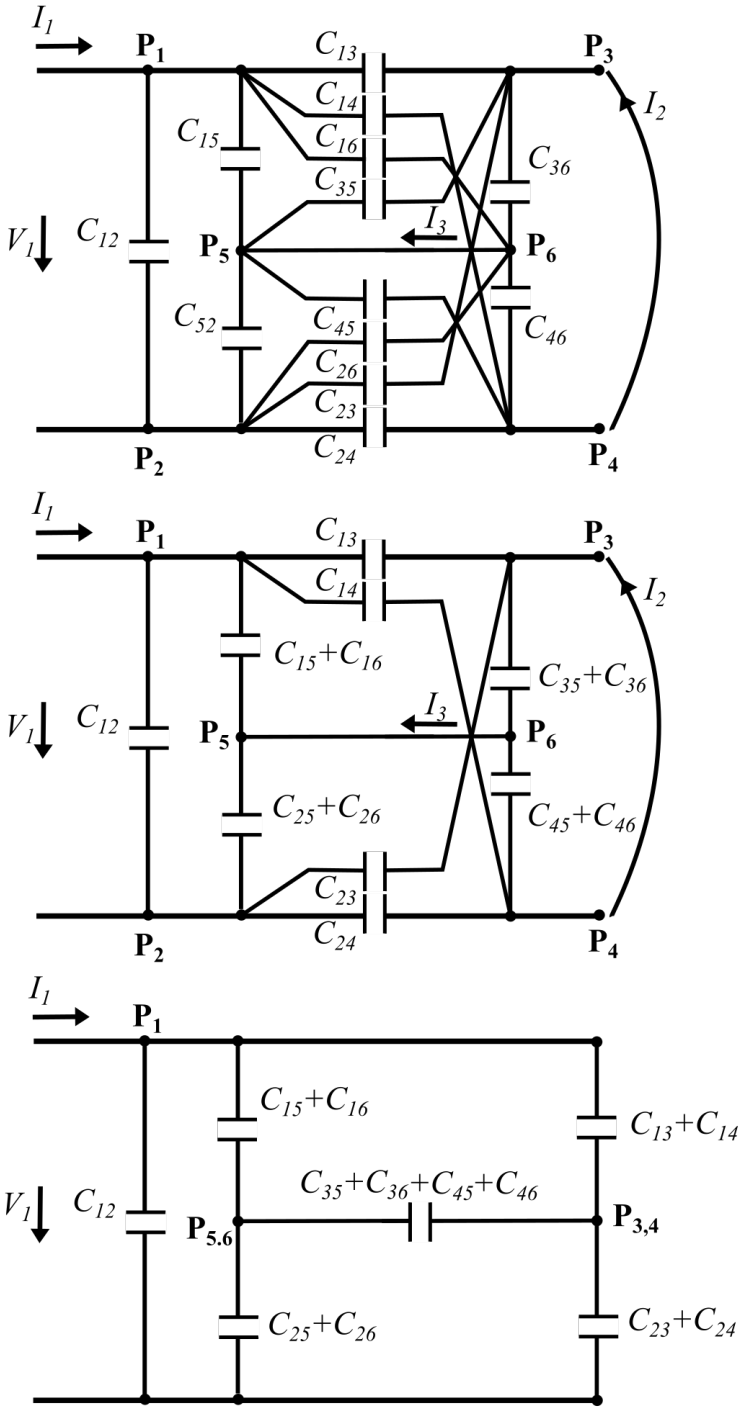

Figure 5.2: Simplification circuit steps

$$\begin{cases} C_{a1} = C_{13} + C_{14} \\ C_{b1} = C_{23} + C_{24} \\ C_{c1} = C_{15} + C_{16} \\ C_{d1} = C_{25} + C_{26} \\ C_{e1} = C_{35} + C_{36} + C_{45} + C_{46} \end{cases} . \tag{5.4}$$

$$\begin{aligned} C_{01} =& \frac{C_{e1}\left(C_{a1} + C_{c1}\right)\left(C_{b1} + C_{d1}\right)}{C_{T1}} \\ &+ \frac{C_{a1}C_{b1}\left(C_{c1} + C_{d1}\right) + C_{c1}C_{d1}\left(C_{a1} + C_{b1}\right)}{C_{T1}} \\ C_{T1} =& C_{e1}\left(C_{a1} + C_{b1} + C_{c1} + C_{d1}\right) \\ &+ \left(C_{a1} + C_{b1}\right) \cdot \left(C_{c1} + C_{d1}\right) \end{aligned} \tag{5.5}$$

As the current I_3 is equal to zero, the system 5.1 can be expressed as:

$$\begin{aligned} I_1 &= j\omega\left(C_1 - \tfrac{C_{M13}^2}{C_3}\right)V_1 - j\omega\left(C_{M12} + \tfrac{C_{M13}C_{M23}}{C_3}\right)V_2 \\ I_2 &= -j\omega\left(C_{M12} + \tfrac{C_{M13}C_{M23}}{C_3}\right)V_1 + j\omega\left(C_2 - \tfrac{C_{M23}^2}{C_3}\right)V_2 \end{aligned} \tag{5.6}$$

and then solved for:

$$\begin{cases} C_{1\mathrm{eq}} = C_1 - \frac{C_{M13}^2}{C_3} \\ C_{2\mathrm{eq}} = C_2 - \frac{C_{M23}^2}{C_3} \\ C_{M\mathrm{eq}} = C_{M12} + \frac{C_{M13}C_{M23}}{C_3} \end{cases} \tag{5.7}$$

The equations 5.7 are then converted in the π model 5.3 that let us to analysed it analytically as the four plate model presented in [13]:

$$\begin{aligned} C_{1\mathrm{eq}\pi} &= C_{1\mathrm{eq}} - C_{M\mathrm{eq}} \\ C_{2\mathrm{eq}\pi} &= C_{2\mathrm{eq}} - C_{M\mathrm{eq}} \end{aligned} \tag{5.8}$$

Where the coupling coefficient will be:

$$K_c = \frac{C_{M\mathrm{eq}}}{\sqrt{C_{1\mathrm{eq}\pi}C_{2\mathrm{eq}\pi}}} \tag{5.9}$$

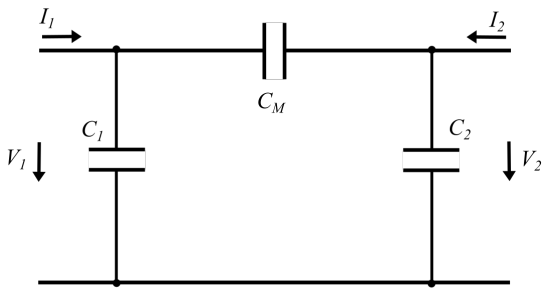

Figure 5.3: π model of the six plate model

5.2 Matching network model

For study and investigation purposes, two matching topologies have been implemented and studied, an LL and an LCL compensation network, shown in figure 5.4. The results related to the two chosen topologies are presented in chapter 6

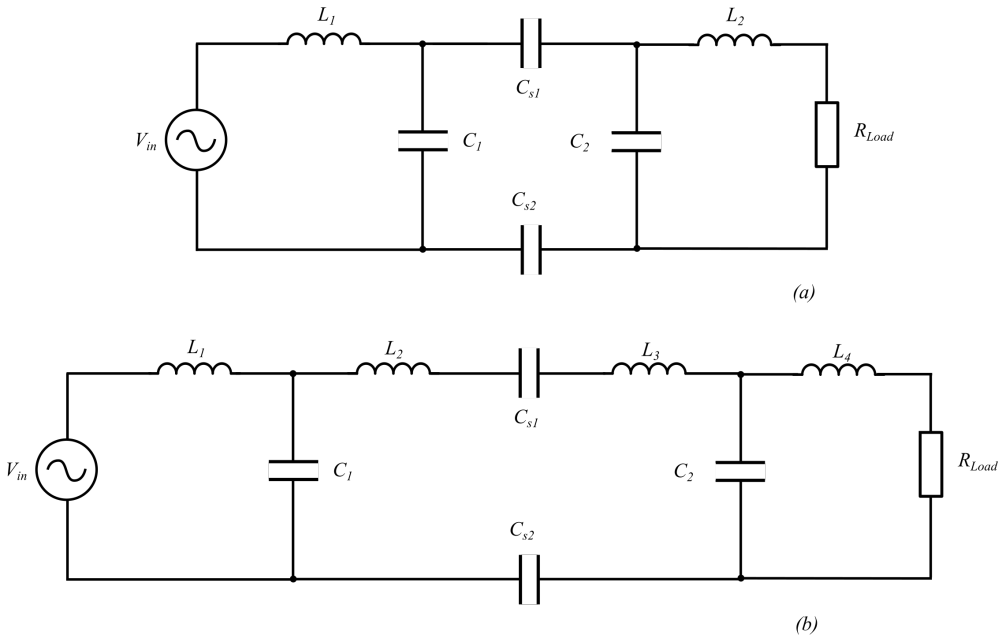

Figure 5.4: (a): LL compensation network, (b): LCL compensation network

Chapter 6

Simulation Results

This section aims to show the behaviour of the losses and the capacitive coupling related to the variation of selected parameters of the capacitive plates. The variation of the geometric dimensions of the strips affect the losses in the machine and the feasibility of the matching network associated with it. At this stage, two compensation topology have been selected and discussed. Different Pareto front are presented. In chapter 8 the optimization procedure to find the Pareto fronts is exhaustively explained.

To maintain the focus on the CWPT, a net air gap of 0.8 mm between the plates is chosen. The involved parameters in the analysis are the thickness of the plates and the thickness of the insulation layer. Consequently, the rotor radius accommodates to maintain the net air gap. The choice of maintaining a net air gap is forced by maintaining a good amount of Torque transmitted in the machine.

Other parameters like the distance between plates on the same side is not considered because, as the cross coupling between them is very low, the effect is negligible. A parameter that is will be involved in later analysis is the width of the strips.

6.1 Losses in the machine

The first analysis are conducted varying the insulation thickness and the plate thickness in a range between 0.05 mm to 0.3 mm. The width of the strips is fixed to the width of the stator tooth, for the capacitive strips laying on the stator, and the width of rotor pole, for the one on the rotor side. This range has been chosen in order to avoid to analyze points that do not have any practical sense. 80 different

design configurations have been evaluated. Three simulations are involved in this analysis: a 3d model used to extract the capacitance matrix of the model, a 2d simulation needed to evaluate the losses from the 75 Hz current of the stator and a 1 MHz simulation to evaluate the losses in the plates.

6.1.1 75 Hz losses

Figure 6.1 shows the losses trend on the stator and rotor plates due to the 75 Hz magnetic field: as the plate thickness increase the losses increases consequently, almost linearly. An increase in the overall volume of the strips increase the volume where the eddy currents can flow, according to 4.4.

A slight variation of the insulation thickness is also noticeable: as the insulation thickness increase the losses in the strips reduces consequently. A bigger insulation thickness bring the plates away from the stator windings and consequently are less affected by the varying magnetic field. This is also the reason why the losses in the rotor strips are always smaller compared to the losses in the stator strips. the flux leakage is generated by the interaction between the stator field and the rotor DC field. As the rotor plates are rotating synchronously with the stator field, this will translate in less losses in those plates.

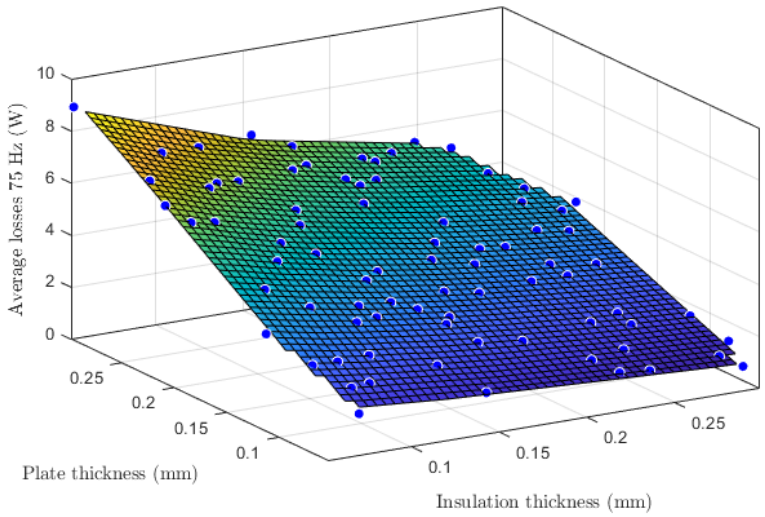

Figure 6.1: Losses coming from 75 Hz magnetic field

6.1.2 Matching network losses

As mentioned in [17], [15], the majority of the losses in a system that include a CWPT system come from the matching network and especially from the inductors. As mentioned before, an LL and LCL compensation have been evaluated and later compared. Figure 6.2 shows that the insulation thickness is the main parameter that affects the losses in the plates while the plate thickness has a negligible effect. It's evident from figure 6.2 that for an insulation thickness smaller than 0.2 mm the losses becomes too high. This trend can be simply explained referring to the

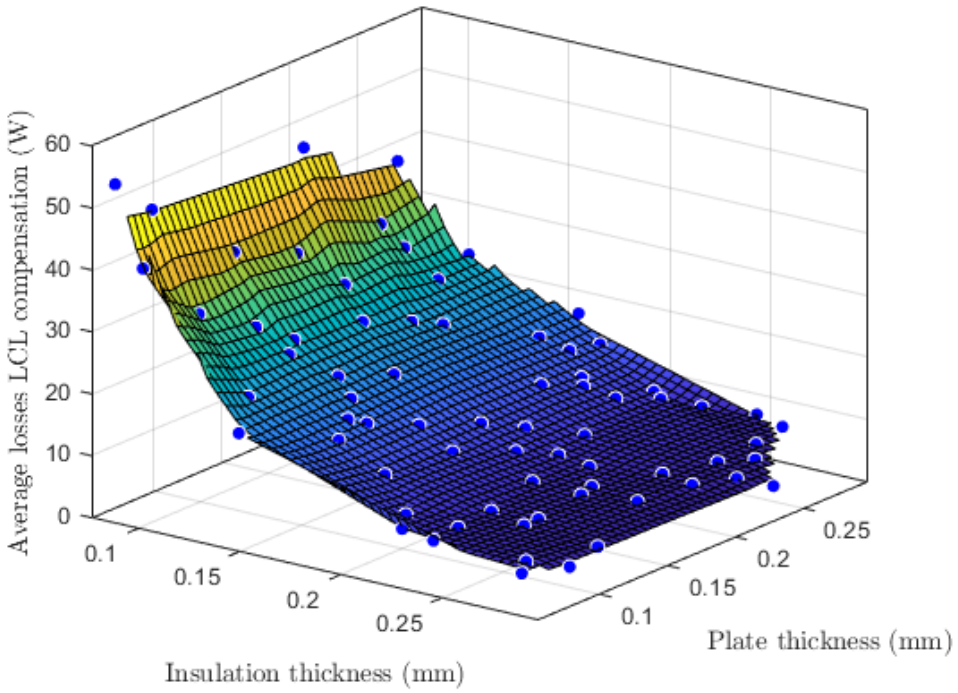

Figure 6.2: Losses coming from LCL compensation network

previously explained six capacitance model in chapter 5.

The reduction of the insulation layer increase the capacitance value between the main plates and the core. This needs to be compensated by the matching network, as larger value of the inductors is required. The plate thickness doesn't affect the losses in the matching network. This is consistent because the capacitive plates of the components doesn't depends on the volume of the plates but just on the surface of them.

6.1.3 2 MHz Losses

The overall losses deriving from the current flowing in the strips are shown in 6.3. As previously expected, the losses are small especially for insulation values bigger than 0.2 mm. This is related to the small value of current that flows inside the strips, ≈2-5 Ampere.

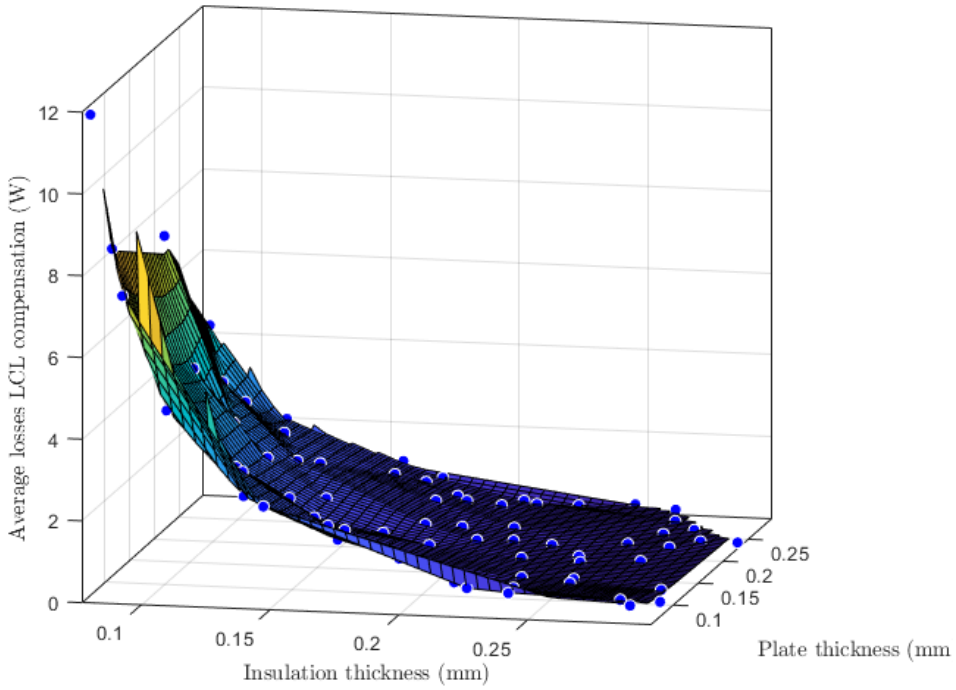

Figure 6.3: Losses coming from 2 MHz current

6.2 WFSM for loss comparison

In order to perform some considerations on the results obtained a comparison with a conventional WFSM machine is performed.

The comparison evaluate the differential efficiency between the two machines and the torque, normalized with respect to the standard machine.

To evaluate the efficiency of the machine, it is compared with a motor presenting the same geometry with a minimum air gap of 0.8 mm set. As shown in chapter 2, the principal components of a WFSM are equal to our system, so we don't need to

make a comparison of them.

The missing component in the presented design is the component that makes the connection between the static part and the rotational component. Many solutions have been suggested as explained in chapter 2: In the comparison machine a common set of carbon brushes is used, taking the values and performance from the *Mersen* company [27].

Slip rings can be modeled as resistance of the brushes and a voltage potential drop of the carbon surface and the metal surface. This characteristic comes from the properties of the two materials and, based on a standard, this voltage drop can be evaluated on a scale from extremely low to high.

Electrographic brushes are choosen, with a medium contact drop and low medium friction coefficient, which means low electrical loss. This kind of brush is normally used in synchronous and asynchronous machine applications.

The final loss is the sum of the Ohmic loss coming from the resistance and the voltage drop:

$$P_{loss} = RI^2 + V_{drop}I \tag{6.1}$$

as the current flowing in the DC field winding will be equal to 2.3 A

$$\text{Ohmic loss} = 13\mu W \approx \textit{negligible}$$

$$\text{Voltage drop loss} = 5.3W \tag{6.2}$$

$$P_{loss} \approx 5.3W$$

6.3 Pareto fronts

After the evaluation of more than 80 different configurations, two Pareto front for both the configuration LL and LCL are presented, with respectively color scale showing the effect of the insulation thickness and the plate thickness in the different design 6.4.

on the x axis the torque is normalized respect to the comparison machine Torque with a net air gap of 0.8 mm. on the y axis is shown the differential efficiency

between the two configurations, calculated through the equation 6.3.

$$\begin{aligned} \text{Differential efficiency} &= \frac{P_{out}}{P_{out}+\text{Compared loss}} \\ \text{Compared loss} &= \text{Total loss} - \text{Losses comparison machine} \end{aligned} \tag{6.3}$$

From 6.4, 6.5, as the insulation thickness increase the efficiency increase but the

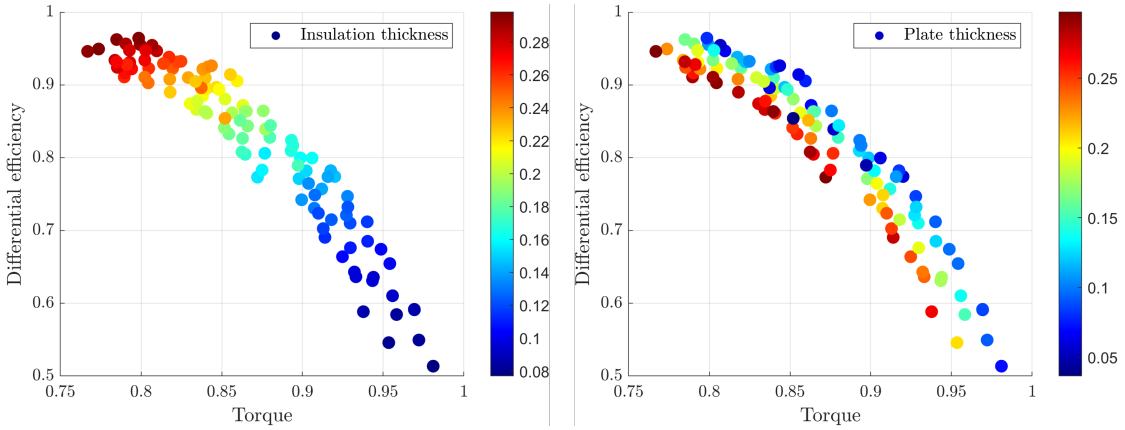

Figure 6.4: Pareto front LCL compensation

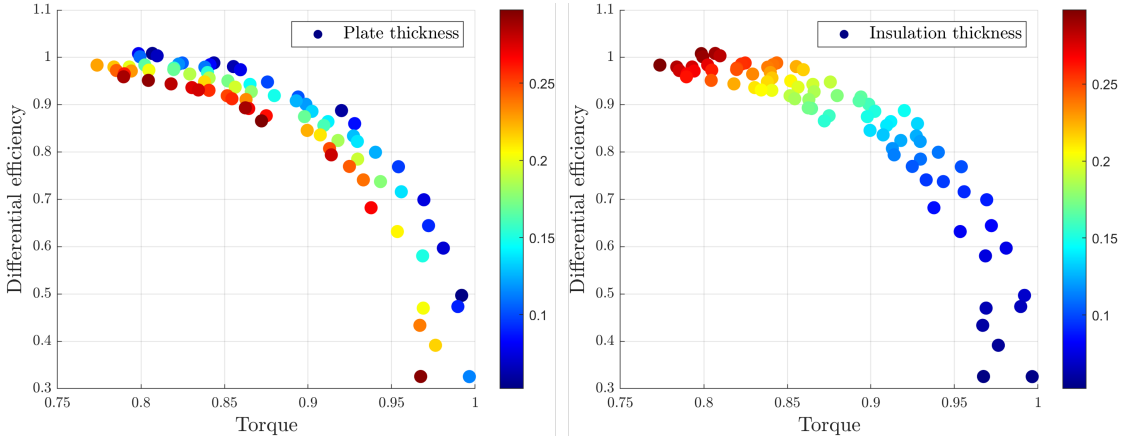

Figure 6.5: Pareto front LL compensation

torque drops drastically. An increasing in the insulation thickness determine a bigger region where the magnetic flux density B is not flowing into a magnetic material. The plate thickness, indeed, is not directly influencing the efficiency or

the Torque, but a small plate thickness, increase the overall performance.

Comparing the Pareto front coming from the two configuration is evident how the LL configuration is a better choice in terms of efficiency compared to the more complex LCL configuration.

A closer look to three evaluation points on the Pareto front shown in 6.6 is presented in figure 6.7 and 6.8 The matching network is predominant in the total

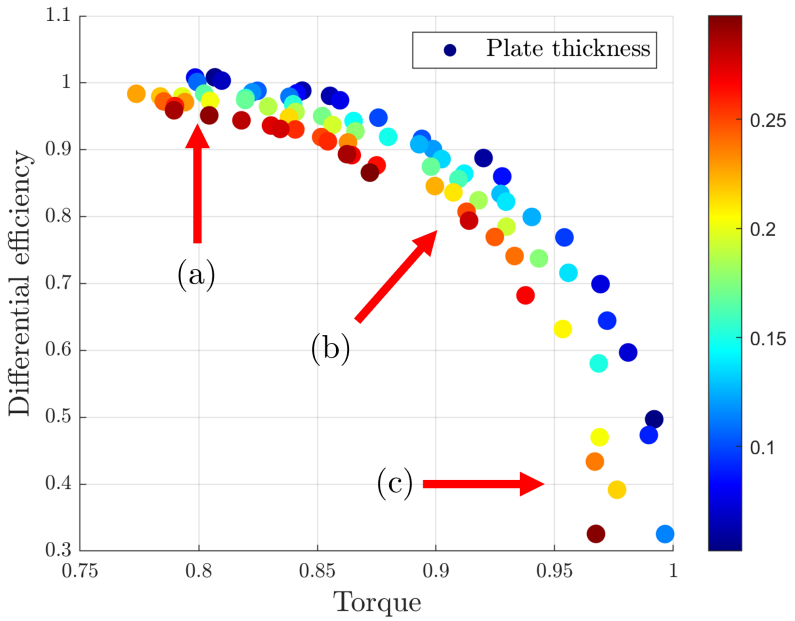

Figure 6.6: Pareto front showing the three evaluated points

sum of losses in both configurations. The losses due to the 2 MHz field are negligible while the losses coming from the 75 Hz field are still consistent.

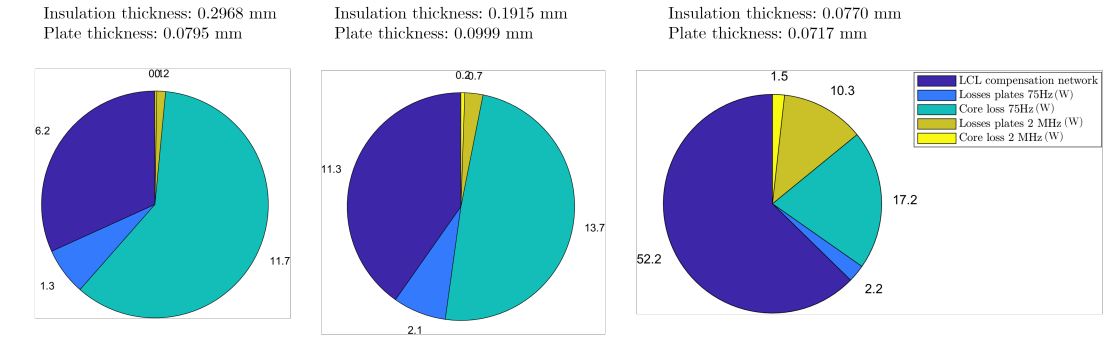

(a) Differential efficiency: 0.96
Torque: 0.78

(b) Differential efficiency: 0.87
Torque: 0.86

(c) Differential efficiency: 0.54
Torque: 0.97

Figure 6.7: Pie chart of three evaluated point with an LCL compensation network

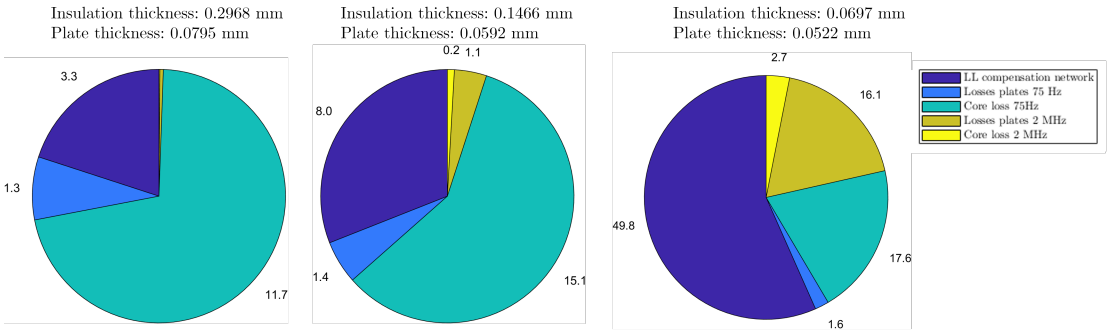

(a) Differential efficiency: 1.02
Torque: 0.8

(b) Differential efficiency: 0.91
Torque: 0.89

(c) Differential efficiency: 0.49
Torque: 0.99

Figure 6.8: Pie chart of three evaluated point with an LL compensation network

Chapter 7

Experimental Results

In this chapter, the manufacturing of an experimental prototype is described in detail. Consequently, results from power tests are presented to support the analysis. The challenges encountered during the prototype development have also been discussed in detail.

7.1 Construction of the prototype

The prototype is designed Mitsubishi super line SF XR motor. The stator dimensions are mentioned in table 7.1. The stator of the machine was used in its original form. However, the rotor is fabricated using CNC machine.

Stator	Value	Unit
Inner radius	50	mm
Outer radius	80	mm
Length	85.5	mm
Material	HF-10	laminated
36 slots	25 windings	/slot
Frequency	75	Hz

Table 7.1: Fundamental data of the motor Mitsubishi super line SF XR

Figure 7.1 and table 7.2 show different material layers that are present in the model and their relative nominal dimensions. As the final geometry of the rotor is yet to be defined, an additional layer of metal (d) is glued on a plastic rotor to simulate its capacitance effect.

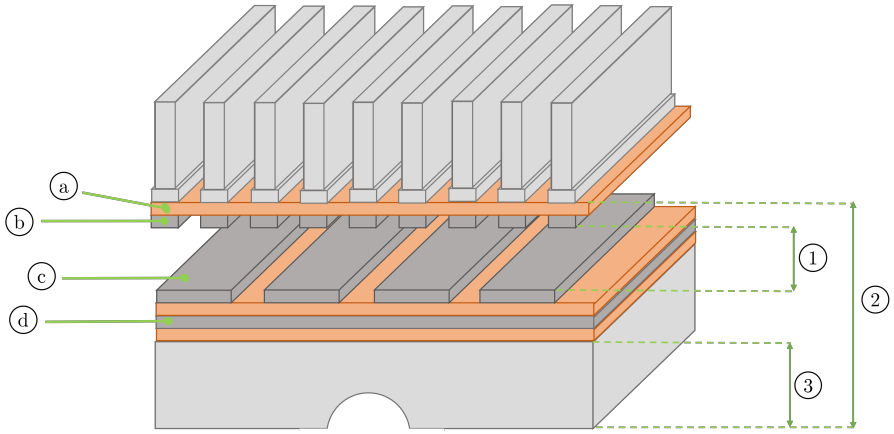

Figure 7.1: Material prototype layers

Reference	Component	Thickness	Unit
a	Kapton tape	0.2060	mm
b	Stator plates	0.127	mm
c	Rotor plates	0.127	mm
d	Rotor sleeve	0.127	mm
1	Air gap	0.8	mm
2	Stator radius	50	mm
3	Rotor radius	48.311	mm

Table 7.2: Geometric layers thickness

Initial prototype model of the rotor was built through a 3D printer *Ultimaker S3* 7.2. However, the print result was not not precise in terms of the diameter in comparison with the airgap of the machine of 0.8 mm.

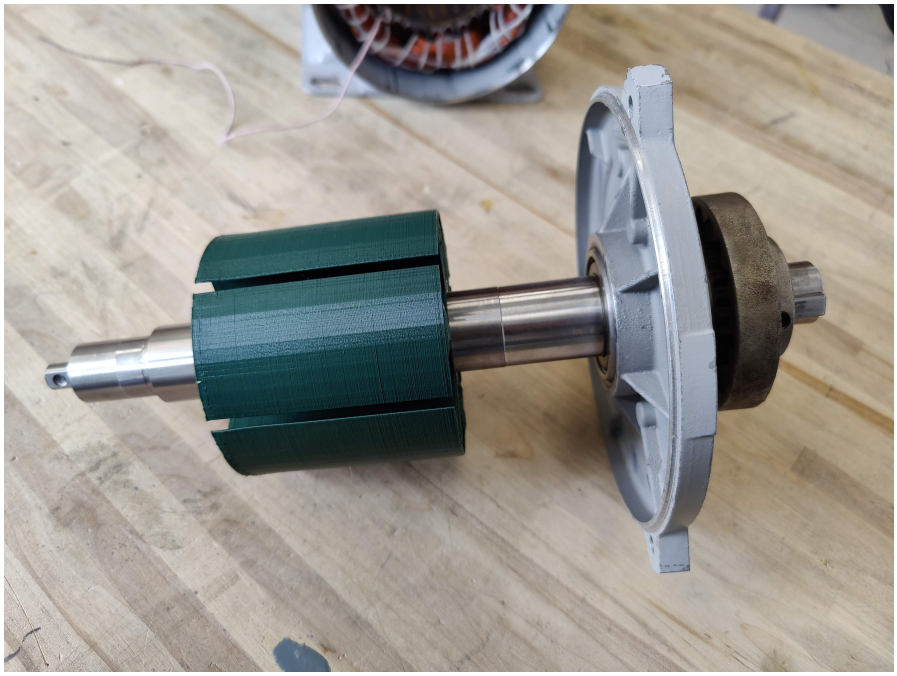

Figure 7.2: 3D printed rotor

The rotor is modeled with multiple disks packed together made of High Density Polyethylene, HDPE, plastic cut through a *Shopbot* CNC machine. As the machine's resolution is ±0.006 mm, the result is acceptable, and shown in 7.3.

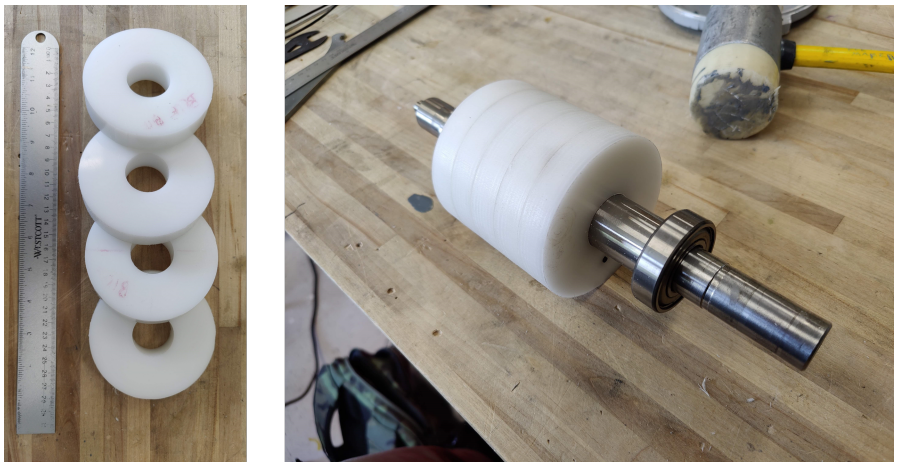

Figure 7.3: *Shopbot* CNC machine rotor

Also, the capacitive plates present on the rotor and stator sides have been cut through the CNC machine 7.4:

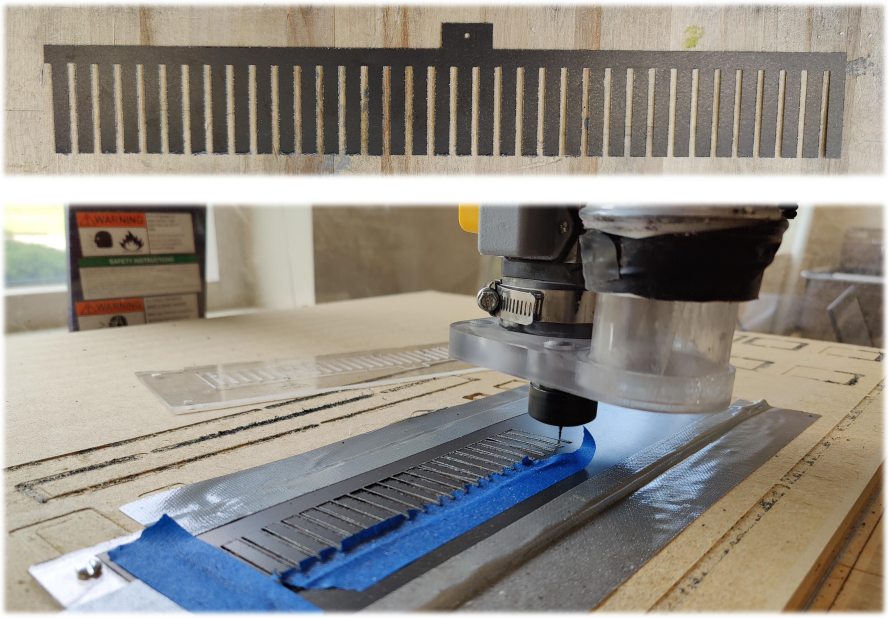

Figure 7.4: Capacitive power transfer strips cut through *Shopbot* CNC machine

The layers of Kapton tape, rotor metallic sleeve and coupler plates have been fixed on the rotor, and shown in figure 7.5.

The same procedure has been employed for the stator core and shown in 7.6.

Litz wire of adequate length has been soldered with all 6 plates of the coupler structure to measure the capacitance matrix, as shown in 7.7:

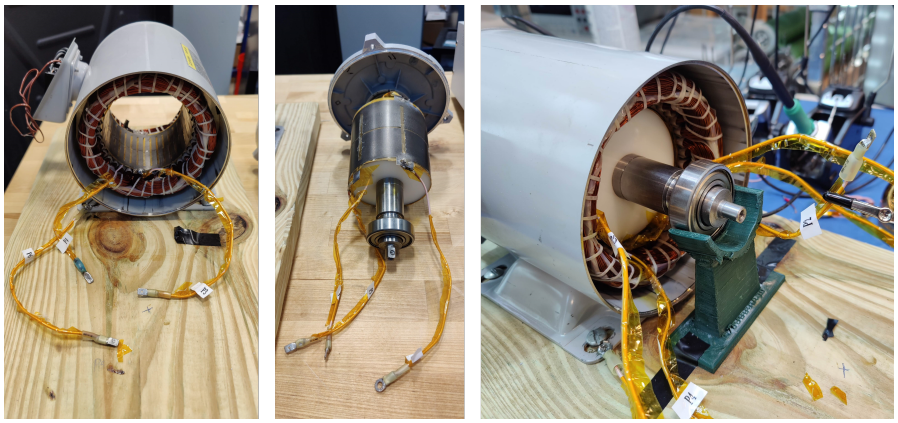

Figure 7.7: Prototype components: stator, rotor and final assembly

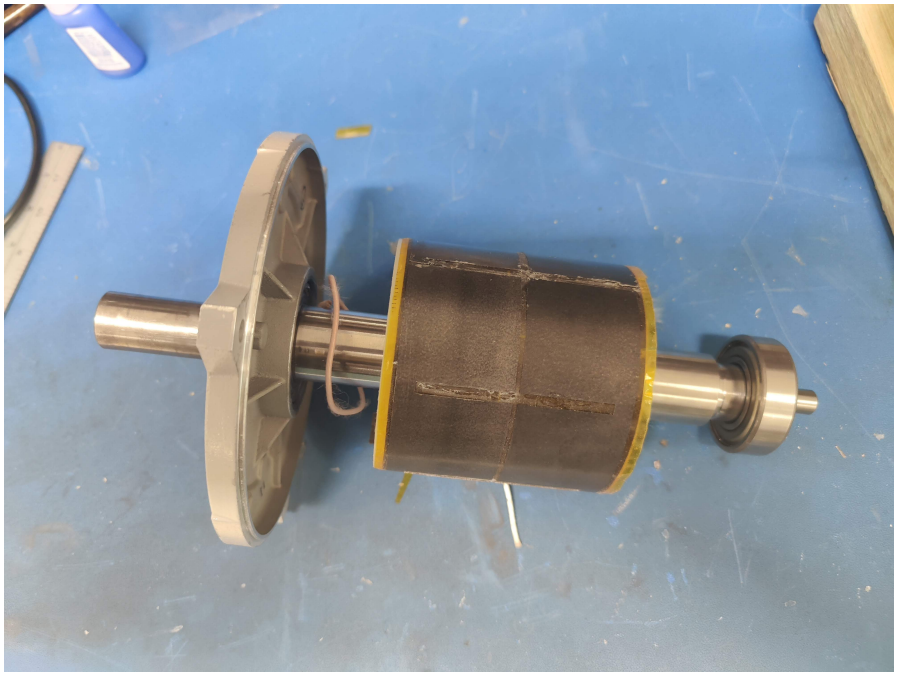

Figure 7.5: Rotor with capacitive strips glued on it

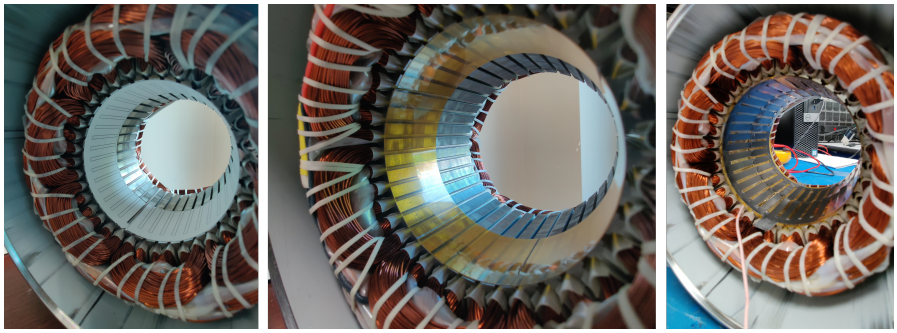

Figure 7.6: Stator strips positioning procedure

7.2 Calculation of the permittivity of the Kapton tape

At first, the electrical permittivity ε_r of the Kapton tape has been experimentally tested.

To evaluate this, a simple capacitor made of two plates with the desired layers of Kapton tape between the plates is made 7.8:

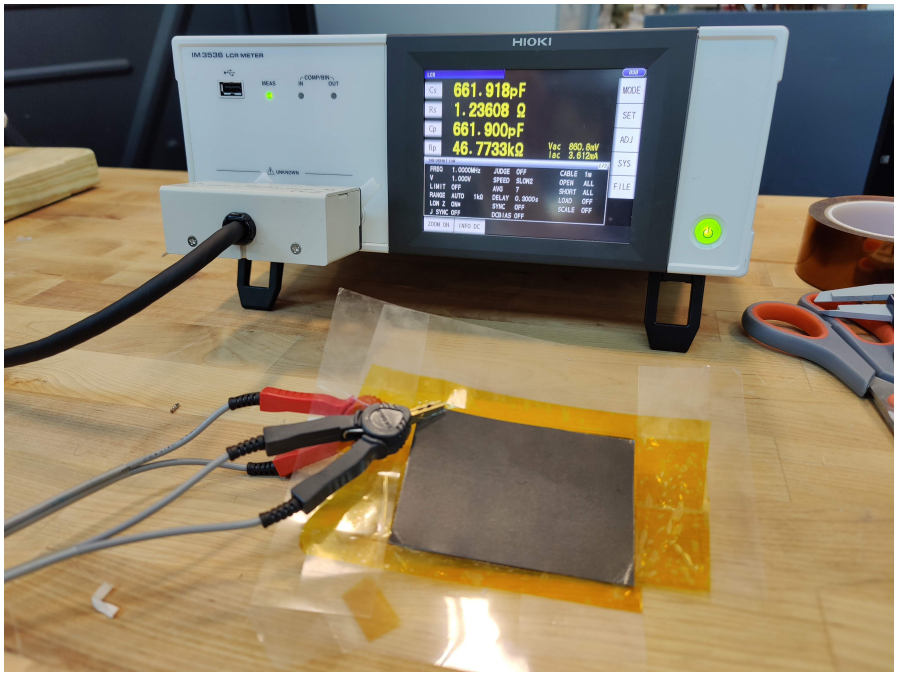

Figure 7.8: Permittivity test setup

The thickness of the plates is confirmed with a caliber. Table 7.3 describes the geometric dimensions. Using the fundamental capacitance equation, we can find

Component	Dimensions	Unit
Kapton tape thickness	0.2060	mm
Plates thickness	0.127	mm
Area plates	70 x 88.5	mm^2

Table 7.3: Geometry dimension permittivity test

the value of ε_r that comes very close to the evaluated one at 1MHz.

Component	Dimensions	Unit
Evaluated C	661.9	pF
Datasheet 1 kHz ε_r	3.50	F/m
Evaluated ε_r	3.42	F/m

Table 7.4: Results permittivity test

7.3 Capacitance matrix calculation

A primary test to evaluate the capacitance values coming from the prototype is performed and the results compared with the simulated case study.

For this first test, a Hioki IM3536 LCR Meter impedance analyzer is used for this evaluation. As the instrument is extremely sensitive, the probes needs to be as distant as possible from each other to avoid as much as possible any mutual inductance effect.

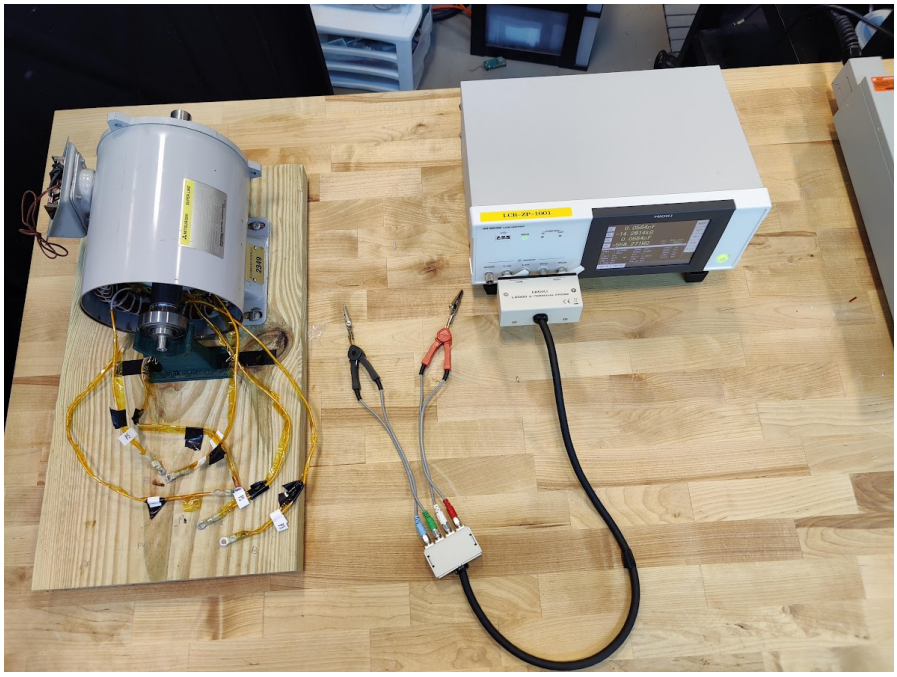

Figure 7.9: Capacitance matrix calculation setup

The first step was the tuning the LCR meter performing a short circuit and open circuit connection between the instrument's probe at the operational frequency and, after that, proceeding with the calculation of the capacitances. The instrument has just two probes and, as six plates are present as presented in 3, 15 capacitances are there, which means solving 15 different equations shortcircuiting different plates together. With a total of six plates, the number of combinations are 31. At first, a system of 15 equations chosen from the 30 previously evaluated has been solved, but the results were not acceptable. Few small parassitic capacitances where generating noise inside of the equation's system ending into unrealistic solutions.

Taking in consideration the capacitance matrix coming from the simulation 7.5,

the capacitance are classified into 4 groups:

- C_{15} C_{25} C_{36} $C_{46} \approx 1 - 1.5nF$
- C_{13} $C_{24} \approx 150pF$
- C_{12} C_{23} C_{34} $C_{14} \approx 10fF$
- C_{16} C_{26} C_{56} C_{45} $C_{35} \approx 10pF$

	Plate 1	Plate 2	Plate 3	Plate 4	Plate 5	Plate 6
Plate 1	\\	2.03E-13	1.19E-10	1.44E-13	1.60E-09	9.39E-12
Plate 2	2.03E-13	\\	1.43E-13	1.60E-10	1.60E-09	8.39E-12
Plate 3	1.19E-10	1.43E-13	\\	1.71E-13	2.71E-12	1.37E-09
Plate 4	1.44E-13	1.23E-10	1.71E-13	\\	2.61E-12	1.39E-09
Plate 5	1.60E-09	1.60E-09	2.71E-12	2.61E-12	\\	5.78E-12
Plate 6	9.39E-12	8.39E-12	1.37E-09	1.39E-09	5.78E-12	\\

Table 7.5: Capacitance matrix from simulation

During the measurement procedure, it has been noticed that the length of Litz wire for the measurement purpose on the plates has a substantial effect on the measured values of the capacitance. Hence, the length of the wires is reduced to minimize the effect of wire during the capacitance measurement procedure. This consequence is due to the inductance generated by the cable itself: as the length of the cable increase, this affects the LCR meter to evaluate a capacitive reactance smaller which means evaluating a bigger capacitance. As proof of this consideration, In table 7.6 few results extracted from the LCR meter are compared. While the second measurement has been taken by reducing the length of the cable by 10 cm. The length of the cables should be as small as possible. However, for the measurement purpose tan adequate length is required and cannot be avoided.

Connection 1 and connection 2	Longer cables	Short cables	Unit
P_{123} and P_{456} shorted	3.85	3.71	pF
P_{134} and P_{256} shorted	3.23	3.01	pF
P_{136} and P_{245} shorted	2.31	2.28	pF

Table 7.6: Comparison equation values with different cable connection length

Comparing the two it shows that the capacitance is reduced by reducing the length of the cables. As has already been discussed, 15 equations are required to calculate the individual coupling capacitances. Careful consideration is taken to choose the combinations among the 30 measured combinations.

As a first approach,the full system of equations has been used to find all the capacitances presented in 7.3, However, the six plate capacitance model is no more valid because the stray capacitances of the systems have been introduced that make the system differ from the original 6 plate capacitance.

As a second approach all the parassitic capacitances with a small value have been neglected:

$$C_{12} = C_{23} = C_{34} = C_{14} = C_{16} = C_{26} = C_{56} = C_{45} = C_{35} = 0F \tag{7.1}$$

Those capacitance comes from the minor cross-coupling between the plates and, based on the simulation, as those are extremely small and negligible.

After removing the cross-coupling capacitances the total values of the combinations have been reduced to 6. Hence, only 6 system of equations is required to evaluate the capacitance which has higher values.

$$\begin{gathered} C_{12} + C_{13} + C_{14} + C_{15} + C_{16} \\ C_{13} + C_{23} + C_{34} + C_{35} + C_{36} \\ C_{14} + C_{24} + C_{34} + C_{45} + C_{56} \\ C_{15} + C_{25} + C_{35} + C_{45} + C_{56} \\ C_{12} + C_{23} + C_{24} + C_{26} + C_{15} + C_{35} + C_{45} + C_{56} \\ C_{13} + C_{14} + C_{16} + C_{23} + C_{24} + C_{26} + C_{35} + C_{45} + C_{56} \end{gathered} \tag{7.2}$$

This system of equations is simplified by removing the cross-coupling capacitances. and shown as below.

$$C_{13} + C_{15} \tag{7.3}$$
$$C_{13} + C_{36} \tag{7.4}$$
$$C_{24} + C_{46} \tag{7.5}$$
$$C_{15} + C_{25} \tag{7.6}$$
$$C_{15} + C_{24} \tag{7.7}$$
$$C_{13} + C_{24} \tag{7.8}$$
$$\tag{7.9}$$

The solutions of the equations 7.2 are obtained through the LCR meter, that permits to evaluate the specific capacitance values solving the system 7.10:

$$\begin{array}{cccccc} C_{13} & C_{15} & C_{24} & C_{25} & C_{36} & C_{46} \end{array} \qquad \text{nF}$$

$$\begin{bmatrix} 1 & 1 & 0 & 0 & 0 & 0 \\ 1 & 0 & 0 & 0 & 1 & 0 \\ 0 & 0 & 1 & 0 & 0 & 1 \\ 0 & 1 & 0 & 1 & 0 & 0 \\ 0 & 1 & 1 & 0 & 0 & 0 \\ 1 & 0 & 1 & 0 & 0 & 0 \end{bmatrix} \begin{bmatrix} C_{13} \\ C_{15} \\ C_{24} \\ C_{25} \\ C_{36} \\ C_{46} \end{bmatrix} = \begin{bmatrix} 1.68 \\ 1.02 \\ 0.91 \\ 3.00 \\ 1.71 \\ 0.264 \end{bmatrix} \tag{7.10}$$

Capacitance	Value	Unit
C_{13}	0.117	nF
C_{15}	1.563	nF
C_{24}	0.147	nF
C_{25}	1.437	nF
C_{36}	0.903	nF
C_{46}	0.763	nF

Table 7.7: Final capacitance matrix values

A capacitance matrix 7.5 extracted from a 3D simulation is used as a comparison with the experimental values: the main parameters in this simulation are a nominal plate thickness of 0.127 mm, an insulation thickness of 0.22 mm and a net airgap between the CPT plates of 0.65 mm evaluated on the machine.

A frequency sweep is carried out by varying the frequency from 1kHz to 3MHz for estimating the capacitance variation for one specific combination of capacitances 7.10:

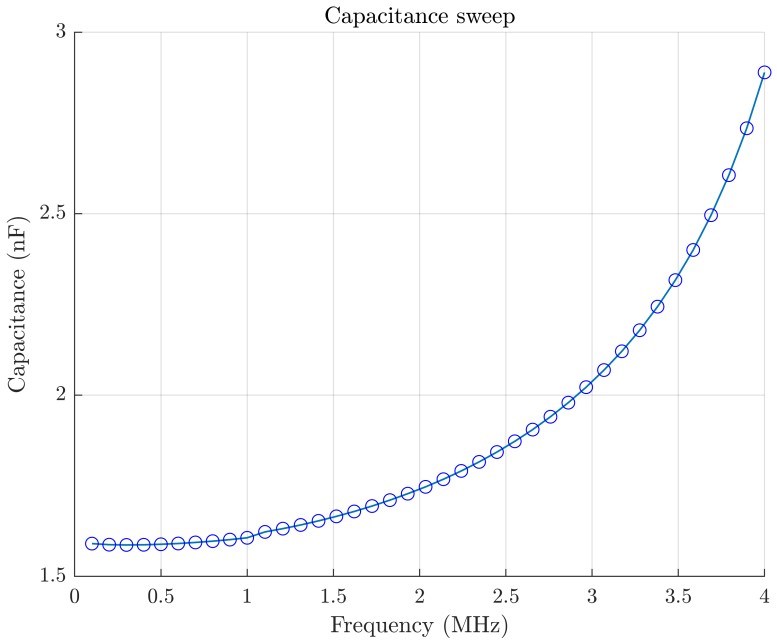

Figure 7.10: Frequency sweep of one capacitance equation

In 7.8 are shown the results at 1kHz frequency:

Capacitance	Experimental values	Simulation values	Unit
C_{13}	117	156	pF
C_{24}	147	156	pF
C_{15}	1.563	1.480	nF
C_{25}	1.437	1.480	nF
C_{36}	0.903	1.260	nF
C_{46}	0.763	1.260	nF

Table 7.8: Comparison between experimental values and simulation values

The capacitance values are in the expected range, the plates facing the rotor are bigger than the capacitances facing the stator as expected, but those are generally smaller compared to the simulation values. This can come for multiple factors:

- Misalignment of the stator plates with the stator core which eventually makes the lower surface area under the influence of the stator core plate for capacitance.

- LCR meter error: as explained in the manual the the accuracy error of the measurememt of the capacitances from LCR meter can vary from a 3% for frequency around 1 kHz up to 6% at 2MHz.
- the different length of the cable connection, as shown previously
- A slight change in the insulation thickness generates a big difference in the capacitances facing the core, as shown in table 7.9.

Insulation Thickness	$C_{15} = C_{25}$	$C_{36} = C_{46}$	Unit
0.18011	1.97	1.70	nF
0.18879	1.85	1.59	nF
0.19152	1.82	1.55	nF
0.19772	1.76	1.51	nF
0.20117	1.71	1.46	nF
0.20766	1.65	1.40	nF
0.21144	1.60	1.37	nF
0.21421	1.59	1.35	nF
0.21908	1.54	1.31	nF
0.22485	1.52	1.29	nF
0.22863	1.47	1.25	nF

Table 7.9: Sweep of capacitance $C_{15} = C_{25}$ and $C_{36} = C_{46}$ varying the insulation thickness

As can be seen, varying the insulation thickness between 0.18 mm to 0.23 mm, the values have a Δ variation of 500 pF.

In conclusion, considering all the sources of errors that needs to be consider in the test, the simulation is a valuable way to estimate the capacitances present in the system. The significant difference between the simulation and the experimental values comes from the imperfection of the prototype and the impossibility to accurately estimate the thickness of the insulation layer with common instruments.

7.4 Power transfer test

In this section is evaluated the amount of power transferred through the plates with an associated LL compensation network. A specific capacitance matrix has been evaluated at the test frequency, evaluated the ESR, and tuned the matching

network's inductors are performed. The test frequency is modified and increased to 2 MHz owing to the limitations of the power amplifier. At 1MHz, as shown in 7.11 and below the power amplifier provides a distorted output voltage waveform due to excessive load mismatch. This can potentially damage the power amplifier.

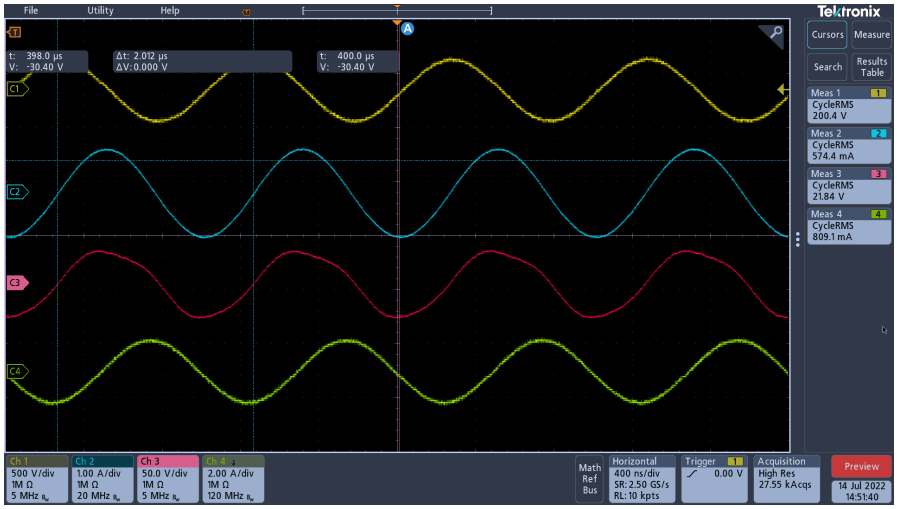

Figure 7.11: Oscilloscope screenshot showing the distorted voltage waveforms

Hence, the frequency of operation of the power amplifier is selected at 2 MHz along with the RF tuner. The tuner provides necessary LC compensation to the input impedance and hence modified the impedance seen by the power amplifier in such a way that improves its voltage waveform. Eventually, the power amplifier can be used at higher power.

Preliminary tests have been performed following the safety standard using a special E field analyzer.

In 7.12 the implemented electric model is presented.

Two inductors L_1 and L_2 are tuned on the primary and secondary side to obtain a resonant circuit condition as explained in 3 and the capacitance matrix is extracted from the model, as explained in the previous section. In 7.12 all the components have a relative resistor associated that represents their Ohmic resistance. Those resistance values are measured through the LCR meter.

Considering the purpose of the CPT, a 25 Ω resistor is chosen to mimic the resistance generated by the DC rotor windings, directly dependent on the field circuit.

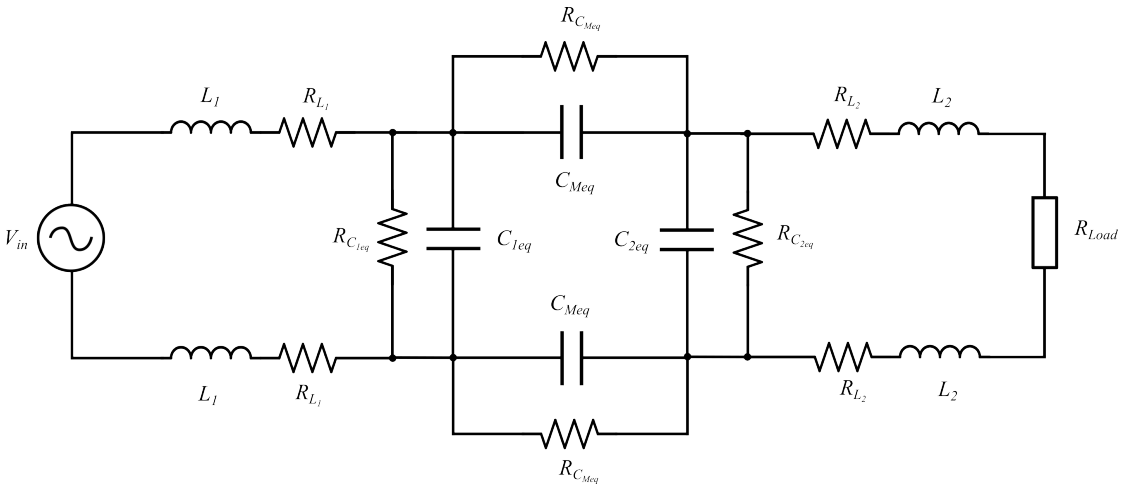

Figure 7.12: Circuit setup

7.4.1 Experimental setup

In 7.13 the full setup is presented:

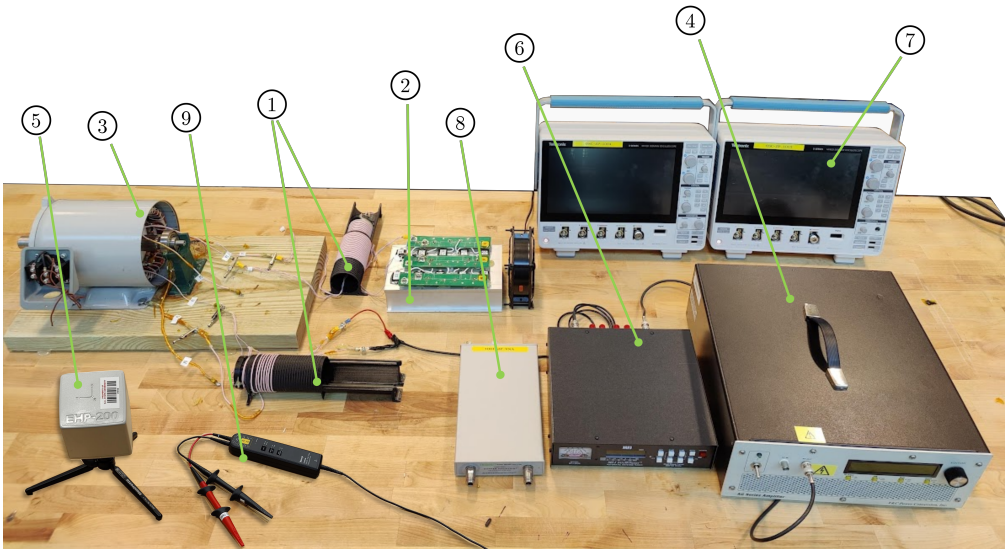

Figure 7.13: Setup for wireless power transfer test

1. Inductors L_1 and L_2;
2. Load resistance R_{load} 25 Ω;
3. Motor Mitsubishi SF XR and CWPT inside it (not visible from the picture);

4. T&C Power Conversion AG 1021 Amplifier: high-frequency amplifier employed to supply the 2MHz current to the circuit;
5. Narda EHP-200A/AC: high-frequency analyzer employed during early stages of analysis to verify that the experimental setup is far from the safe zone for humans;
6. MFJ 993B IntelliTuner™: includes high efficiency switching L-network from 1.8 MHz to 30 MHz to tune the circuit;
7. Oscilloscope's Tektronix MDO34-3-BW-100-MDO;
8. TR1300/1 2-Port 1.3 GHz Analyzer: a Vector Network Analyzer used to estimate precisely the ESR of the inductors;
9. Tektronix THDP0200 high voltage differential probes;

The capacitance is significantly affected while changing the operational frequency of the circuit. As the significant parasitic inductance comes into play due to longer cables. As the main goal of this test is to transfer the power through the proposed coupling structure. The capacitance matrix evaluated at 2 MHz operation frequency is selected to be compared with the simulation-based capacitance. In table 7.10 are shown the values of the capacitances at 2 MHz frequency. and consequently,

Capacitance	Values	Unit
C_{13}	132	pF
C_{24}	172	pF
C_{36}	1.418	nF
C_{46}	1.376	nF
C_{15}	668	nF
C_{25}	725	nF

Table 7.10: Main capacitance values

the equivalent capacitances of the π model shown in 7.12 are:

7.4.2 Tuning procedure of the matching network's inductors

An estimation of the needed inductors can be done using simple circuit analysis. The procedure is based on a first first tuning of the load side and consequently, the

Capacitance	Values	Unit
C_{1eq}	437	pF
C_{2eq}	838	pF
C_{Meq}	152.6	pF

Table 7.11: π model capacitance values

tuning of the primary side with the secondary been tuned.

The value of the inductor L_2 and L_1 is:

$$L_2 = \frac{1}{\omega^2 C_{2eq}} \tag{7.11}$$

$$L_1 = \frac{1}{\omega^2 (C_{1eq} - C_{Meq} + \frac{C_{Meq}(C_{2eq} - C_{Meq})}{C_{2eq}})} \tag{7.12}$$

To tune the power transfer circuit, the inductors at the primary and secondary sides of the power transfer need to be varied such that the total reactance in the system is negligible. For this purpose, the inductor at the secondary side is first tuned by varying the inductance while shorting the primary side capacitive plates. The variation of the secondary inductor is monitored through LCR meter.

The secondary side circuit will be termed as tuned when LCR meter shows negligible capacitive or inductive reactance. For the primary side tuning of the shorted cable at the primary side, plates are removed and the primary inductor is connected to the sending plates. The LCR meter is connected to the input side of the Power Transfer circuit. The primary side is tuned by varying the primary inductor such that the LCR meter shows negligible capacitive or inductive reactance. The tuning has been performed fixing all the cables on the table properly and having in position all the probes needed for the power test as those can affect the general inductance of the system. In table 7.12 are presented the values compared to the ones evaluated through simulation.

	Experimental Inductance	Simulation Inductance	Unit
L_1	14.50	12.48	μH
L_2	7.85	6.92	μH

Table 7.12: Comparison between simulated and measured inductance values

7.4.3 Input resistance verification

After the tuning of the inductors is performed, the effective resistance of seen by the power amplifier at the input side of the circuit is measured by the LCR meter. The presence of a CWPT and a matching network, as explained in 3, change the value of the reflected load resistance on the input side because it acts like a transformer. By connecting the LCR meter to the primary side, the resonance point and the resistance seen by the power amplifier can be checked. As it's evident from 7.15 the resonance peak is at 2 MHz, and the evaluated resistance is 10.4 Ω 7.14, close to the simulated value of 11.2 Ω.

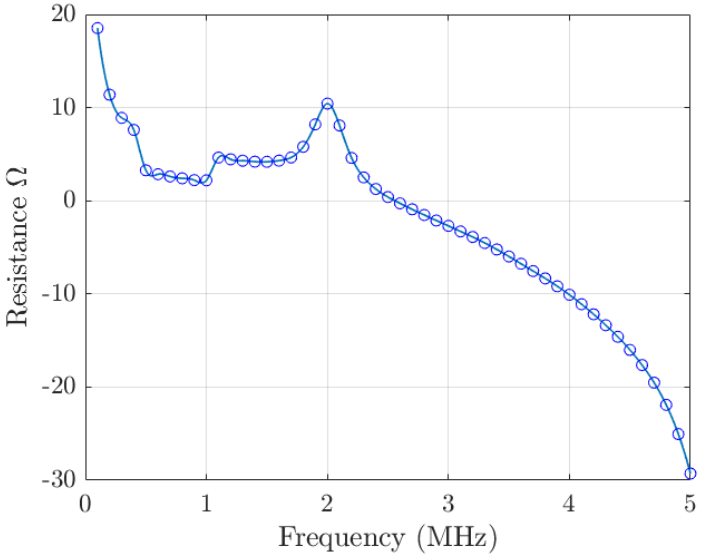

Figure 7.14: Resistance sweep value respect to frequency

7.4.4 Test results

The power test is performed by increasing the power till the nominal value. Table 7.13 contains principal values to estimate the efficiency of the power transfer and the voltages of interest in the system. Two oscilloscopes have been used to have track of multiple voltages together and evaluate them on the same experimental setup. Figure 7.16 shows the power flow from the input to the output side in the form of voltage and current at 65W of power transfer. It is noticeable that at higher power rating the sin wave of the input voltage starts to be distorted. Beyond this power transfer, the system was not able to transfer power anymore. As the

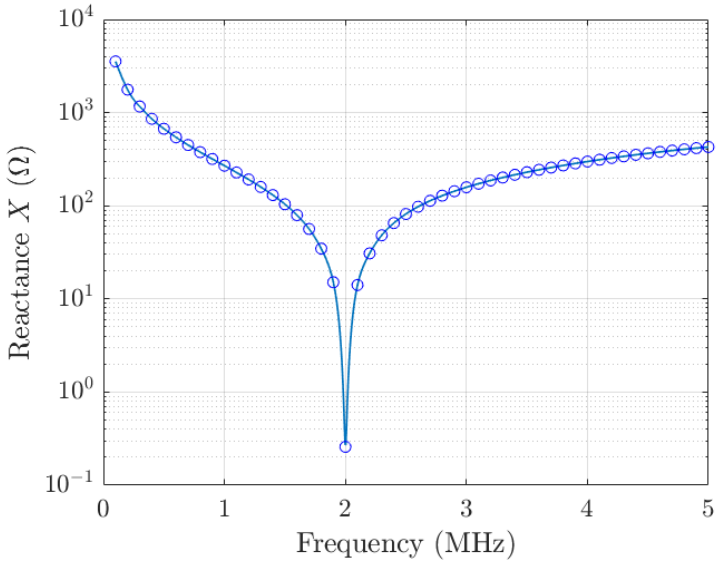

Figure 7.15: Reactance sweep respect to frequency

I_{in}	V_{in}	I_{load}	P_{in}	P_{out}	η	V_{12}	V_{56}	V_{13}
1.112	13.1	0.816	12.86	10.00	0.78	190	12.24	94.32
1.55	18.24	1.147	24.98	19.76	0.79	266.3	16.22	131.8
1.906	22.18	1.406	37.78	29.69	0.78	327.9	19.45	161.7
2.194	25.5	1.621	50.06	39.47	0.79	376.7	22.45	185.9
2.464	28.87	1.832	63.14	50.41	0.80	429	23.75	209.9
2.752	32.55	2.065	78.76	64.05	0.81	480.8	26.71	247.5

Table 7.13: Evaluated points capacitive power transfer test

Kapton tape is responsible to glue the rotor plates and hold them to the rotor sleeve. One of the edges of the rotor plate came off and physically touch the stator plates, as shown in 7.17. In figure 7.18 the value of the efficiency is compared to the simulated value.

The simulated value of efficiency is practically constant because as in a resonant condition the circuit is purely resistive so, as the input power increase the power output increase consequently.

The experimental efficiency shows a slight increment over the time due to a resistive effect that remains constant and does not depends on the power transmitted.

The significant difference is probably related to a wrong estimation in the resistance of the capacitive plates evaluated through the LCR Meter. As the LCR

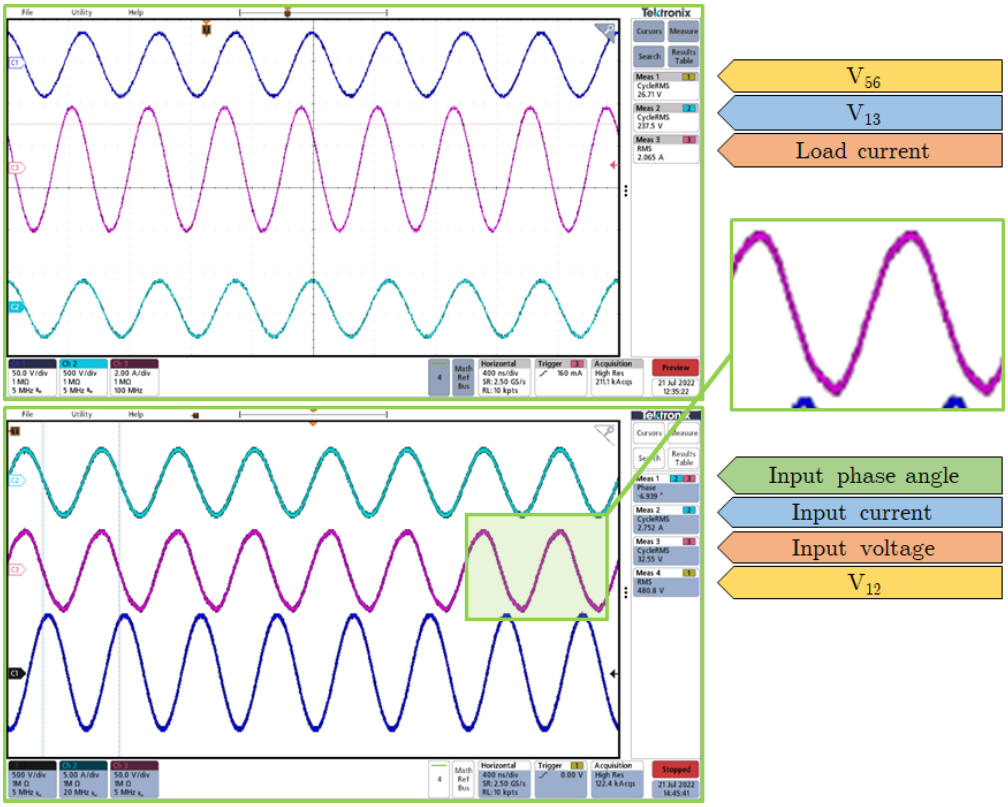

Figure 7.16: Oscilloscpe screenshot showing the distorted voltage at 65 W

meter evaluates the reactance, in a nonresonant circuit the predominant value that is estimated is the imaginary component of the reactance coming from the capacitive or inductive components and consequently, a significant error over the resistance component is present.

A precise way to estimate the resistance of inductors and capacitors is later explained and implemented to evaluate the ESR of the inductors.

In figure 7.19 are shown the cross-coupling voltage between sending side plates and the voltage across the plates directly interested in the power transfer. As can be noticed, the trend over time is essentially linear.

Measurement of the voltage between the rotor and stator core is essential. As ideally there should be no voltage between the rotor and stator core otherwise in practical machine there is a potential hazard of rotor bearing currents would could potentially degrades the bearings. Experiment, 7.20, shows that the inclusion of the proposed design model does not induce significant voltage difference between the rotor and stator core. Moreover the rotor and stator core acts like shielding

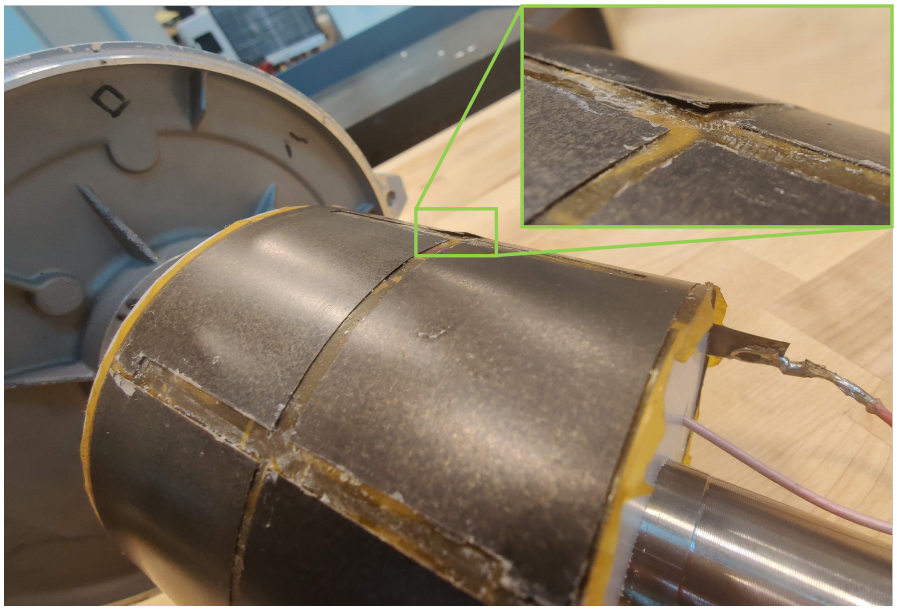

Figure 7.17: Rotor strips damage

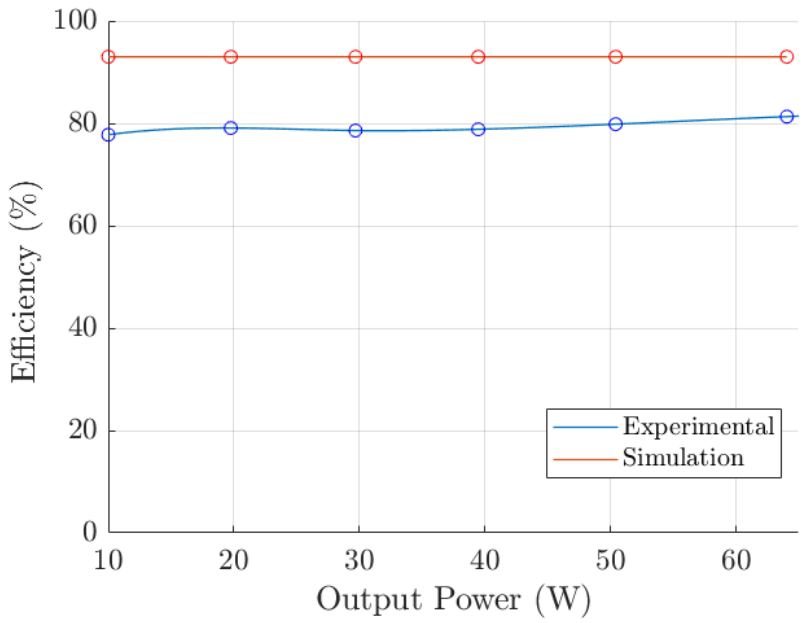

Figure 7.18: Efficiency comparison between simulation and experiment

plates to contain the electric field and minimize the exposure of Electric field in the environment and hence, can be beneficial for safety purposes.

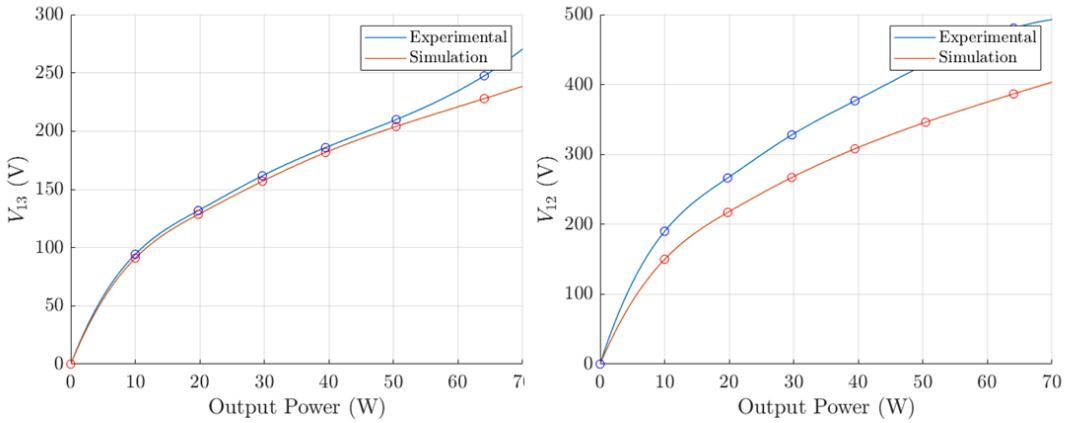

Figure 7.19: Voltages between plates 12 and 34: comparison between simulation and experiment

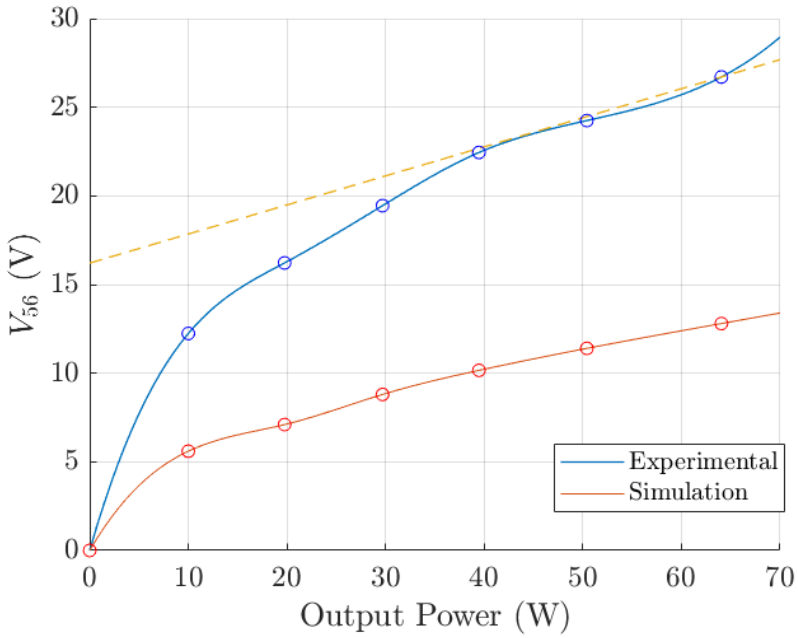

Figure 7.20: Voltage between plates 56: comparison between simulation and experiment

7.4.5 Electric field analyzer considerations

Few measurements have been taken with the Narda E field Analyzer putting the instrument in front of the motor as shown in 7.21.

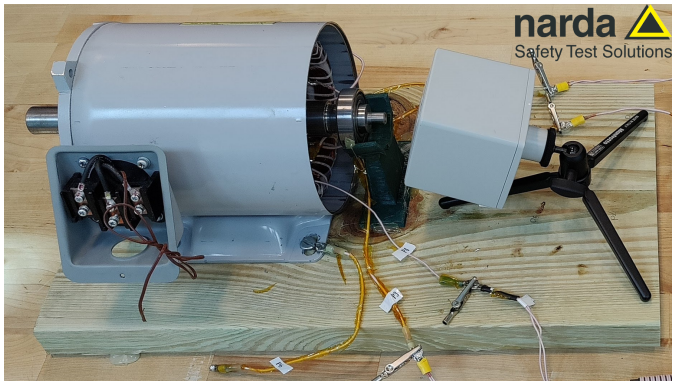

Figure 7.21: Narda location in the setup

For malfunctioning instrument problems and lack of time only a few points have been taken. In 7.23 is evident a linear increase in the magnetic field after a certain amount of power transmitted. This behavior is due to some fringing effect inside the motor itself. As soon as the power transmitted increases, the external field shown in 7.22 depends only on the external plates 5 and 6. As it's noticeable from

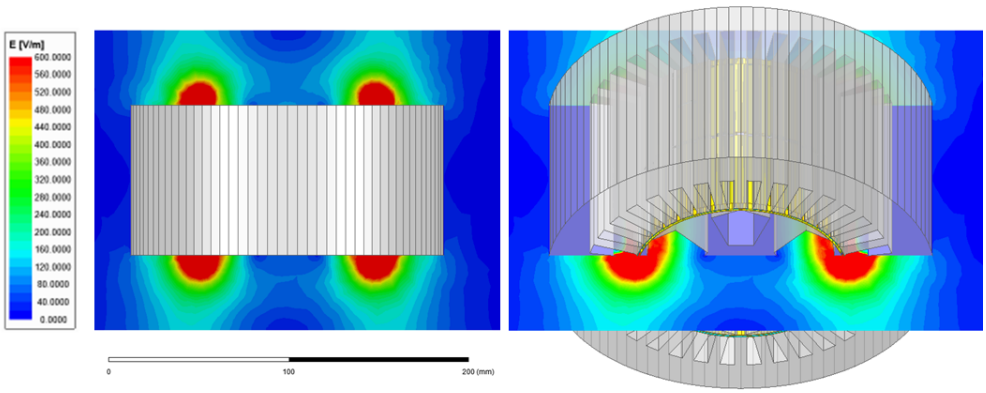

Figure 7.22: 3D plot of the E-field with a 65 W of power output

7.20 the voltage across those two plates it's linear with the power so, as the E field is directly proportional to the voltage, it is also linear with the increasing power.

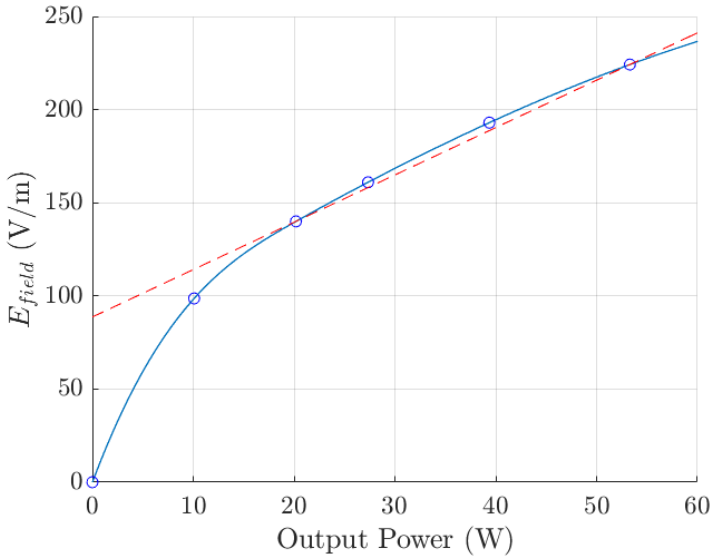

Figure 7.23: E field over the power

In 7.24 is shown the value of the E field around when the output power is ≈ 40 W. The red line represents the human safety limit specified by IEEE C95.1-2005 standard [28]. All the test has been performed while remaining in a safety region, far from the tested prototype.

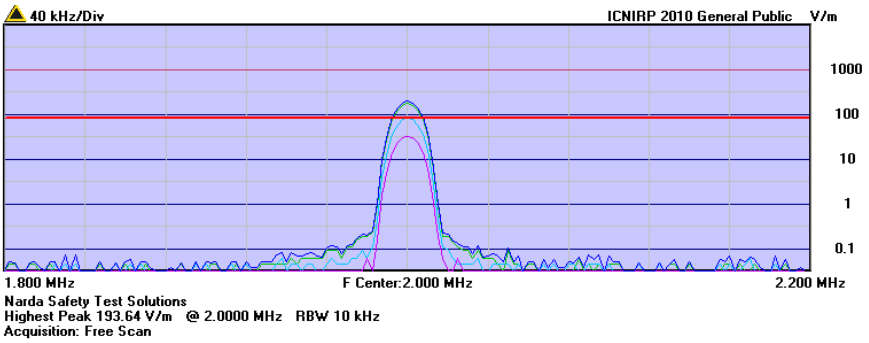

Figure 7.24: Narda screenshot at 40 W power trasmitted

7.4.6 Evaluation of the inductor ESR

The estimation of the resistance of inductor and capacitor can be difficult in common configuration: As the reactance component is in general very high compared to the resistive one, this one is in general affected by huge error. To avoid this problem, a

Vector Network Analyzer VNA shown in 7.13 can be used to estimate it precisely using the parallel resonance method described in [29].

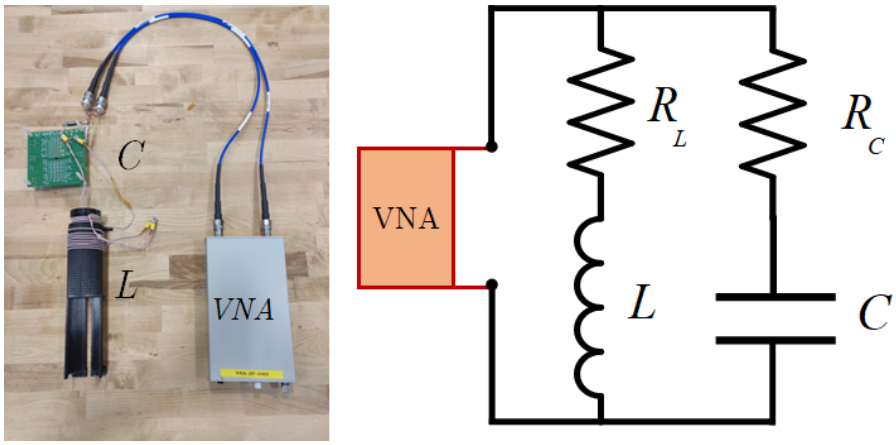

Figure 7.25: ISR inductor estimation setup

The procedure is based on few steps: first is evaluated the inductance of the specific inductor and consequently the needed capacitor to compensate its reactance value and put the circuit in resonant conditions. At this point, the VNA is used to detect the exact resonance frequency and to evaluate the total quality factor Q_T of the circuit. In 7.25 is shown the setup that will be used.

A capacitor with known quality factor Q_C is used to extract the quality factor only of the interested inductor. Q_L is evaluated through the formula 7.13:

$$Q_L = \frac{Q_C Q_T}{Q_C - Q_T} \tag{7.13}$$

in table 7.14 are resumed the principal values:

	Inductance (μH)	Resonant capacitance (pF)	Q_T	Q_C	Q_L	Resistance (Ω)
L_1	8.85	716.27	152.37	1256.50	173.39	0.64
L_2	14.7	431.22	614.37	2087.08	870.66	0.21

Table 7.14: Main values and results from ISR estimation

The inductor L_1 has a very small quality factor that means having an extremely lossy component directly affecting the efficiency of the capacitive power transfer.

Chapter 8

Optimization

After a few considerations, analysis and a first prototype, the research of an optimized design is needed. This chapter proposes an algorithm based on a Bayesian strategy to find the optimum design given few parameters. A preliminary description of the loop case is described. Few considerations to reduce the overall time consumption are made. The analysis is performed through a code that connects MATLAB and ANSYS MAXWELL.

8.1 Loop case description

The optimization loop is composed by multiple FEA simulations and different MATLAB codes combined together. The codes define define the connection between the optimization algorithm and the ANSYS simulations, presented in appendix A, and the evaluation of the losses coming from an LCL compensation network, written by another team member and presented in appendix C. For the first iteration, only two parameters will be considered, the insulation thickness and the plate thickness. The principle of the optimization loop is based on the minimization of a combination of multiple objective functions. The optimization functions that are considered are the differential efficiency, the normalized Torque introduced in Chapter 6 and the torque ripple, evaluated as:

$$T_{ripple} = \frac{Torque_{max} - Torque_{min}}{Torque_{mean}} \tag{8.1}$$

The three functions need to be normalized first and then combined together into a weighted sum. The obtained single objective function is minimized through a

global optimization algorithm to find the optimum design. At an early stage, there are not much information on how the objective function will behave, as much data comes into the analysis, a random research algorithm is used to see if the function converges or not.

To evaluate the mentioned objective functions, multiple Ansys simulations need to be integrated together. In figure 8.1 is shown the complete optimization loop and the related code is shown in appendix A: The first simulation that should run

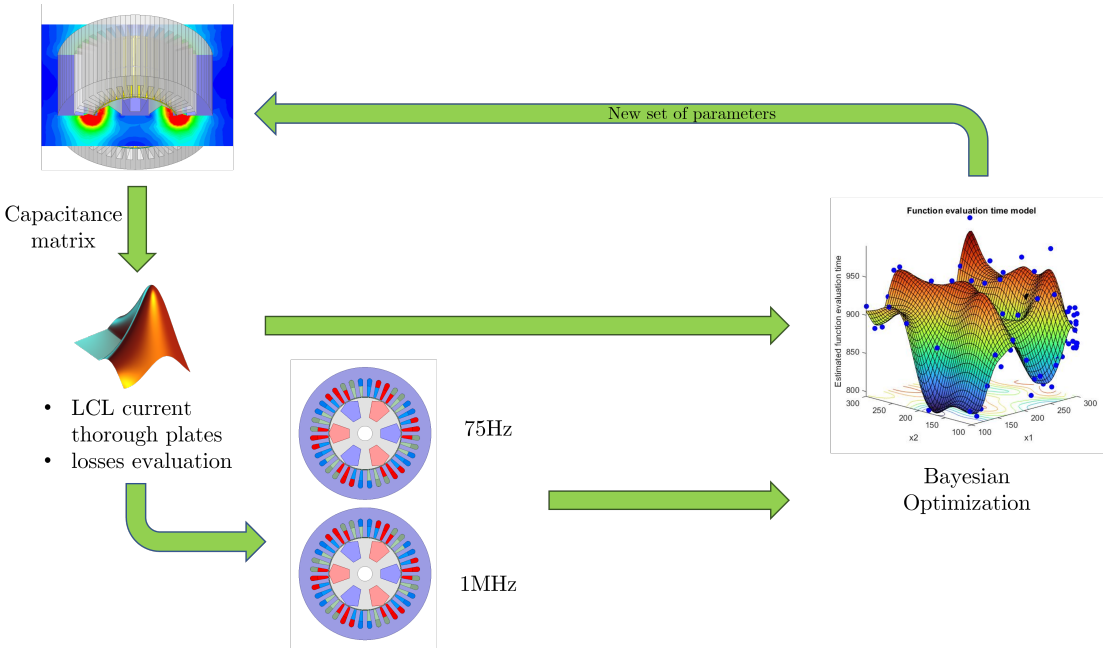

Figure 8.1: Optimization loop scheme

is the 3D model electrostatic simulation needed to extract the capacitance matrix of the model. After that, the matrix is provided to a Matlab code that evaluates, for specific output power, the current flowing in the circuit and the losses of the matching network. After that, two more simulations are needed. A first simulation evaluates the losses coming from the machine field winding at 75 Hz frequency and another one where the 2 Mhz current evaluated from the Matlab code is provided to the plates.

The implementation of those three simulations together represent an enormous cost of time and resources, so few consideration have been made in order to speed up the evaluation and reduce the time consumption. The principal loss of time and instability of the optimization loop comes from the 3d simulation that takes more than 30 minutes. Even after a significant simplification of the model from a full

representative model to an essential polygonal one, as shown in figure 8.2, the time needed for one full loop was still too high. The solution was to create different look-up tables, described in the next section.

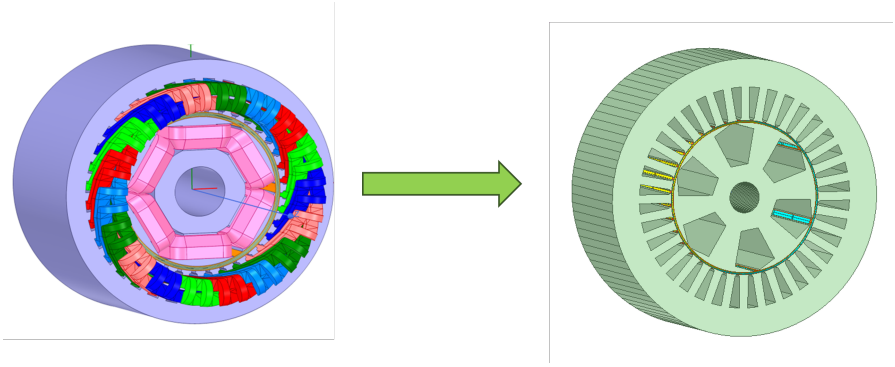

Figure 8.2: Comparison between the complex model and new optimized polygon model

8.2 Matrix lookup tables

A good way to save the evaluation time of the 3D simulation is to create specific look-up tables for a discrete set of parameters, generate the interpolated curves and use them in the optimization algorithm, drastically reducing the evaluation time.

To achieve this goal, 50 different sets of parameters have been evaluated in the range of interest. The capacitance matrix of those points has been extracted, and for each of them, a specific fitting curve has been evaluated. To generate the desired curve, the *curve fitting* toolbox is used. A simple code with few specifications regarding the type of interpolation and the robustness of the fitting is shown:

```
ft = fittype( 'loess' );
opts = fitoptions( 'Method', 'LowessFit' );
opts.Normalize = 'on';
opts.Robust = 'Bisquare';
surffit= fit([NUM(:,1),NUM(:,2)],NUM(:,j),ft, 'Normalize', 'on'...
    );
```

After that, using another set of points the quality of the interpolation is verified, as shown in figure 8.3:

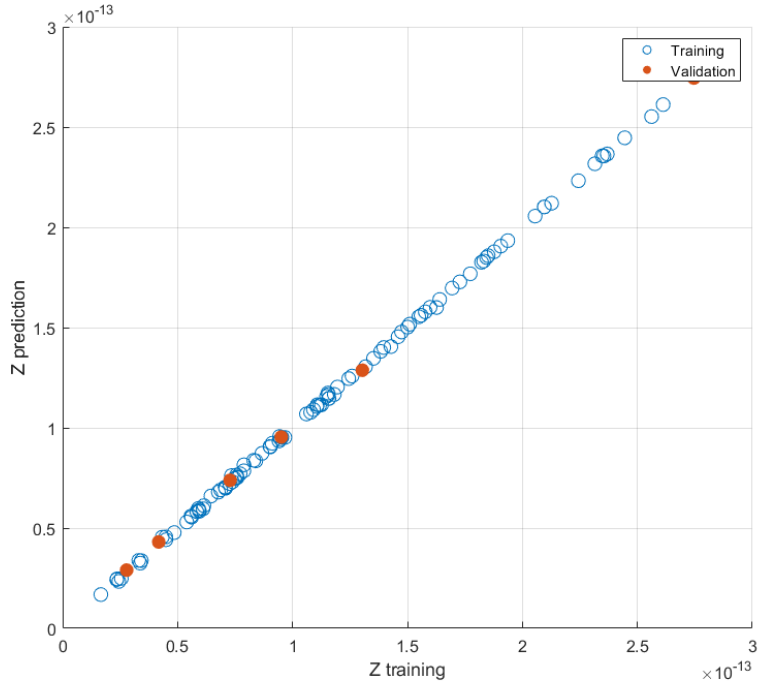

Figure 8.3: Normalized training points (blue) and predicted points (orange)

At the end of the analysis, a set of fitted curves is ready to be directly used and inserted into the optimization loop, Avoiding the use of the 3D simulation.

8.3 Bayesian optimization algorithm

Instead of randomly sampling different points in the interested parameters space, a Bayesian Optimization algorithm is implemented. This code makes use of the Bayes theorem to find the solution of a general global optimization problem [30]. The basic principle is based on an initial random sampling around a defined point, and from that, using a probabilistic model analyzing other points to find the minimum of the objective function. The number of iterations needed is strongly dependent on the number of parameters evaluated. Figure 8.4 shows the different time consumption for different iterations. As can be noticed, they are variable and depend on the complexity of the geometry: as the geometry changes every iteration, the mesh of the components changes accordingly, increasing or decreasing the overall complexity of the model.

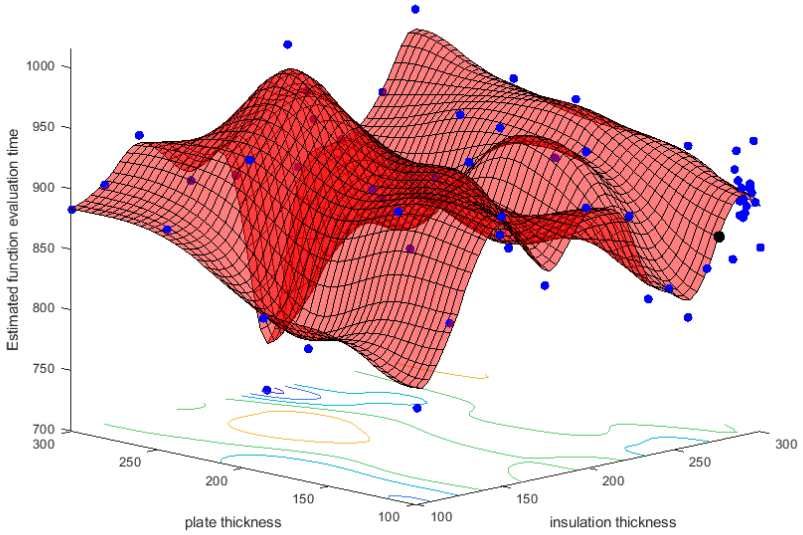

Figure 8.4: Fitting curve showing the different evaluation times for all the evaluated points

As in this first iteration only two parameters have been analyzed, 60 iterations are enough to evaluate an optimum point, as shown in figure 8.5. After those iterations, there is no more significant improvement in the reduction of the objective function. Figure 8.6 shows at the end the shape of the objective function curve: as can be noticed, in this case, an optimum global point has been founded, but it's not always true.

A closed look at the evaluated points over a Pareto front, like the one present in chapter 6, for a specific set of weights lets the reader understand the iteration process of this algorithm: at first, it analyzes different points in the space, and when it is close to the solution it analyses more points in that region. Figure 8.7 shows the different evaluated points for two different sets of weights.

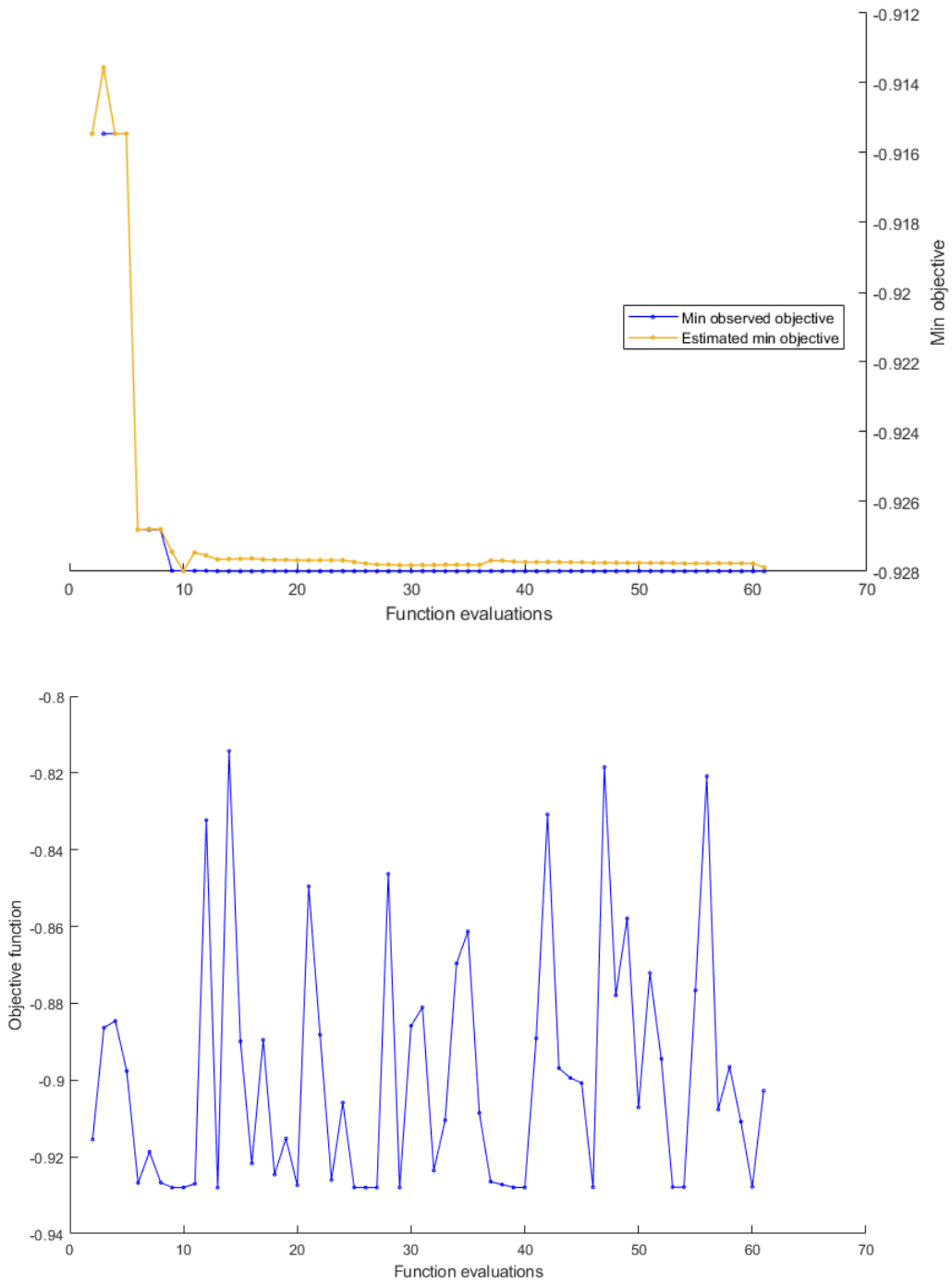

Figure 8.5: Value of the objective function with respect to the iteration number and the estimated minimum objective function

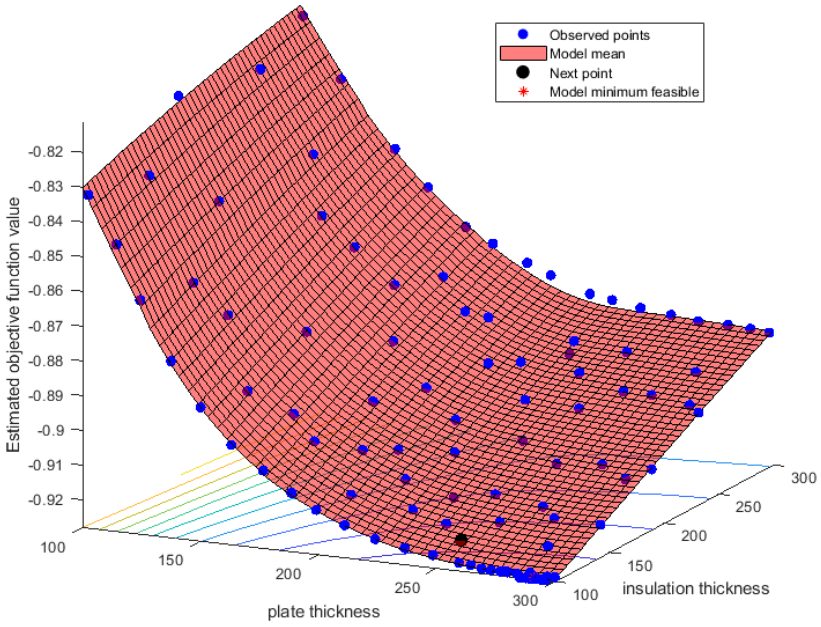

Figure 8.6: Optimization function curve after 80 iteration configurations

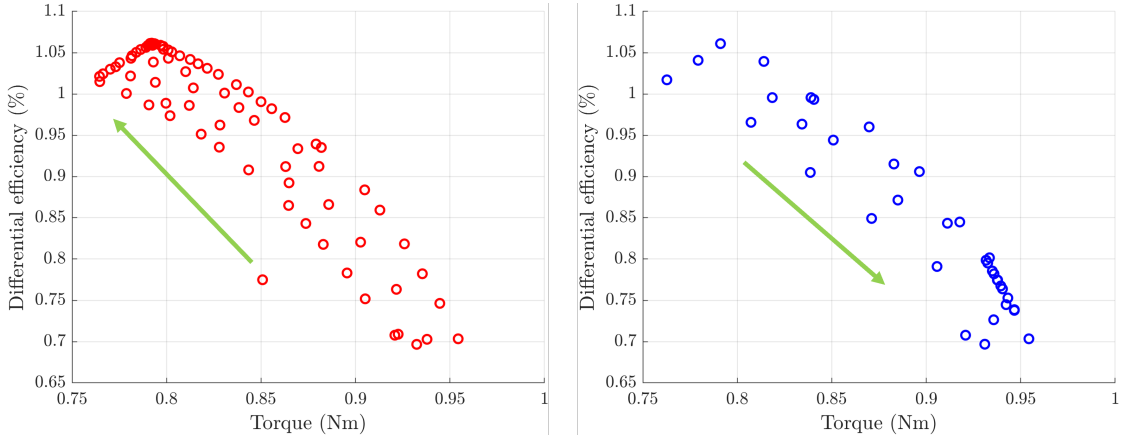

Figure 8.7: (Left): Pareto front with 0.2 weight on the torque, 0.7 on the differential efficiency and 0.1 on the torque ripple; (Right): Pareto front with 0.7 weight on the Torque, 0.2 on the differential efficiency and 0.1 on the Torque ripple

Chapter 9

Conclusion

This last chapter concludes the thesis dissertation, summarizing the achieved results and the future works related to the project.

9.1 Achieved results

The objective of this project was to investigate, simulate and prototype a new configuration of capacitive wireless power transfer system for a wound field synchronous machine. Many challenges raised up related to find a way to simulate a completely new system taking in consideration all the side effects of inserting electrically excited metal plates in the air gap of a motor. A first set of simulations was run in order to verify the feasibility of the system, regarding the voltages across the plates and the transmitted power. Later, a first prototype to test the capacitive wireless power transfer has been developed: the results regarding the capacitance matrix and the expected amount of energy transferred has been confirmed through the simulation results.

Furthermore, a preliminary implementation of an optimization loop has been studied for the second prototype generation. A complete algorithm able to connect MATLAB and ANSYS, performing multiple simulations at the same time and finding the global optimum solution through a Bayesian optimization loop has been written and run.

9.2 Future works

The improvements that can be performed in the future are related to achieve a better efficiency of the CPT system and to see the full machine working:

- Insert in the optimization loop more variables that are involved in the geomoetry of the plates (width, length, number of strips);
- Test different solutions to hold in position the plates istead of using Kapton tape;
- Test the full machine, including the integration of an inverter and a rectifier.

Appendix A

Objective function evaluation

This function represents one iteration of the loop case study. Through this, the ANSYS simulations are called, the data analyzed and evaluated in the objective function that needs to be minimized.

```
function value = evalObjectiveFunctions_BayesianNEW(vars)
%first check the number of time step that have been used in the...
    simulation
    data(1)=vars.x1
    data(2)=vars.x2
%set the location of the files and scripts
    project_path="C:\Users\ssavio\Desktop\Optimization 3.0";
%parfor function permits to evaluate two different functions at...
    the same
%time. This permits to run in parallel two different simulation...
    on ANSYS
    parfor ii = 1:2
        if ii == 1
        Run_Maxwell_75Hz(data,project_path);
        else
        %a small pause between the two functions is necessary ...
    in order to
        %avoid overlapping with the ANSYS connection
        pause((ii-1)*10);
        Run_Maxwell_capacitance_matrix(data,project_path);
```

```
17          end
18      end
19      time_step_75=102;
20      number_design_75=1;
21
22 %import into the workspace the evaluated losses at 75 Hz and  ...
     the Torque
23      [Ohmic_Loss_rotor_strip75] =Losses_import_for_optimization(...
     time_step_75, number_design_75,"75...
     HzOhmic_Loss_rotor_strip.csv",0);
24      [Ohmic_Loss_stator_strip75]=Losses_import_for_optimization(...
     time_step_75, number_design_75,"75...
     HzOhmic_Loss_stator_strip.csv",0);
25      [Rotor_losses_core75]=Losses_import_for_optimization(...
     time_step_75, number_design_75,"75HzRotor_losses_Core.csv...
     ",0);
26      [Stator_losses_core75]=Losses_import_for_optimization(...
     time_step_75, number_design_75,"75HzStator_losses_Core.csv...
     ",0);
27      [Torque]=Losses_import_for_optimization(time_step_75, ...
     number_design_75,"75HzTorque.csv",0);
28
29 %calculate the mean value of the losses at 75 Hz, starting from...
      a specific time step
30 %(in order to avoid the initial transient)
31      start_time_step=68;
32      Mean_loss75=6*mean(Ohmic_Loss_rotor_strip75([...
     start_time_step:end],2))+...
33              36*mean(Ohmic_Loss_stator_strip75([start_time_step:...
     end],2))+mean(Rotor_losses_core75([start_time_step:end],2))...
     ...
34              +mean(Stator_losses_core75([start_time_step:end],2)...
     );
35
36
37 %evaluate the losses coming from the matching network
38      matrix_table=import_matrix_table_NEW
39      [Plate_current,P_losses,v_p12_rms_minimum_Q,...
     v_p32_rms_minimum_Q...
40          ,v_p42_rms_minimum_Q,Efficiency_system,Cf1,Cf2,Lf1,Lf2,...
     L1,L2,Q_var,esrL1...
41          ,esrL2,esrLf1,esrLf2,esrCf1,esrCf2,c1_eqpi,c2_eqpi,...
     cm_eq,Source_v,Load_r,Losses_rectifier_output]=...
     LCL_losses_rect(matrix_table,1);
42
```

```
%Losses high frequency current LCL compensation
    data(3)=Plate_current;

%evaluating the losses coming from the high frequency current
    Run_Maxwell_1MHz(data,project_path);
    time_step_1MHz=76;
    number_design_1MHz=1;

%importing high frequency losses
    [Ohmic_Loss_rotor_strip1MHz] =...
    Losses_import_for_optimization(time_step_1MHz, ...
    number_design_1MHz,"1MHzOhmic_Loss_rotor_strip.csv",0);
    [Ohmic_Loss_stator_strip1MHz]=...
    Losses_import_for_optimization(time_step_1MHz, ...
    number_design_1MHz,"1MHzOhmic_Loss_stator_strip.csv",0);
    [Rotor_losses_core1MHz]=Losses_import_for_optimization(...
    time_step_1MHz, number_design_1MHz,"1...
    MHzRotor_losses_Core.csv",0);
    [Stator_losses_core1MHz]=Losses_import_for_optimization(...
    time_step_1MHz, number_design_1MHz,"1...
    MHzStator_losses_Core.csv",0);
    start_time_step=20;

%calculate the mean value of the losses, starting from a ...
    specific time step
    Mean_loss1MHz=6*mean(Ohmic_Loss_rotor_strip1MHz([...
    start_time_step:end]))...
            +36*mean(Ohmic_Loss_stator_strip1MHz([...
    start_time_step:end]))...
             +mean(Rotor_losses_core1MHz([start_time_step:end...
    ]))...
             +mean(Stator_losses_core1MHz([start_time_step:end...
    ]));

%Total losses sum and evaluation of the mean torque
    Total_loss=P_losses+Mean_loss75+Mean_loss1MHz+...
    Losses_rectifier_output;
    Mean_torque=mean(Torque);

%Comparison Machine values
    P_out=70; %W
%to evaluate the loss function we remove the losses coming from...
     a machine
%with 0.8mm airgap  without any plates inside, but considering ...
    the losses
```

```
72 %coming from the brushes
73     loss_brushes=4;
74     machine_core_losses=17;
75     losses_machine_comparison=machine_core_losses+loss_brushes;
76     Torque_compare=11;
77     loss_eval=Total_loss-losses_machine_comparison;
78
79 %differential power loss normalized by output power
80     differential_eff=P_out./(P_out+loss_eval);
81     Torque_normalized=Mean_torque/Torque_compare;
82     Ripple=(max(Torque)-min(Torque))/Mean_torque
83
84 %weigths of the evaluated functions
85     w1=0.5
86     w2=0.5
87     w3=0.2
88
89 %objective function to be minimized
90     value = -(w1*differential_eff + w2*Torque_normalized)+0.2*...
       Ripple);
91
92 %% Save all results into an external .csv file (name .csv file ...
       before every optimization here)
93     output_matrix = [Mean_loss75 Mean_loss1MHz Mean_torque ...
       Ripple differential_eff P_losses Losses_rectifier_output]
94
95     try
96         writematrix(output_matrix,'save_file.csv','WriteMode','...
       append')
97     catch EM1
98         disp(EM1)
99     end
100 end
```

Appendix B

Import losses function and interface code between MATLAB and ANSYS

This function sends instructions to the ANSYS simulations and saves the analyzed data into .csv files. The code has been written with the fundamental help and knowledge of Muhammad Abdelraziq.

```
function [] = Run_Maxwell(data,project_path)
iMaxwell = actxserver('Ansoft.ElectronicsDesktop');

%this first section create the connection between MATLAB and ...
    ANSYS looking
%for a specific project into a specific folder
    try
        oDesktop = iMaxwell.GetAppDesktop();
        oDesktop.RestoreWindow;
        oProject = oDesktop.SetActiveProject("75Hz 3");
        oDesign = oProject.SetActiveDesign("75...
    HzDesign_nominal_complete_losses_update_winding");

%the optimetric setup is cleaned and ready to accept new ...
    parameters to
%analize
        oModule = oDesign.GetModule('Optimetrics');
```

```
15          try
16              invoke(oModule, 'DeleteSetups', {'ParametricSetup1...
    '});
17          catch
18              warning('There was no Optimetrics settings set up!'...
    );
19          end
20
21 %here the specific variable for the iteration are imported and ...
    saved into
22 %the workspace
23          invoke(oModule, 'InsertSetup', 'OptiParametric', {'...
    NAME:ParametricSetup1', 'IsEnabled:=', ...
24              true, {'NAME:ProdOptiSetupDataV2', 'SaveFields:=', ...
    true, 'CopyMesh:=', false, 'SolveWithCopiedMeshOnly:=', ...
25              true}, {'NAME:StartingPoint'}, 'Sim. Setups:=', {'...
    Setup1'}, {'NAME:Sweeps', {'NAME:SweepDefinition', 'Variable...
    :=', ...
26              'insulator_tickness', 'Data:=', strcat(num2str(data...
    (1,1)),'um'), 'OffsetF1:=', false, 'Synchronize:=', 0}, {'...
    NAME:SweepDefinition', 'Variable:=', ...
27              'plates_tickness', 'Data:=', strcat(num2str(data(1,2)...
    ),'um'), 'OffsetF1:=', false, 'Synchronize:=', 0}}});
28          invoke(oProject,'Save')
29
30 %the code asks ANSYS to read the optimetrics and to solve the ...
    setup
31          invoke(oModule, 'SolveSetup', 'ParametricSetup1');
32          oModule = oDesign.GetModule('ReportSetup');
33
34 %at the end of the analysis, few excel files are created with ...
    all the
35 %desired datas saved on them
36          invoke(oModule,'UpdateReports', {'75HzTorque'})
37          invoke(oModule,'UpdateReports', {'75HzStator_strip'})
38          invoke(oModule,'UpdateReports', {'75HzRotor_strip'})
39          invoke(oModule,'UpdateReports', {'75...
    HzStator_losses_Core'})
40          invoke(oModule,'UpdateReports', {'75HzRotor_losses_Core...
    '})
41
42          invoke(oModule, 'ExportToFile', '75HzTorque', ...
43            strcat(project_path,'/75HzTorque.csv'));
44
```

```
45          invoke(oModule, 'ExportToFile', '75HzStator_strip', ...
    ...
46              strcat(project_path,'/75HzOhmic_Loss_stator_strip.csv...
    '));
47
48          invoke(oModule, 'ExportToFile', '75HzRotor_strip', ...
    ...
49              strcat(project_path,'/75HzOhmic_Loss_rotor_strip.csv'...
    ));
50
51
52          invoke(oModule, 'ExportToFile', '75HzRotor_losses_Core...
    ', ...
53              strcat(project_path,'/75HzRotor_losses_Core.csv'));
54
55          invoke(oModule, 'ExportToFile', '75...
    HzStator_losses_Core', ...
56              strcat(project_path,'/75HzStator_losses_Core.csv'));
57
58        invoke(oDesign, 'DeleteFullVariation', 'All', true);
59        disp('Deleted previous variation!')
60
61      catch EM
62          disp(EM)
63          delete(iMaxwell);
64      end
65
66  end
```

This function is used to extract the data from the files generated by the simulations, check the data unit and save them into usable variables.

```
1  function [Losses_table]=losses_converter_no_plates_pareto(...
       time_step, number_design,file_name,figure_number)
2
3  trigger=0;
4  [NUM,TXT,RAW] = xlsread(file_name);
5
6  for i=2:length(NUM)
7       %time column
8        if contains(TXT(1,1), "[ms]")
9            NUM(i,1) = NUM(i,1)*1e-3;
```

```
10          elseif contains(TXT(1,1), "[us]");
11              NUM(i,1) = NUM(i,1)*1e-6;
12          elseif contains(TXT(1,1), "[ns]");
13              NUM(i,1) = NUM(i,1)*1e-9;
14          elseif contains(TXT(1,1), "[ps]");
15              NUM(i,1) = NUM(i,1)*1e-12;
16          end
17          %Watt column
18          if contains(TXT(1,2),"[mW]")
19              NUM(i,2) = NUM(i,2)*1e-3;
20          elseif contains(TXT(1,2),"[uW]")
21              NUM(i,2) = NUM(i,2)*1e-6;
22          elseif contains(TXT(1,2),"[nW]")
23              NUM(i,2) = NUM(i,2)*1e-9;
24          elseif contains(TXT(1,2),"[pW]")
25              NUM(i,2) = NUM(i,2)*1e-12;
26          end
27          Losses_table=NUM;
28  end
```

Appendix C

LCL matching network losses evaluation code

This code is used to evaluated the losses coming from the LCL matching network and the current flowing in the capacitive strips given a specific capacitance matrix. The code has been written in collaboration with the team member Syed Muhammad Hassan Gillani.

```
function [Plate_current,P_losses,v_p12_rms_minimum_Q,...
    v_p32_rms_minimum_Q...
     ,v_p42_rms_minimum_Q,Efficiency_system,Cf1,Cf2,Lf1,Lf2,L1,...
    L2,Q_var,esrL1...
     ,esrL2,esrLf1,esrLf2,esrCf1,esrCf2,c1_eqpi,c2_eqpi,cm_eq,...
    Source_v,Load_r,Losses_rectifier_output] = LCL_losses_rect(c...
    ,j)

%% Summary of Function
%This function receives two input
%The first input is a 6x6 matrix which represents the ...
    capacitance
%matrix.The second input is the model number that we get ...
    against every
%capacitance matrix.
%The first output is the peak current through L1 Compensation ...
    Element that
%essentially is in series with the Plate. Hence, it is a peak ...
    current for
```

```
12 %the plate. The second output is the total losses in the ...
       compensation
13 %elements.
14 %   The primary steps of the function is tabulated as below:
15 % a) Conversion of 6x6 capacitance matrix into 2 port ...
       equivalent
16 % capacitance matrix.
17 % b) Evaluating the Range of LCL Compensation based on the ...
       power condition
18 % and resonance
19 % c) Evaluating the ESR of every compensation set
20 % d) Evaluating the Input Impedence of all the circuits based ...
       on the unique
21 % compensation sets
22 % e) Evaluating the voltages and currents of all the impedence ...
       stages of
23 % the circuits by going from source to load.
24 % f) Evaluating the voltage and curretns of all teh circuit ...
       components
25 % g) Evaluating the Pin and Pout along with the compensation ...
       losses
26 % h) Evaluating the Reactive Power of the compensation elements...
        along
27 % with the total reactive power
28 % i) Selection of the compensation based on teh minimum ...
       reactive power for
29 % a specific model
30
31 %% Evaluation of 2 Port Equivalent Capacitance Model from given...
        six plate Capacitance Matrix
32 %The document for evaluating this paper is
33 % https://ieeexplore.ieee.org/document/7839952
34 %The equation number is (3)
35 %Calculating the paramentes for C1
36
37 ce1=c(3,5)+c(3,6)+c(4,5)+c(4,6);
38 ca1=c(1,3)+c(1,4);
39 cb1=c(2,3)+c(2,4);
40 cc1=c(1,5)+c(1,6);
41 cd1=c(2,5)+c(2,6);
42
43 % The equation is evaluted from this document
44 % https://ieeexplore.ieee.org/document/7839952
45 % The equation is taken from Table 2 Last Equation
46 ct=ce1*...
```

```
47      (ca1+cb1+cc1+cd1)...
48      +((ca1+cb1)*(cc1+cd1));
49  c01=(((ce1*(ca1+cc1))...
50      *(cb1+cd1))/ct)...
51      +(((ca1*cb1*(cc1+cd1))...
52      +(cc1*cd1*(ca1+cb1)))/ct);
53  ce2=c(1,5)+c(1,6)+c(2,5)+c(2,6);
54  ca2=c(3,5)+c(3,6);
55  cb2=c(4,5)+c(4,6);
56  cc2=c(1,3)+c(2,3);
57  cd2=c(1,4)+c(2,4);
58  c02=(((ce2*...
59      (ca2+cc2))*(cb2+cd2))...
60      /ct)+(((ca2*cb2*...
61      (cc2+cd2))+...
62      (cc2*cd2*(ca2+cb2)))/ct);
63  % The equation is evaluted from this document
64  % https://ieeexplore.ieee.org/document/7839952
65  % The equation is taken from Table 2 Middle Column
66  %Calculating parameters for C2
67  %Calculating Paramenters for C3
68  ca3=c(1,5)+c(2,5);
69  cb3=c(1,6)+c(2,6);
70  cc3=c(3,5)+c(4,5);
71  cd3=c(3,6)+c(4,6);
72  ce3=c(1,3)+c(1,4)+c(2,3)+c(2,4);
73
74  % The equation is evaluted from this document
75  % https://ieeexplore.ieee.org/document/7839952
76  % The equation is taken from Table 2 Last equation
77  c03=(((ce3*(ca3+cc3))*...
78    (cb3+cd3))/ct)+(((ca3*cb3*...
79      (cc3+cd3))+(cc3*cd3*(ca3+cb3)))/ct);
80  c1=c(1,2)+c01;
81  c2=c(3,4)+c02;
82  c3=c(5,6)+c03;
83  %%Calculating CM12 CM13 CM23
84  cm12=((ce1*((c(2,4)*cc1)-(c(1,4)*cd1)))/ct)+(((c(4,5)+c(4,6))*...
        ...
85      (ca1*cd1-cb1*cc1))/ct)+((((c(1,3)*c(2,4))...
86      -(c(1,4)*c(2,3)))*(cc1+cd1+ce1))/ct);
87
88  cm31=((ce3*((c(2,6)*cc3)-(c(2,5)...
89      *cd3)))/ct)+(((c(2,4)+c(2,3))*...
90      (ca3*cd3-cb3*cc3))/ct)+((((...
```

```
91      c(1,5)*c(2,6))-(c(1,6)*c(2,5)))*(cc3+cd3+ce3))/ct);
92 cm13=cm31;
93 cm23=((ce2*((c(4,6)*cc2)-...
94      (c(3,6)*cd2)))/ct)+(((c(1,6)+c(2,6))*...
95      (ca2*cd2-cb2*cc2))/ct)+...
96      ((((c(3,5)*c(4,6))-(c(3,6)*c(4,5)))*(cc2+cd2+ce2))/ct);
97
98 %Calculating the Equivalent 2 Port Model Capacitances of Six ...
      Plate Coupler
99 c1eq=c1-(((cm13)^2)/c3);
100 c2eq=c2-(((cm23)^2)/c3);
101 cmeq=cm12+((cm13*cm23)/c3);
102
103 %For Resonance Purpose the Input and Output Capacitance is ...
      evaluated to
104 %equate with the external compensations.
105 %This equation is taken from the document
106 %https://ieeexplore.ieee.org/abstract/document/7390090
107 %The equation id taken from equation number 10
108 % The primary and secondary side input capacitance
109 Cin_Pri=c1eq-cmeq+cmeq.*((c2eq-cmeq)./c2eq);
110 Cin_Sec=c2eq-cmeq+cmeq.*((c1eq-cmeq)./c1eq);
111 %
112 %The equivalent pi Model of the capacitor plates
113 %This equation is taken from the document
114 %https://ieeexplore.ieee.org/abstract/document/7390090
115 %The equation id taken from figure 4 part b
116 c1eq_pi=c1eq-cmeq;
117 c2eq_pi=c2eq-cmeq;
118 %Evaluating Coupling Coefficient
119 %https://ieeexplore.ieee.org/abstract/document/7390090
120 %The equation id taken from equation number 9
121  kc=cmeq/(sqrt(c1eq*c2eq));
122 %% The Next Section is for evaluation of Inductances and ...
      Capcitance of LCL
123 %Compensation Topology
124
125 %For this we are required to define system output power rating....
       system
126 %Operating frequency, and required voltage gain of the ...
      compensation and
127 %coupler stage.
128 f0=1e6;                                          %Frequency of ...
      operation
```

```
129 w0=2*pi*f0;                                          %Radial ...
      frequency
130 pout_dc=70.66;                                       %Output Power ...
     DC side.
131 r_dc=13.66;                                          %DC Load ...
      Resistance
132 Losses_rectifier=1.41;
133 efficiency_rectifier=pout_dc/(Losses_rectifier+pout_dc);
134 pout=pout_dc/efficiency_rectifier;                   %Output Power ...
      at the AC side load
135 %The input impedence is the AC resitance to the input of the  ...
      the full bridge rectifier
136 rl=r_dc*(8/((pi^2)*efficiency_rectifier));                    ...
            %Calculated from the formula Rin=8*Rl/pi^2 current ...
      driven full bridge rectifier
137 % rl=(pi^2*r_dc)/(8*efficiency_rectifier);       %Load ...
      resistance and the AC side
138 vs_rms=300*(2*sqrt(2)/pi);                         %Full Bridge ...
      Lossless Inverter RMS output
139 vr_rms=(sqrt(pout*rl));                           %Full Bridge ...
      Rectifier Lossless RMS input
140 ir_rms=vr_rms/rl;
141
142 %Sweeping the value of Cf1_LC
143 sweep_factor=1/100;
144 Cf1_LCL_initial=100e-12;                             %Initial value ...
      of the Cf1 for range of different Cf1
145 Cf1_LCL_final=10e-9;                                 %Maximum alue ...
      of Cf1 for range of different Cf1
146 Cf1_LCL=(Cf1_LCL_initial:sweep_factor...              %Variation of ...
      Cf1 capacitance
147      *Cf1_LCL_initial:Cf1_LCL_final);
148
149 %Evaluation of Cf2 based on the power condition
150 %The equation is taken from the document
151 %https://ieeexplore.ieee.org/document/7839952
152 %The equation number of teh document is 13
153 Cf2_LCL=((pout*(1-kc^2)*c1eq*c2eq)./...
154      (2*pi*f0*cmeq*Cf1_LCL*vs_rms*vr_rms));
155
156
157 %Evaluation of Lf1 Lf2 L1 and L2 based on the resonance ...
      condition
158 %The equation is taken from the document
159 %https://ieeexplore.ieee.org/document/7839952
```

```
%The equation number of the document is 15
Lf1_LCL=1./((2*pi*f0)^2*(Cf1_LCL));
Lf2_LCL=1./((2*pi*f0)^2*(Cf2_LCL));
L1_LCL=1./(((2*pi*f0)^2)*Cf1_LCL)...
    +(1/(((2*pi*f0)^2)*Cin_Pri));
L2_LCL=1./(((2*pi*f0)^2)*Cf2_LCL)...
+(1/(((2*pi*f0)^2)*Cin_Sec));
%% Evaluating the ESR of Capacitance and Inductance
%evaluation of capacitance ESR
%Coefficients of the ESR capacitance based on the curve fit if ...
    the
% available capacitors and their ESR
a=34.81;
b=-0.001765;
c=4.085;
d=-4.807e-6;
ESR_Cf1_LCL=1e-3*(a*exp(b*(Cf1_LCL/1e-12))...   %The evaluation...
     of Cf1 ESR based on the equation of Curve fit
    +c*exp(d*(Cf1_LCL/1e-12)));
ESR_Cf2_LCL=1e-3*(a*exp(b*(Cf2_LCL/1e-12))...
    +c*exp(d*(Cf2_LCL/1e-12)));
%Evaluation of Inductors ESR
Q=500;                  %Assuming the Quality factor of the air...
     core inducotr
% The relation of ESR and inductance
ESR_L1_LCL=(w0*L1_LCL)./Q;       %For L1 compensation
ESR_L2_LCL=(w0*L2_LCL)./Q;       %For L2 Compensation
ESR_Lf1_LCL=(w0*Lf1_LCL)./Q;     %For Lf1 Compensation
ESR_Lf2_LCL=(w0*Lf2_LCL)./Q;     %For Lf2 Compensation
%% The input Impedence of the circuit is evaluated by series ...
    and parallel
% combinatoins of the impendences of teh circuit elements
%Evaluating the Input Impedence
stage8=rl+1j*w0*Lf2_LCL+ESR_Lf2_LCL;        %Series combination...
     of load resistance and Lf2 compensation along with its ESR
stage7=1./((1./((1./(1j*w0*Cf2_LCL))...     %The parallel ...
    combination of teh stage 8 impendence along with the Cf2 ...
    compensation and its ESR
    +(ESR_Cf2_LCL)))+(1./(stage8)));
stage6=stage7+1j*w0*L2_LCL+ESR_L2_LCL;      %The series ...
    combination of the stage 7 impendence along with the L2 ...
    compensation and its ESR
stage5=1./((1./stage6)...                   %The parallel ...
    combination of the stage 5 imoedence along with the c2eq_pi ...
    equivalent capacitance model
```

```
194      +(1./(1./(1j*w0*c2eq_pi))));
195 stage4=stage5+(1./(1j*w0*cmeq));              %The series ...
      combination of stage 5 impedence along with the cmeq ...
      equivalent  capacitance model
196 stage3=1./((1./stage4)...                     %The parallel ...
      combination of stage 4 along with the c1eq
197      +(1./(1./(1j*w0*c1eq_pi))));
198 stage2=stage3+1j*w0*L1_LCL+ESR_L1_LCL;        %The series ...
      combination of stage 3 impedence along with teh L1 ...
      compensation and its ESR
199 stage1=1./((1./stage2)+...                     %The parallel ...
      combination of stage 2 along with the Cf1 compensation and ...
      its ESR
200      (1./((1./(1j*w0*Cf1_LCL))+(ESR_Cf1_LCL))));
201 %this will be the input impedence for the source voltage
202 stage0=stage1+(1j*w0*Lf1_LCL)...              %The series ...
      combination of stage 1 along with the Lf1 and its ESR
203      +ESR_Lf1_LCL;
204 % %AC side Input Impedence of the System
205 % mag_z=abs(stage0);
206 % ang_z=angle(stage0);
207 %Evaluation of the Source Current
208 is=vs_rms./stage0;           %voltage divided by the input ...
      impedence
209 % is_rms_abs=abs(is);
210 % is_rms_ang=angle(is);
211 %Evaluation of necessary voltage and current across the stages ...
      impedences
212 %Stage 1 Impedence is in series with the stage 0 impedence ...
      hence current
213 %will remain the constant and hence voltage will be evaluated
214 v_stage1=is.*stage1;
215 %The stage 2 voltage will have the same voltage as stage 1 ...
      because both
216 %are in parallel
217 v_stage2=v_stage1;
218 %The current in stage 2 is according to ohms law
219 i_stage2=v_stage2./stage2;
220 %The voltage across stage 3 is the current in stage 2(same for ...
      stage 3) and stage 3 impedence
221 v_stage3=i_stage2.*stage3;
222 %The voltage across stage 4 and stage 3 is same because they ...
      are in
223 %parallel
224 v_stage4=v_stage3;
```

```
%The current through stage 4 impedence
i_stage4=v_stage4./stage4;
%The voltage across stage 5 impedence
v_stage5=i_stage4.*stage5;
%The voltage across stage 6 is same as stage 5 because it is ...
    constant
v_stage6=v_stage5;
%The current through the stage 6 impedence
i_stage6=v_stage6./stage6;
%The voltage across the stage 7 impedence
v_stage7=i_stage6.*stage7;
%The voltage across the stage 8 impedence
v_stage8=v_stage7;
%The current through stage 8 current
i_stage8=v_stage8./stage8;
%The voltage across load resistance
v_rl=i_stage8*rl;
%The current through the load resistance which is same as of ...
    stage 8
i_rl=i_stage8;
%% Evaluation of Voltage and Current of the Compensation ...
    Elements
v_lf1=is.*((1j*w0*Lf1_LCL)+ESR_Lf1_LCL);                    %...
    Voltage across the Lf1 Inductor along with the ESR
i_branch_ESRLf1=is;                                         %...
    Current through Lf1
v_ESR_Lf1_LCL=i_branch_ESRLf1.*ESR_Lf1_LCL;                 %...
    Voltage Across  the ESR of Lf1
i_ESR_Lf1=is;
i_lf1_rms=abs(i_branch_ESRLf1);                             %RMS ...
    Current Lf1
v_lf1_rms=abs(v_lf1);                                       %RMS ...
    voltage across the Lf1 inductor
i_branch_Cf1_ESRCf1=v_stage1./(((1./(1j*w0*Cf1_LCL))...     %...
    Current through the Cf1 and ESR of Cf1
     +(ESR_Cf1_LCL)));
v_ESR_Cf1_LCL=i_branch_Cf1_ESRCf1.*ESR_Cf1_LCL;             %Cf1 ...
    ESR Voltage
% v_ESR_Cf1_LCL_rms=abs(v_ESR_Cf1_LCL);                       %RMS ...
    Cf1 ESR Voltage
v_cf1=v_stage1-v_ESR_Cf1_LCL;                               %Cf1 ...
    Cap Voltage
v_cf1_rms=abs(v_cf1);                                       % RMS ...
    Cf1 Cap Voltage
```

```
256 i_cf1=i_branch_Cf1_ESRCf1;                                  % Cf1 ...
      Cap current
257 i_ESR_Cf1=i_cf1;                                            % Cf1 ...
      ESR Current
258 % i_ESR_Cf1_rms=abs(i_ESR_Cf1);                              % RMS...
       Cf1 ESR current
259 ic_cf1_rms=abs(i_cf1);                                      %RMS ...
      Cf1 Current
260 i_l1=i_stage2;                                              %L1 ...
      Inductor Current
261 i_ESR_L1=i_l1;
262 v_ESR_L1_LCL=i_ESR_L1.*ESR_L1_LCL;
263 i_l1_rms=abs(i_l1);                                         % RMS ...
      L1 Inductor Current
264 v_l1=i_l1.*((1j*w0*L1_LCL)+ESR_L1_LCL);                    % ...
      Voltage across the L1 inductor and ESR of L1
265 v_l1_rms=abs(v_l1);                                        % RMS ...
      value of the Voltage across L1 and ESR of L1
266 i_lf2=i_rl;                                                % Value...
       of the Lf2 current
267 i_ESR_Lf2=i_lf2;
268 v_ESR_Lf2_LCL=i_ESR_Lf2.*ESR_Lf2_LCL;                      %...
      Voltage across the Lf2 inductor and ESR of Lf2
269 i_lf2_rms=abs(i_lf2);                                      % RMS ...
      value of the Lf2 current
270 v_lf2=i_lf2.*((1j*w0*Lf2_LCL)+ESR_Lf2_LCL);                %...
      Voltage across the Lf2 Inductor and ESR of Lf2
271 v_lf2_rms=abs(v_lf2);                                      %RMS ...
      voltage across the Lf2 Inductor and ESR of Lf2
272 i_branch_Cf2_ESRCf2=v_stage7./...
273      (((1./(1j*w0*Cf2_LCL))+(ESR_Cf2_LCL)));               %%...
      Current through the Cf2 and ESR of Cf2
274 v_ESR_Cf2_LCL=i_branch_Cf2_ESRCf2.*ESR_Cf2_LCL;            %%...
      Voltage across the Cf2 inductor and ESR of Cf2
275 % v_ESR_Cf2_LCL_rms=abs(v_ESR_Cf2_LCL);
276 v_cf2=v_stage7-v_ESR_Cf2_LCL;                               %...
      Voltage across Cf2 only
277 v_cf2_rms=abs(v_cf2);                                       %rms ...
      value of the Cf2 voltage
278 i_cf2=v_cf2./(1./(1j*w0*Cf2_LCL));                         %...
      Current through Cf2
279 ic_cf2_rms=abs(i_cf2);                                     %rms ...
      value of Cf2 current
280 i_l2=i_stage6;                                             %...
      Current through the L2 compensation inductor
```

```
281 i_ESR_L2=i_l2;                                          %...
      Current through L2 ESR
282 i_l2_rms=abs(i_l2);                                     %rms ...
      value of L2 current
283 v_l2=i_l2.*(1j*w0*L2_LCL);                              %...
      Voltage across L2 inductor
284 v_ESR_L2_LCL=i_l2.*ESR_L2_LCL;                          %...
      Voltage across ESR of L2
285 v_l2_rms=abs(v_l2);                                     %RMS ...
      voltage across the L2 inductor
286 i_ESR_Cf2=i_cf1;                                        %...
      Current through ESR of Cf2
287
288 % i_ESR_Cf2_rms=abs(i_ESR_Cf2);                         %RMS ...
      current through the Cf2 ESR
289 v_c1eq_pi=v_cf1-v_l1;                                  %...
      Voltage across the c1eq_pi capacitance model
290 v_c1eq_pi_rms=abs(v_c1eq_pi);                          %RMS ...
      Voltage across the c1eq_pi capacitance model
291 v_p12=v_c1eq_pi;                                       %...
      Voltage across Plate 1 and 2
292 v_p12_rms=v_c1eq_pi_rms;                              %RMS ...
      Voltage across Plate 1 and 2
293 i_cmeq=i_stage4;                                       %...
      Current through the cmeq capacitance
294 i_cmeq1=i_cmeq;                                        %Same ...
      as above
295 v_cmeq1=i_cmeq1.*(1./(1j*w0*2*cmeq));                  %...
      Voltage across the cmeq capacitance
296 v_cmeq1_rms=abs(v_cmeq1);                              %RMS ...
      voltage across cmeq capacitance
297 v_cmeq=v_cmeq1;                                        %Same ...
      as above
298 v_cmeq_rms=v_cmeq1_rms;                                %RMS ...
      voltage across the cmeq equivalent capacitance model
299 %voltages across plates
300 v_p42_rms=v_cmeq1_rms;                                 %RMS ...
      voltage across plate 4 and 2
301 v_p32=v_c1eq_pi-v_cmeq;                                % ...
      voltage across plate 3 and 2
302 v_p32_rms=abs(v_p32);                                  %RMS ...
      voltage across plate 3 and 2
303
304 %% Power in various elements and output and input
```

```
%To analytically evaluate the power at the source side and load...
    side
Pout=abs(v_rl).*abs(i_rl)...                                %Active...
    Power ant the Output side
    .*cos(angle(v_rl)-angle(i_rl));
Pin=abs(vs_rms).*abs(is)...                                 %Active...
    Power at the input side
    .*cos(angle(vs_rms)-angle(is));
%Power loss in various compensation ESR
Ploss_ESR_Cf1=abs(v_ESR_Cf1_LCL).*abs(i_ESR_Cf1).*...       %Cf1 ...
    Ploss
    abs(cos(angle(v_ESR_Cf1_LCL)-angle(i_ESR_Cf1)));
Ploss_ESR_Cf2=abs(v_ESR_Cf2_LCL).*abs(i_ESR_Cf2).*...       %Cf2 ...
    Ploss
    abs(cos(angle(v_ESR_Cf2_LCL)-angle(i_ESR_Cf2)));
Ploss_ESR_Lf1=abs(v_ESR_Lf1_LCL).*abs(i_ESR_Lf1).*...       %Lf1 ...
    Ploss
    abs(cos(angle(v_ESR_Lf1_LCL)-angle(i_ESR_Lf1)));
Ploss_ESR_Lf2=abs(v_ESR_Lf2_LCL).*abs(i_ESR_Lf2).*...       %Lf2 ...
    Ploss
    abs(cos(angle(v_ESR_Lf2_LCL)-angle(i_ESR_Lf2)));
Ploss_ESR_L1=abs(v_ESR_L1_LCL).*abs(i_ESR_L1).*...          %L1 ...
    Ploss
    abs(cos(angle(v_ESR_L1_LCL)-angle(i_ESR_L1)));
Ploss_ESR_L2=abs(v_ESR_L2_LCL).*abs(i_ESR_L2).*...          %L2 ...
    Ploss
    abs(cos(angle(v_ESR_L2_LCL)-angle(i_ESR_L2)));
%Getting the Total Power losses
P_loss_total=Ploss_ESR_Cf1+Ploss_ESR_Lf2+Ploss_ESR_L1+...
    Ploss_ESR_L2+...
    Ploss_ESR_Cf2+Ploss_ESR_Lf1;
%Evaluating the Efficiency of the Systems with varying ...
    compensation values
Efficiency=pout./(pout+P_loss_total);
%% Evaluating the Reactive Power of the compensation elements ...
    along
% with the total reactive power
%Evaluating The Reactive Power within the compensation ...
    components
Q_Lf1=i_branch_ESRLf1.*v_lf1;
Q_Lf1_rms=abs(Q_Lf1);                                       %...
    Reactive Power of Lf1
Q_Cf1=i_cf1.*v_cf1;                                         %...
    Reactive Power of Cf1
```

```
334 Q_Cf1_rms=abs(Q_Cf1);                                    %%...
      Reactive Power of Cf1
335 Q_L1=i_l1.*v_l1;                                         %%...
      Reactive Power of L1
336 Q_L1_rms=abs(Q_L1);                                      %%...
      Reactive Power of L1
337 Q_Lf2=i_lf2.*v_lf2;                                     %%...
      Reactive Power of Lf2
338 Q_Lf2_rms=abs(Q_Lf2);                                    %...
      Reactive Power of Lf2
339 Q_Cf2=i_cf2.*v_cf2;                                     %...
      Reactive Power of Cf2
340 Q_Cf2_rms=abs(Q_Cf2);                                    %%...
      Reactive Power of Cf2
341 Q_L2=i_l2.*v_l2;                                        %...
      Reactive Power of L2
342 Q_L2_rms=abs(Q_L2);                                      %...
      Reactive Power of L2
343 Q_total=Q_Lf1_rms+Q_Cf1_rms+Q_L1_rms...                  %Total ...
      Reactive Power
344     +Q_Lf2_rms+Q_Cf2_rms+Q_L2_rms;
345 %% This section selects the compensation for one unique ...
      equivalent capacitance model which has minimum reactive ...
      power
346 %Total Number of Samples we have
347 Total_index=numel(Q_total);                              %Total ...
      number of elements in arrat of reactive power
348 Pout1=round(Pout,2);                                     %...
      Rounding off the Pout vector
349 index=find(Pout1>=0.98*pout);                           %Making...
       the index vector with a condition of active power at least ...
      98% of the required output power
350 Pout_max=max(Pout1);                                    %...
      Getting the available maximum power output for
351                                                          % ...
      unique capacitance model
352 if Pout_max>=0.98*pout                                  %...
      Setting an if condition under which the maxmimum
353                                                          % ...
      output power available from the sets of
354                                                          % ...
      compensation are satisfying the minimum
355                                                          % ...
      required active power
356 %Number of Samples that are left with output power condition
```

```
357 Remaining_index=Total_index-numel(index);
358 %The range of the reactive power that satisfies the output ...
      power condition
359 Q_Low_Range=Q_total(index(1):index(end));
360 % Extracting Minimum Value of Q_total and corresponding index ...
      within the
361 %power condition
362 % Q_lowest=Q_total(index(1));
363 [Q_min(1,1),Q_min_Index(1,1)]=min(Q_Low_Range);
364 %Evaluating the minimum index of the Q_minimum wrt the total ...
      index length
365 Q_min_total_index=Q_min_Index(1,1)+Remaining_index;
366 %veryfying that both minimum q with different index number have...
       same Q_min
367 %value
368 Q_total_min(1,1)=Q_total(Q_min_total_index);
369 %Getting the values of the compensation and plate voltages and ...
      equivalent
370 %capacitance with respect to the minimum index total value
371 Cf1_LCL_minimium_Q(1,1)=Cf1_LCL(Q_min_total_index);
372 Cf2_LCL_minimium_Q(1,1)=Cf2_LCL(Q_min_total_index);
373 Lf1_LCL_minimium_Q(1,1)=Lf1_LCL(Q_min_total_index);
374 Lf2_LCL_minimium_Q(1,1)=Lf2_LCL(Q_min_total_index);
375 L1_LCL_minimium_Q(1,1)=L1_LCL(Q_min_total_index);
376 L2_LCL_minimium_Q(1,1)=L2_LCL(Q_min_total_index);
377 v_p12_rms_minimum_Q(1,1)=v_p12_rms(Q_min_total_index);
378 v_p32_rms_minimum_Q(1,1)=v_p32_rms(Q_min_total_index);
379 v_p42_rms_minimum_Q(1,1)=v_p42_rms(Q_min_total_index);
380
381 %Selecting the ESR of the compensation based on the minimum ...
      reactive power
382 ESR_Cf1_LCL_minimum_Q(1,1)=ESR_Cf1_LCL(Q_min_total_index);
383 ESR_Cf2_LCL_minimum_Q(1,1)=ESR_Cf2_LCL(Q_min_total_index);
384 ESR_Lf1_LCL_minimum_Q(1,1)=ESR_Lf1_LCL(Q_min_total_index);
385 ESR_Lf2_LCL_minimum_Q(1,1)=ESR_Lf2_LCL(Q_min_total_index);
386 ESR_L1_LCL_minimum_Q(1,1)=ESR_L1_LCL(Q_min_total_index);
387 ESR_L2_LCL_minimum_Q(1,1)=ESR_L2_LCL(Q_min_total_index);
388
389 i_Cf1_LCL_minimum_Q(1,1)=ic_cf1_rms(Q_min_total_index);
390 i_Cf2_LCL_minimum_Q(1,1)=ic_cf2_rms(Q_min_total_index);
391 i_lf1_LCL_minimum_Q(1,1)=i_lf1_rms(Q_min_total_index);
392 i_lf2_LCL_minimum_Q(1,1)=i_lf2_rms(Q_min_total_index);
393 i_l1_LCL_minimum_Q(1,1)=i_l1_rms(Q_min_total_index);
394 i_l2_LCL_minimum_Q(1,1)=i_l2_rms(Q_min_total_index);
395
```

```
396 v_Cf1_LCL_minimum_Q(1,1)=v_cf1_rms(Q_min_total_index);
397 v_Cf2_LCL_minimum_Q(1,1)=v_cf2_rms(Q_min_total_index);
398 v_lf1_LCL_minimum_Q(1,1)=v_lf1_rms(Q_min_total_index);
399 v_lf2_LCL_minimum_Q(1,1)=v_lf2_rms(Q_min_total_index);
400 v_l1_LCL_minimum_Q(1,1)=v_l1_rms(Q_min_total_index);
401 v_l2_LCL_minimum_Q(1,1)=v_l2_rms(Q_min_total_index);
402
403 Pout_LCL_minimum_Q(1,1)=Pout(Q_min_total_index);
404 Pin_LCL_minimum_Q(1,1)=Pin(Q_min_total_index);
405 Ploss_total_minimum_Q(1,1)=P_loss_total(Q_min_total_index);
406
407 % Rectifier Losses evaluated from the equations are
408 Losses_rectifier_output=Losses_rectifier;
409 Efficiency_minimum_Q(1,1)=Efficiency(Q_min_total_index);
410 % v_Lf1_LCL_rms_minimum_Q(1,1);
411 c1eq_pi_sets(1,1)=c1eq_pi;
412 c2eq_pi_sets(1,1)=c2eq_pi;
413
414 % Extracting the Optimized Compensation Capacitance Based on ...
      theminimum reactive Power.
415 Cf1_LCL=Cf1_LCL(index(1));
416 Cf2_LCL=Cf2_LCL(index(1));
417 Lf1_LCL=Lf1_LCL(index(1));
418 Lf2_LCL=(Lf2_LCL(index(1)));
419 L1_LCL=L1_LCL(index(1));
420 L2_LCL=L2_LCL(index(1));
421
422 %Verifying the values of compensation with the resonance ...
      condition
423 % w1=1/(2*3.14*sqrt(Cf1_LCL*Lf1_LCL));
424 sp_q=1;
425 tp_g=1;
426
427 % For LCL Simulation in Simulink Model
428 %This is not required but just saved whenever we requires these...
      as outputs
429 %for simulink simulation
430 Cf1_LCL_1_1=Cf1_LCL_minimium_Q(tp_g,sp_q);
431 Cf2_LCL_1_1=Cf2_LCL_minimium_Q(tp_g,sp_q);
432 L1_LCL_1_1=L1_LCL_minimium_Q(tp_g,sp_q);
433 L2_LCL_1_1=L2_LCL_minimium_Q(tp_g,sp_q);
434 Lf2_LCL_1_1=Lf2_LCL_minimium_Q(tp_g,sp_q);
435 Lf1_LCL_1_1=Lf1_LCL_minimium_Q(tp_g,sp_q);
436 ESR_Cf1_1_1=ESR_Cf1_LCL_minimum_Q(tp_g,sp_q);
437 ESR_Cf2_1_1=ESR_Cf2_LCL_minimum_Q(tp_g,sp_q);
```

```
438 ESR_Lf1_1_1=ESR_Lf1_LCL_minimum_Q(tp_g,sp_q);
439 ESR_Lf2_1_1=ESR_Lf2_LCL_minimum_Q(tp_g,sp_q);
440 ESR_L1_1_1=ESR_L1_LCL_minimum_Q(tp_g,sp_q);
441 ESR_L2_1_1=ESR_L2_LCL_minimum_Q(tp_g,sp_q);
442 c1eq_pi_1_1=c1eq_pi_sets(tp_g,sp_q);
443 c2eq_pi_1_1=c2eq_pi_sets(tp_g,sp_q);
444 % cmeq_1_1=cmeq_sets(tp_g,sp_q);
445 %The required output for the function
446 P_losses=Ploss_total_minimum_Q(1,1);                    %Total ...
      ESR losses under the condition of minimu reactive power
447 Plate_current=sqrt(2)*i_l1_LCL_minimum_Q(1,1);          %The ...
      peak current in the L1 Inductor of compensation
448 Efficiency_system=Efficiency_minimum_Q;                 %...
      Efficiency of the System with the
449                                                         % which...
       actually is the plate current
450 Cf1=Cf1_LCL;
451 Cf2=Cf2_LCL;
452 Lf1=Lf1_LCL;
453 Lf2=Lf2_LCL;
454 L1=L1_LCL;
455 L2=L2_LCL;
456 Q_var=Q_total_min;
457 esrL1=ESR_L1_1_1;
458 esrL2=ESR_L2_1_1;
459 esrLf1=ESR_Lf1_1_1;
460 esrLf2=ESR_Lf2_1_1;
461 esrCf1=ESR_Cf1_1_1;
462 esrCf2=ESR_Cf2_1_1;
463 c1_eqpi=c1eq_pi;
464 c2_eqpi=c2eq_pi;
465 cm_eq=cmeq;
466 Source_v=vs_rms;
467 Load_r=rl;
468 %If the maximum power available by the sets of compensation for...
       a unique
469 %capacitance model is less than the 98% of the required output ...
      power make the following as an output
470 else
471    iteration_number=j;
472     X=['The compensation design of the given system is not ...
      possible' ...
473         ' as the system is capable of delivering maximum power ...
      of',...
```

```
474             num2str(Pout_max),'.The capacitance matrix number is',...
        num2str(iteration_number),'.'];
475         disp(X)
476         % Making the plate current and losses in the compensation ...
        equal to zero
477         % for that specific iteration
478         Plate_current=0;
479         P_losses=0;
480         v_p12_rms_minimum_Q=0;
481         v_p32_rms_minimum_Q=0;
482         v_p42_rms_minimum_Q=0;
483         Efficiency_system=0;
484         Cf1=0;
485         Cf2=0;
486         Lf1=0;
487         Lf2=0;
488         L1=0;
489         L2=0;
490         Q_var=0;
491         esrL1=0;
492         esrL2=0;
493         esrLf1=0;
494         esrLf2=0;
495         esrCf1=0;
496         esrCf2=0;
497         c1_eqpi=0;
498         c2_eqpi=0;
499         cm_eq=0;
500         Source_v=0;
501         Load_r=0;
502         Losses_rectifier=0;
503 end
504 end
```

Bibliography

[1] «Excitation System Technologies for Wound-Field Synchronous Machines: Survey of Solutions and Evolving Trends». In: *IEEE access* 7 (2019), pp. 109699–109718. DOI: 10.1109/ACCESS.2019.2933493. URL: https://ieeexplore.ieee.org/document/8789384 (cit. on pp. 1, 4, 6, 7).

[2] Mehmet Zahid Erel, Kamil Cagatay Bayindir, Mehmet Timur Aydemir, Sanjay K. Chaudhary, and Josep M. Guerrero. «A Comprehensive Review on Wireless Capacitive Power Transfer Technology: Fundamentals and Applications». In: *IEEE access* 10 (2022), pp. 3116–3143. DOI: 10.1109/ACCESS.2021.3139761. URL: https://ieeexplore.ieee.org/document/9666847 (cit. on p. 1).

[3] Skyler Hagen, Marisa Tisler, Jiejian Dai, Ian P. Brown, and Daniel C. Ludois. «Use of the Rotating Rectifier Board as a Capacitive Power Coupler for Brushless Wound Field Synchronous Machines». In: *IEEE journal of emerging and selected topics in power electronics* 10.1 (Feb. 2022), pp. 170–183. DOI: 10.1109/JESTPE.2020.3039497. URL: https://ieeexplore.ieee.org/document/9265209 (cit. on p. 1).

[4] Wikipedia. *Slip ring*. 2011. URL: https://en.wikipedia.org/wiki/Slip_ring (cit. on p. 5).

[5] «Rotary Transformer Design». In: 4th Edition. Transformer and Inductor Design Handbook. Taylor amp; Francis, 2011, pp. 1–3. URL: https://app.knovel.com/hotlink/pdf/rcid:kpTIDHE002/id:kt00CAZJ31/transformer-inductor/rotary-transformer-design?kpromoter=Summon (cit. on p. 7).

[6] Emanuel E. Landsman. «Rotary transformer design». In: 1970 (cit. on p. 8).

[7] Emanuel E Landsman. «Rotary transformer design». In: *1970 IEEE Power Electronics Specialists Conference*. IEEE. 1970, pp. 139–152 (cit. on p. 8).

[8] N. Tesla. *Experiments with Alternate Currents of High Potential and High Frequency*. Nineteenth Century Collections Online (NCCO): Science, Technology, and Medicine: 1780-1925. W.J.Johnston Company, Limited, 1892. URL: https://books.google.it/books?id=kNhCQPbYIsgC (cit. on pp. 10, 11).

[9] JT Boys and AW Green. «Intelligent road-studs-lighting the paths of the future». In: *Transactions of the Institution of Professional Engineers New Zealand: General Section* 24.1 (1997), pp. 33–40 (cit. on p. 10).

[10] Grant A Covic and John T Boys. «Inductive power transfer». In: *Proceedings of the IEEE* 101.6 (2013), pp. 1276–1289 (cit. on p. 10).

[11] Jiejian Dai and Daniel C. Ludois. «A Survey of Wireless Power Transfer and a Critical Comparison of Inductive and Capacitive Coupling for Small Gap Applications». In: *IEEE Transactions on Power Electronics* 30.11 (2015), pp. 6017–6029. DOI: 10.1109/TPEL.2015.2415253 (cit. on p. 10).

[12] Lixiang Jackie Zou, Aiguo Patrick Hu, and Yu-gang Su. «A single-wire capacitive power transfer system with large coupling alignment tolerance». In: IEEE, 2017, pp. 93–98. DOI: 10.1109/WoW.2017.7959372. URL: https://ieeexplore.ieee.org/document/7959372 (cit. on p. 12).

[13] Hua Zhang, Fei Lu, Heath Hofmann, Weiguo Liu, and Chris Mi. «A 4-Plate Compact Capacitive Coupler Design and LCL-Compensated Topology for Capacitive Power Transfer in Electric Vehicle Charging Applications». In: *IEEE transactions on power electronics* 31.12 (2016), p. 1. DOI: 10.1109/TPEL.2016.2520963 (cit. on pp. 13, 39).

[14] Hua Zhang, Fei Lu, Heath Hofmann, Weiguo Liu, and Chunting Chris Mi. «Six-Plate Capacitive Coupler to Reduce Electric Field Emission in Large Air-Gap Capacitive Power Transfer». In: *IEEE Transactions on Power Electronics* 33.1 (Jan. 2018), pp. 665–675. DOI: 10.1109/tpel.2017.2662583. URL: https://doi.org/10.1109%2Ftpel.2017.2662583 (cit. on pp. 13, 37).

[15] Khurram Afridi. *Fundamentals of Capacitive WPT*. Youtube. 2021. URL: https://www.youtube.com/watch?v=sXvcFGzJr6Y (cit. on pp. 15, 17, 43).

[16] Chao Liu, A. P. Hu, G. A. Covic, and N-K C. Nair. «Comparative Study of CCPT Systems With Two Different Inductor Tuning Positions». In: *IEEE transactions on power electronics* 27.1 (Jan. 2012), pp. 294–306. DOI: 10.1109/TPEL.2011.2158322. URL: https://ieeexplore.ieee.org/document/5783347 (cit. on p. 16).

[17] «A Double-Sided LCLC-Compensated Capacitive Power Transfer System for Electric Vehicle Charging». In: *IEEE transactions on power electronics* 30.11 (Nov. 2015), pp. 6011–6014. DOI: 10.1109/TPEL.2015.2446891. URL: https://ieeexplore.ieee.org/document/7127049 (cit. on pp. 17, 43).

[18] Sijie Ning, Jian Yang, Qi Zhu, Mei Su, Ruya Tan, and Yonglu Liu. «Comparative Analysis of LCL, LCLC, CLLC Compensation Networks for Capacitive Power Transfer». In: *2018 IEEE 4th Southern Power Electronics Conference (SPEC)*. 2018, pp. 1–6. DOI: 10.1109/SPEC.2018.8635862 (cit. on p. 18).

[19] Ashish Kumar, Saad Pervaiz, Chieh-Kai Chang, Sean Korhummel, Zoya Popovic, and Khurram K. Afridi. «Investigation of power transfer density enhancement in large air-gap capacitive wireless power transfer systems». In: IEEE, 2015, pp. 1–4. DOI: 10.1109/WPT.2015.7140182. URL: https://ieeexplore.ieee.org/document/7140182 (cit. on p. 19).

[20] Chao Liu, Aiguo Patrick Hu, and Nirmal-Kumar C. Nair. «Coupling study of a rotary Capacitive Power Transfer system». In: *2009 IEEE International Conference on Industrial Technology*. 2009, pp. 1–6. DOI: 10.1109/ICIT.2009.4939623 (cit. on p. 22).

[21] Inc ANSYS. *Maxwell Help*. English. 2021. 3200 pp. (cit. on pp. 25, 30).

[22] Wenping Chai, Thomas A. Lipo, and Byung-il Kwon. «Design and Optimization of a Novel Wound Field Synchronous Machine for Torque Performance Enhancement». In: *Energies* 11.8 (2018). DOI: 10.3390/en11082111. URL: https://www.mdpi.com/1996-1073/11/8/2111 (cit. on p. 27).

[23] Tausif Husain, Wasi Uddin, and Yilmaz Sozer. «Performance Comparison of Short-Pitched and Fully Pitched Switched Reluctance Machines Over Wide Speed Operations». In: *IEEE Transactions on Industry Applications* 54.5 (2018), pp. 4278–4287. DOI: 10.1109/TIA.2018.2839627 (cit. on p. 28).

[24] Daniela Rodriguez-Sotelo, Martin A. Rodriguez-Licea, Ismael Araujo-Vargas, Juan Prado-Olivarez, Alejandro-Israel Barranco-Gutiérrez, and Francisco J. Perez-Pinal. «Power Losses Models for Magnetic Cores: A Review». In: *Micromachines (Basel)* 13.3 (Mar. 2022), p. 418. DOI: 10.3390/mi13030418. URL: https://www.ncbi.nlm.nih.gov/pubmed/35334709 (cit. on pp. 29, 30).

[25] Olga V Tikhonova, Igor' Malygin, R. K. Beraya, N. V. Sokolov, and Anatoliy Plastun. «Loss calculation of induction motor with ring windings by "ANSYS Maxwell"». In: 2017 (cit. on p. 30).

[26] D.G. Fink and D. Christiansen. *Electronics Engineers' Handbook*. ELECTRONICS ENGINEERS' HANDBOOK. McGraw-Hill, 1989. ISBN: 9780070209824. URL: https://books.google.it/books?id=6w5TAAAAMAAJ (cit. on p. 33).

[27] Mersen company. «Mersen Carbon brushes for motors and generators». In: (2010). URL: https://www.mersen.com/sites/default/files/publications-media/2-ptt-carbon-brush-technical-guide-mersen.pdf (cit. on p. 45).

[28] «IEEE Standard for Safety Levels with Respect to Human Exposure to Electric, Magnetic, and Electromagnetic Fields, 0 Hz to 300 GHz». In: *IEEE Std C95.1-2019 (Revision of IEEE Std C95.1-2005/ Incorporates IEEE Std C95.1-2019/Cor 1-2019)* (2019), pp. 1–312. DOI: 10.1109/IEEESTD.2019.8859679 (cit. on p. 71).

[29] Grayson Zulauf and Juan M. Rivas-Davila. «Single-Turn Air-Core Coils for High-Frequency Inductive Wireless Power Transfer». In: *IEEE Transactions on Power Electronics* 35.3 (2020), pp. 2917–2932. DOI: 10.1109/TPEL.2019.2932178 (cit. on p. 72).

[30] Martin Pelikan. «Bayesian Optimization Algorithm». In: *Hierarchical Bayesian Optimization Algorithm: Toward a new Generation of Evolutionary Algorithms*. Berlin, Heidelberg: Springer Berlin Heidelberg, 2005, pp. 31–48. ISBN: 978-3-540-32373-0. DOI: 10.1007/978-3-540-32373-0_3. URL: https://doi.org/10.1007/978-3-540-32373-0_3 (cit. on p. 76).